MAGYAR ÁLLAMI
EÖTVÖS LORÁND
GEOFIZIKAI INTÉZET

EÖTVÖS LORÁND
GEOPHYSICAL INSTITUTE
OF HUNGARY

GEOFIZIKAI KÖZLEMÉNYEK

GEOPHYSICAL TRANSACTIONS

ВЕНГЕРСКИЙ
ГЕОФИЗИЧЕСКИЙ
ИНСТИТУТ
ИМ Л. ЭТВЕША

ГЕОФИЗИЧЕСКИЙ
БЮЛЛЕТЕНЬ

BUDAPEST

CONTENTS

Characteristics of wave field generated when waves penetrate high-velocity layers near the critical angle	*G. V. Golikova* *M. V. Chizhova* *Yu. A. Surkov*	227
The use of symmetry in *f–k* migration	*E. Maeland*	243
Generalized complex attributes and their use for NMO stretching compensation	*A. Vesnaver* *F. Poletto*	253
Ray-tracing modelling in seismic exploration	*Z. Wéber*	273
Is the magnetotelluric field in the Pannonian basin distorted by Carpathian inhomogeneities?	*A. Ádám* *T. Steiner* *P. Kaikkonen* *M. Menvielle* *P. Tarits*	287
Lithostatistical study of Kharita Formation, Western Desert, Egypt	*A. A. Hassan* *A. A. Saleh*	301

VOL. 35. No. 4. NOV. 1990 (ISSN 0016–7177)

TARTALOMJEGYZÉK

Árnyékoló réteg alatti hullámtér vizsgálata	*G. V. Golikova* *M. V. Csizsova* *Yu. A. Szurkov*	242
Az *f–k* migráció szimmetriájának hasznosítása	*E. Maeland*	252
Általánosított komplex attribútumok és alkalmazásuk a dinamikus korrekció nyújtó hatásának kompenzálására	*A. Vesnaver* *F. Poletto*	271
Sugárkövetéses szeizmikus modellezés	*Z. Wéber*	285
Torzítják-e a magnetotellurikus teret a kárpáti elektromos inhomogenitások a Pannon medencében?	*A. Ádám* *T. Steiner* *P. Kaikkonen* *M. Menvielle* *P. Tarits*	298
A Kharita Formáció (Egyiptom, Ny-i sivatag) kőzetstatisztikai vizsgálata	*A. A. Hassan* *A. A. Saleh*	313

СОДЕРЖАНИЕ

Особенности волнового поля, возникающие при прохождении высокоскоростных слоев в области предельного угла	*Г. В. Голикова* *М. В. Чижова* *Ю. А. Сурков*	242
Утилизация симметрии *f–k* миграции	*Э. Мейланд*	252
Обобщенные комплексные характеристики и их применение в компенсировании эффекта удлинения от динамической поправки	*А. Веснавер* *Ф. Полетто*	272
Сейсмическое моделирование по геометрическому прослеживанию луча	*З. Вебер*	285
Искажают ли Карпатские геоэлектрические неоднородности магнитотеллурическое поле Паннонской впадины?	*А. Адам* *Т. Штейнер* *П. Кайкконен* *М. Менвьель* *П. Таритс*	299
Петростатистическое исследование свиты Харита (Западная пустыня, Египет)	*А. А. Гассан* *А. А. Салех*	313

GEOPHYSICAL TRANSACTIONS 1990
Vol. 35. No. 4. pp. 227–242

CHARACTERISTICS OF WAVE FIELD GENERATED WHEN WAVES PENETRATE HIGH-VELOCITY LAYERS NEAR THE CRITICAL ANGLE

G. V. GOLIKOVA, M. V. CHIZHOVA and Yu. A. SURKOV*

The results obtained from interpreting the wave field of a 1 km offset VSP recorded in a well beneath a high-velocity layer are presented. It was proved that if the angle of incidence of the direct wave was close to the critical angle, the direct wave splits into two components: a ray-type direct wave, which penetrates the layer as a sliding wave, and a screened wave. The screened wave was recorded together with the converted *PSP*-wave at some distance from the first break. In the interpretation, polarization and dynamic features of the waves were used as well as theoretical computations both for the ray-type and the non-ray-type parts of the field.

Keywords: direct wave, converted waves, high-velocity layer, screen, wave field, VSP

1. Introduction

In seismic prospecting practice it was noticed that, when the angle of incidence of the seismic waves arriving to thin, high-velocity layers exceeds the critical angle, seismic energy penetrates the layer whereupon subscreen reflected and refracted waves form in the deeper levels of the stratigraphic sequence contrary to the laws of geometrical optics. GAMBURTSEV [1942] assumed that with increasing offset one meets the phenomenon of screening — which is known in other areas of physics as the 'tunnel effect'. Experimental studies of the screening phenomenon and interpretation of real wave fields in numerous areas of the USSR have resulted in the finding that when high-velocity carbonate rocks are present in the upper levels of the stratigraphic sequence, strong subscreen refracted and reflected waves are detectable. When observing such waves in the immediate neighbourhood of thin layers during vertical seismic profiling one can state that these waves are much more intense than waves which reach the same observation point and propagate in accordance with the laws of geometrical optics.

2. Investigation goals

Experimental vertical seismic profiling was carried out in a borehole — at depths down to 2750 m — with a three-component sonde and a series of shotpoints (SP) of various offsets [GOLIKOVA et al. 1982].

One of the tasks of the investigation consisted in studying the nature of the waves in a wide range of offset (from standard CDP to refraction seismic offsets).

*198904 Leningrad, Petrodvorets, Ulyanovskaya 1 Manuscript received: 16 August, 1989
Nauchno Issledovatelsky Institut Fiziki

Even while the work was carried out it became obvious that the solution is closely connected with the conditions of the penetration of waves through high-velocity layers.

When analysing and interpreting wave fields we noticed that the phenomena of screening and sliding strongly influence the resulting wave field. In the further discussion, screening will be understood as non-ray-type penetration of a wave through a high-velocity layer when the angle of incidence exceeds the critical angle. Sliding takes place if the angle of incidence is somewhat smaller than the critical angle.

It is usually considered that screening appears at large-offset CDP technique when the reflected wave field is registered in a 1.0–2.5 km range. This is, however, not always true. By VSP it was shown that high-velocity layers in upper levels of the stratigraphic sequence already behave as screens when the offset reaches 0.5 km. With increasing offset, layers lying deeper and deeper turn into screens. For example, high-velocity layers at 2–3 km depths start behaving as screens from a 1.5 km offset. Moreover, it was noted that the offset at which sliding and screening appear also depends on structural features of the sequence. Consequently, sliding waves and screened waves in a seismic wave field are to be expected not only at large-offsets but also at small-offset CDP as well as in parameters of the stratigraphic sequence are highly variable.

In our example there are many high-velocity layers *(Fig. 1.)*. The strongest velocity- and density contrasts are observable on the boundaries of a limestone layer between 360 and 460 m and of anhydrite layers from 2420 to 2460 m and from 2525 to 2550 m depths. The first calculations for direct, refleted and refracted waves for this sequence [GOLIKOVA and CHIZHOVA 1981] were those on screened wave fields in the borehole. In addition, the available published works [FAYZULIN 1971, POGONYAILO 1968] provided data on the screening effect both for field experiments and modelling. In spite of this information, for a long time there was no success in realizing and interpreting the characteristics of the wave field which accompanies the penetration of high-velocity layers at angles close to the critical angle. In the present paper it is described what we could reach in establishing the conditions of screening.

3. Characteristics of the wave field. Interpretation

Let us consider the wave fields of 0.2 s duration after the first break from 645 to 1300 m depths obtained with 1 km (SP–1, *Fig. 2*) and 0.1 km offsets (SP–0, *Fig. 3*), respectively. It can be seen that the wave fields were recorded beneath the limestone layer.

From simple geometrical considerations it can be concluded that for waves SP–1 the angle of incidence of the direct wave and its satellites exceeds 20° whereas from SP–0 the layers are penetrated almost vertically.

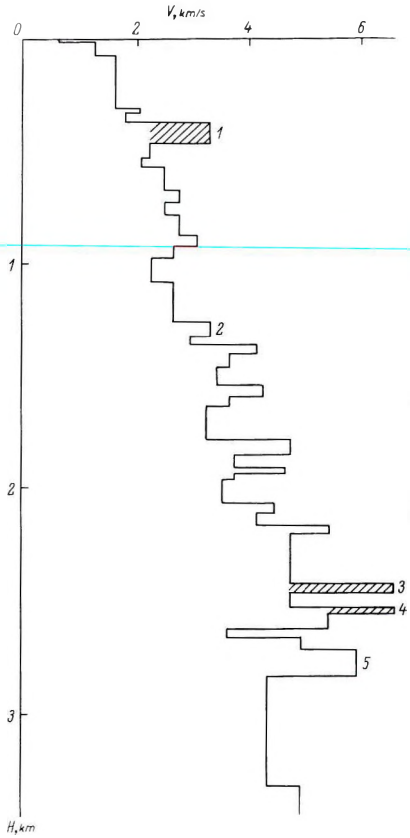

Fig. 1. Velocity sequence. Hatched layers — screens; 1, 2, etc. — serial numbers of high-velocity layers referred to in the paper

1. ábra. Lépcsős sebesség menet. A vonalkázott rétegek az árnyékolók (1, 2 stb. a cikkben használt hivatkozás az egyes árnyékolókra)

Рис. 1. Ступекчатая кривая скоростей. Заштрихованные слои – экраны (1, 2 – ссылки в тексте на номера слоев)

In seismograms from SP–1 (Fig. 2) the direct wave exhibits some peculiarities. In the 645–1000 m depth range it is of lower frequency than it is when deeper. Its amplitude decreases with decreasing depth, i.e. the nearer the observation points are to the screen, which means increasing angle of penetration through the high-velocity layer. At the same time, in the zero-offset seismograms (SP–0, Fig. 3.) the direct wave form is of high stability and decreasing amplitude with increasing depth. Visual study of the seismograms reveals some other differences as well. For example, in the zero-offset records the direct wave sharply attenuates with time, while in the far-offset seismograms after the direct wave arrival a field of nearly the same intensity was recorded. Another peculiarity of the field from (SP–1) is the presence of in-phase axes (hatched peaks) of higher apparent velocities than the direct wave.

In the 1 km offset VSP beneath the high-velocity layer of the above seismograms, in addition to the direct wave and its satellites which originate in the upper levels of the sequence, an intense interference field was recorded consisting of the screened direct wave, E, and converted PSP-waves. This field

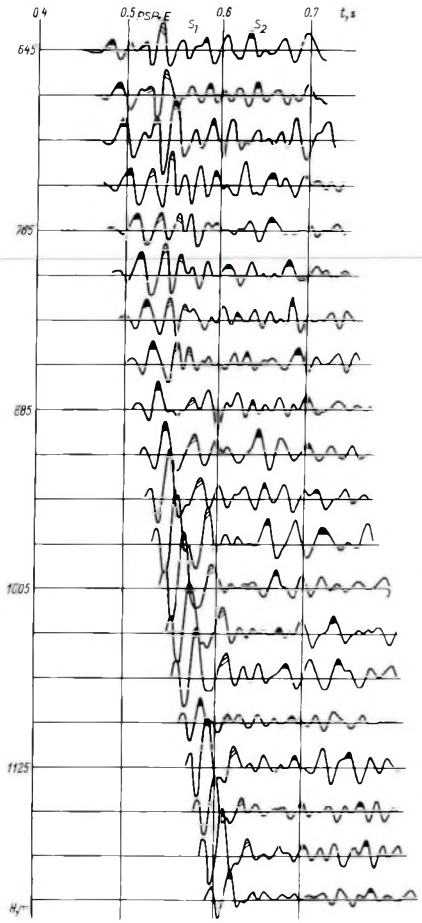

Fig. 2. Records of the *Z*-component of the VSP field from SP–1. Filled peaks — direct waves and their satellites; hatched peaks — converted *PSP*- and screened waves (*E*)

2. ábra. Az SP–1 robbantópontból kapott VSP hullámtér *Z*-komponense. Befeketített maximumok a direkt hullámok és szatellitáik, a vonalkázott maximumok a konvertált *PSP*- és az árnyékolt hullám (*E*)

Рис. 2. Компонента *Z* поля ВСП, полученного из взрывпункта SP–1. Зачерненные экстремумы – падающие волны, заштрихованные экстремумы – волны *PSP* и экранированные (Э).

is observable at depths between 500 and 1300 m. In *Fig. 4* a sketch illustrates the generation of the above-mentioned waves. In order to confirm the above hypothesis experimental and theoretical characteristics of the suggested wave types have been compared. Traveltime curves, amplitude curves of the total displacement vector, and curves of the angle of incidence have been constructed for the phases marked by filled peaks in the seismograms. In general, the quantitative characteristics of the field confirmed its visually detectable features. Let us consider these characteristics in detail.

The direct wave

In *Fig. 5.* amplitude curves for the total displacement vector $A(H)$ are displayed. One of them corresponds to the direct wave in a vertical direction, SP–0 while two others to records of shot points at a distance of 1 km from the

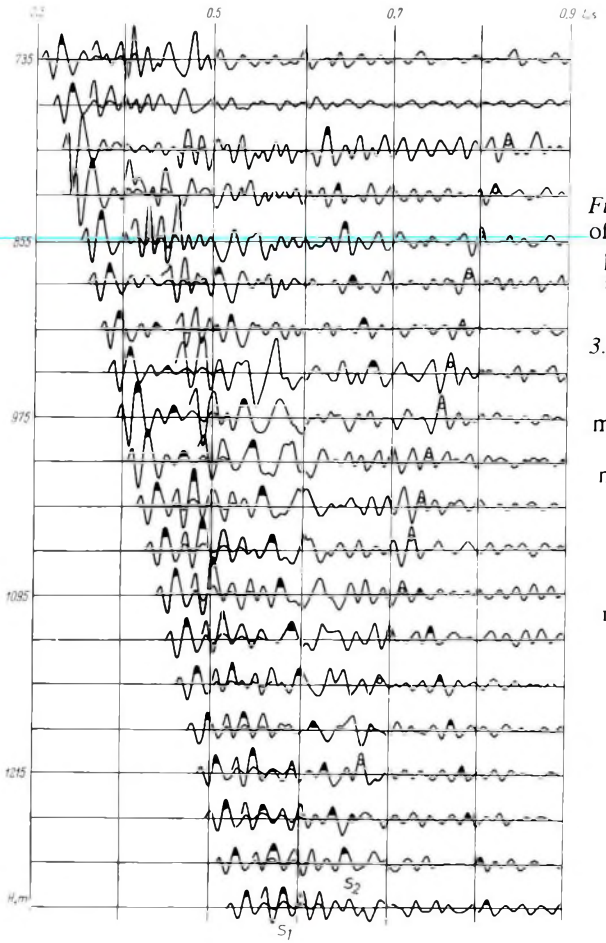

Fig. 3. Record of the *Z*-component of the VSP field from SP–0. Filled peaks — direct waves and their satellites; peaks with circles — reflected waves

3. ábra. Az SP–0 robbantópontból kapott VSP hullámtér *Z*-komponense. Befeketített maximumok a direkt hullámok és szatellitáik, a körökkel jelölt maximumok reflektált hullámok

Рис. 3. Компонента *Z* поля ВСП, полученного из взрывпункта SP–0. Зачененные экстремумы – падающие волны; экстремумы с кружкамы – отраженные волны.

borehole: SP–1 and SP+1. On the first curve a continuous decrease of the direct wave is observable with increasing depth of the observation points. The behaviour of the curves from SP–1 and from SP+1 is completely different. An interval of sharp increase of the amplitudes can be distinguished from the bottom of the high-velocity limestone layer down to 700 m depth which is replaced by an interval of a less sharp increase of the amplitude between 700 and 1000 m. Further, down to 1500 m the direct wave diminishes a little. At the same time the apparent frequency of the arrivals in the 500–1300 m depth range gradually increases from 30 to 45 Hz.

Polarization diagrams, constructed in the incidence plane by use of a three-component record of the direct wave in the study interval of the sequence, are elliptical with excentricity ($K=1-b/a$) of about 0.8–0.9 (a and b are the

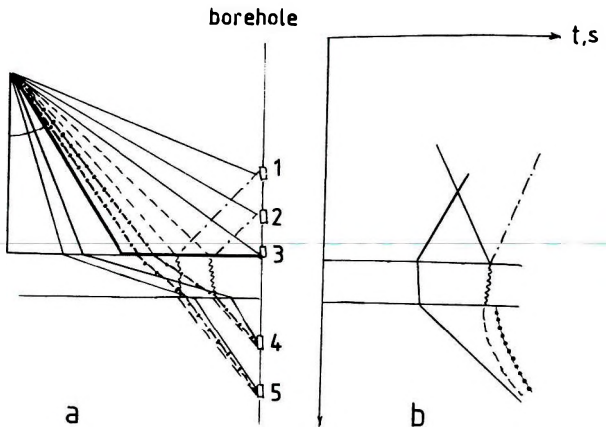

Fig. 4. Sketch of an offset VSP in a model containing a high-velocity layer
a) Sketch of raypaths
b) Traveltime curves
Thin continuous line — direct *P*-wave; dashed line — screened wave; bold dot-dash line — converted *PSP*-wave; bold-face line — head wave; thin dot-dash line — reflected wave; 1, 2 ... — observation points in the borehole

4. ábra. Távoli gerjesztésű VSP vázlata árnyékolót tartalmazó modell esetén
a) Sugárutak
b) Út–idő görbék
folyamatos vonal — direkt hullám; szaggatott vonal — árnyékolt hullám; vastag pont-vonal — konvertált *PSP* hullám; vastag folytonos vonal — refraktált hullám; vékony pont-vonal — reflektált hullám; 1, 2 ... — észlelési pontok a fúrásban

Рис. 4. Схема ВСП с дальним возбуждением для модели с экраном.
а) лучевая схема,
в) годографы.
Сплошные линии – лучи прямой волны; штрихованные линии – лучи экранированной волны; жирные линии с точками – лучи обменной волны *PSP*; жирная линия – путь головной волны;
тонкая штрих-пунктирная линия – лучи отраженной волны;
1, 2... – точки наблюдения в скважине.

lengths of the axes of the ellipse). It should be noted that in the deeper levels of the sequence the excentricity of the first break is as much as 0.95 which means near-linear polarization. In that the polarization is elliptical. It may support either interference of the waves or the existence of a wave field which cannot be described by zero-approximation of the ray-tracing method. For the wave above, the angles and azimuths of incidence to the observation points have also been computed.

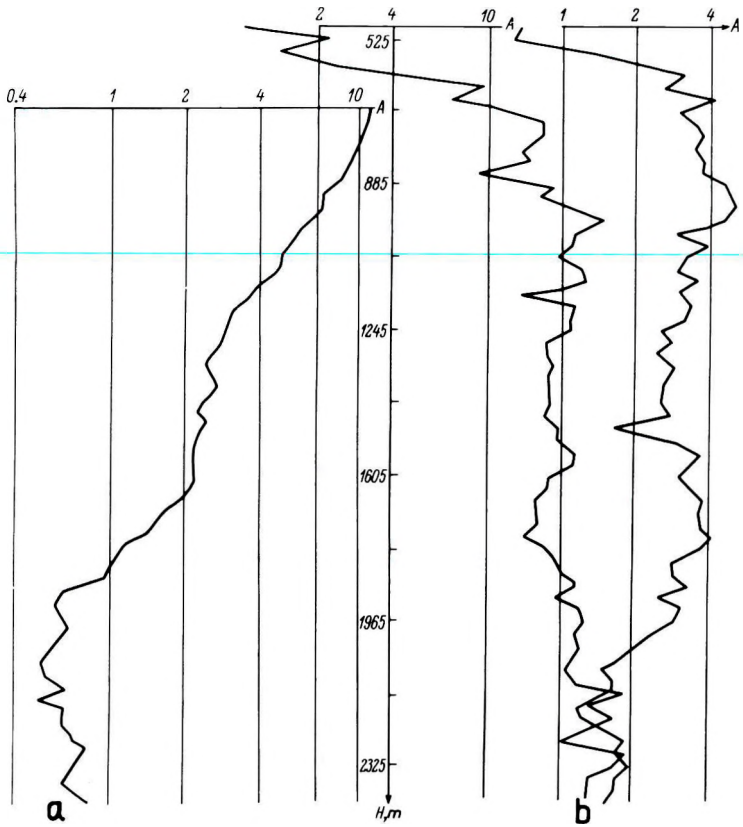

Fig. 5. Amplitude curves of the direct wave

5. ábra. A direkt hullám amplitudó menete

Рис. 5. Амплитудные кривые прямой волны.

Polarization processing of data of three-component VSPs is described by BERDENNIKOVA et al. [1983]. It is known that the parameters of the ray at the observation point can only be determined for the linearly polarized wave from its amplitude. In spite of this, angles of arrival γ for all waves studied have been computed by considering the direction of the large axis of the ellipse as that of the ray. The computed values contain large errors, which exceed 10°. In view of the lack of accuracy in determining the angles of arrival in the interpretation, we have used only a mean value of γ for the whole depth interval under consideration.

Based on computed values of γ we have evaluated the mean angle of arrival of the rays to the upper boundary of the layer. Computations revealed that the angle of incidence of rays of the direct wave is close to the critical angle and that, inside the layer, the wave propagates along sliding trajectories.

It is known that if thin, high-velocity layers are penetrated by sliding waves an interference wave field is generated. Its description is possible by first and higher order approximations of the ray-tracing method. It is suggested that the presence of low frequencies in the record of the direct wave is connected with the mechanism of its penetration through the high-velocity layer and with the existence of displacement components which can be described by the first approximation of wave splitting.

Satellites of the direct wave

In the seismogram of Fig. 3 in the 0.2 s time interval after the first break of the direct wave, a series of in-phase axes of waves parallel to the direct wave is displayed, with an intensity of about 20–30% of that of the direct wave. These waves were generated in the upper levels of the sequence. The relative intensities of the satellites (S_1 and S_2) increase with increasing offset (compare Figs. 2 and 3).

The curves of the angle of incidence versus depth *(Fig. 6)* show a large scatter of local values. The mean values of the angles of incidence lead us to suppose that the satellites, as well as the direct wave, penetrate the high-velocity layer as sliding waves.

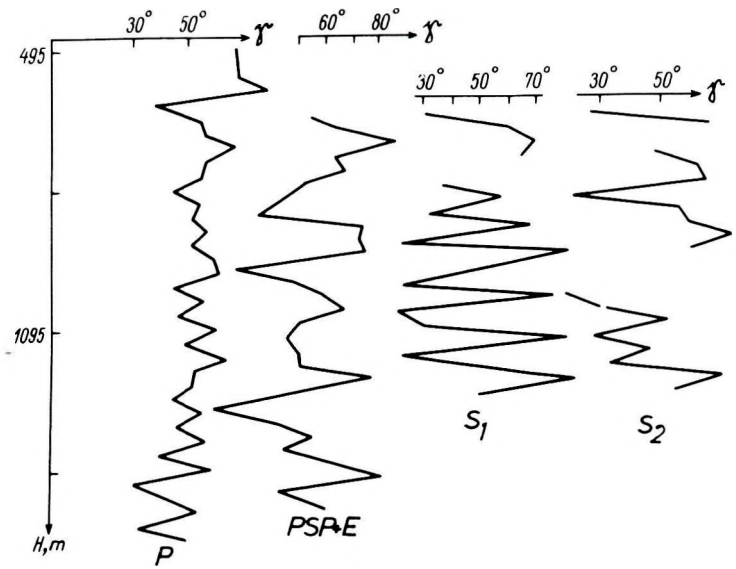

Fig. 6. Angles of arrival versus depth of waves arriving to the observation points from SP–1

6. ábra. A hullámok beérkezési szögei a mélység függvényében (gerjesztés SP–1-ben)

Рис. 6. Углы подхода волн к точкам наблюдения как функция глубины (возбуждение в SP–1.).

At large offsets an interference field of unknown origin was recorded between the direct wave and satellites S_1 and S_2. Calculations for the wave kinematics have shown that within this time interval the waves penetrated the high-velocity layer as *PSP*- and screened direct *S*-waves. The behaviour of the computed traveltime curves is in agreement with recorded kinematic data *(Fig. 7)*. *Figure 8* presents the amplitude versus depth curves of this field down to about 1100 m depth. The field intensity sharply decreases below this depth; this sharp decrease is possibly linked with the disappearance of the screened wave and a decrease in the *PSP*-wave intensity. Mean values of angles of arrival of the same phase are of about 55–60° (Fig. 6) and show that, in the wave field, waves are present which were generated at the incidence of the direct wave to the high-velocity layer at angles larger than the critical angle. When considering kinematic and polarization-dynamic characteristics of the wave field originating from SP–1 and recorded beneath the high-velocity layer, we can draw conclusions as follows:

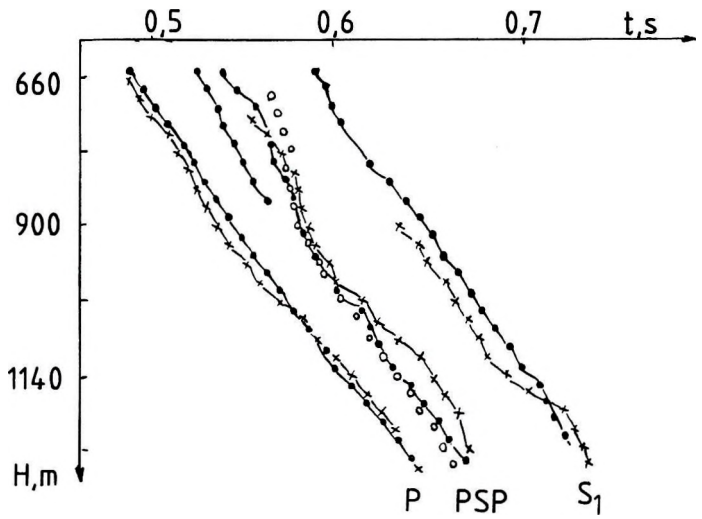

Fig. 7. Traveltime curves of satellite waves of Fig. 2. Lines with dots — recorded peaks; lines with crosses — computed; circles — computed traveltime curve of the screened wave

7. ábra. A 2. ábra hullámainak út–idő görbéi. Pontozott vonal — észlelt maximumok; x-el jelölt vonal — számított görbe; körökkel jelölt vonal — az árnyékolt hullám számított út–idő görbéje

Рис. 7. Годографы волн, регистрируемых вблизи прямой волны рис. 2.
Линии с точками – наблюденные максимумы,
линии с крестиками – расчетные кривые,
кружочки – теоретический годограф экранированной волны.

1) If the angle of incidence of the direct wave arriving to the high-velocity layer is close to the critical angle the wave field splits into two parts. One of them is of ray type and consists of the direct wave proper and its satellites which penetrate the high-velocity layer along sliding rays. The other part propagates through the layer in a non-ray way as a screened wave. Among these waves a converted *PSP*-wave has also been recorded, its role in the wave field increasing if the angle of incidence of the direct wave exceeds the critical.

2) Immediately below the high-velocity layer the whole wave field is of low intensity. With increasing distance from the layer the field intensity sharply increases, with the maximum amplitudes being recorded in the 700–1200 m depth range.

3) Beneath the high-velocity layer the frequency of some waves is decreased.

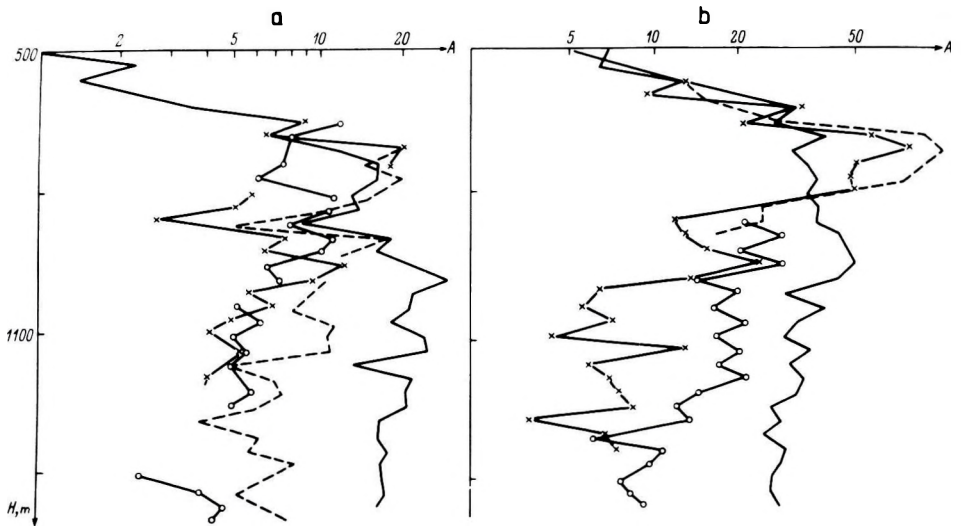

Fig. 8. Experimental amplitude curves for shotpoints SP–1 (a) and SP+1 (b). Continuous line — direct *P*-wave; dashed line — *PSP*- and screened waves; line with crosses — S_1; line with circles — S_2

8. ábra. Az SP–1-hez (a) és az SP+1-hez (b) tartozó kísérleti amplitudó görbék. Folytonos vonal — direkt *P*-hullám; szaggatott vonal — *PSP*- és árnyékolt hullám; x-el jelölt vonal — S_1; körökkel jelzett vonal — S_2

Рис. 8. Экспериментальные амплитудные кривые, относящиеся к SP–1 (а) и SP+1 (b). Сплошная линия – прямая волна *P*; штриховая линия – волные *PSP* и Э; линия с крестиками – S_1, линия с кружками – S_2.

4. Theoretical wave calculations

In order to confirm the interpretation, those results of theoretical calculations were used which are based on formulae of the zero-approximation of the ray-tracing method. In computations of the screened wave it was taken into account [VORONIN 1959] that the wave attenuation is of exponential type with a factor $\mu\kappa$ where μ = frequency of the recorded wave and κ = screening coefficient.

$$\kappa = h/V\sqrt{\sin^2\theta - \sin^2\tilde{\theta}}$$

where h = thickness of screening layer, V = velocity in the layer above the screen, θ = angle of incidence of the ray to the upper boundary of the layer, $\tilde{\theta}$ = angle of total reflection.

In order to compute the wave fields the velocity model of the medium (Fig. 1) was applied. For the main screen, i.e. limestone in the upper level of the sequence, several versions of seismic models were considered. In each model fields of the direct wave, of the screened wave and of the *PSP*-wave were computed and compared.

Theoretical calculations revealed the high-degree of sensitivity of the screened wave intensity to variations in the screen thickness and to the contrast in *P*-wave velocity on its boundaries. For instance, in screen models which consist of a 100 m thick layer the screened wave had insignificant intensity compared with other waves. The best correspondence of theoretical results to experimental data has been achieved for a two-layer screen model having the following parameters, with the 40 m thick layer acting as screen:

h_1=55 m, V_{P1}=2600 m/s, V_{S1}=900 m/s, ρ_1=2.3 g/cm^3
h_2=40 m, V_{P2}=3800 m/s, V_{S2}=2000 m/s, ρ_2=2.5 g/cm^3

Theoretical amplitude curves of principal waves are displayed in *Fig. 9,* and the corresponding seismograms of the total field in *Fig. 10.* It should be noted that theoretical curves manifest the same type of changes with depth as the experimental curves (Fig. 8). In both of them, the field intensity increases with the distance from the bottom of the screen and with approaching the spot of recording the direct wave at 1000–1200 m depth. Immediately below the screen layer the *PSP*-wave is the most intense. In the model, the intensity of the screened wave is close to that of the direct sliding wave somewhere in the 900–1200 m interval. Precisely in this interval, screened wave kinematics does not differ from that of the direct wave, and together they generate an intense field. At short distances from the layer, the screened wave is of insignificant intensity. Consequently the characteristics of this wave do not allow its independent detection in a seismogram.

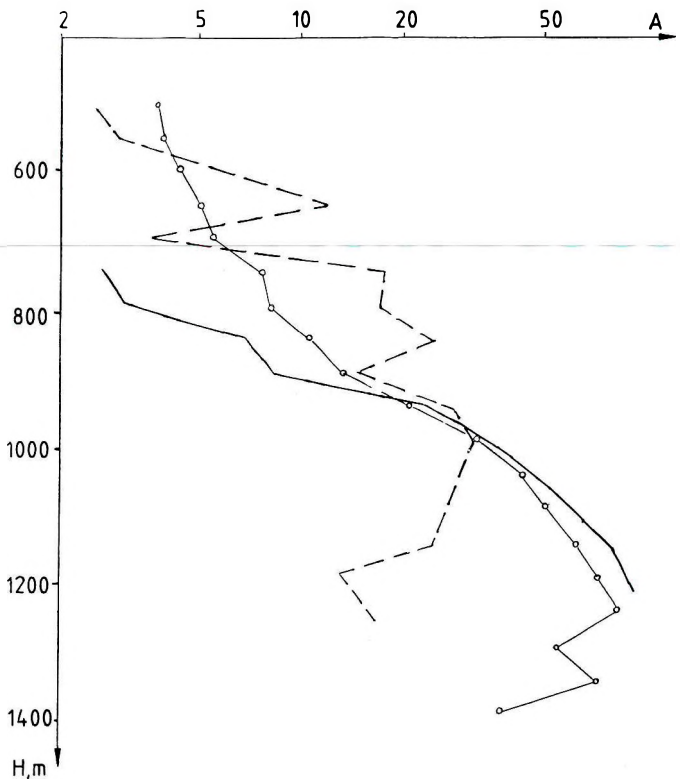

Fig. 9. Theoretical amplitude curves. Continuous line — direct *P*-wave; dashed line — *PSP*-wave; line with circles — screened wave

9. ábra. Elméleti amplitudó görbék. Folytonos vonal — direkt *P*-hullám; szaggatott vonal — *PSP*-hullám; körökkel jelölt vonal — árnyékolt hullám

Рис. 9. Теоретические амплитудные волн.
Сплосная линия – прямая волна *P*; штриховая линия – волна *PSP*;
линия с кружочками – экранированная волна.

The principal characteristics of the (theoretical and experimental) seismograms are in agreement with each other. A difference, however, can be noted which consists in different depth positions of maximum amplitudes. Attemps to eliminate this lack of agreement by varying the parameters of the high-velocity layer model have not given results. The disagreement between the seismograms is probably connected with the existence of high-velocity layers at depths of 600 and 800 m in the real sequence which are absent in the model.

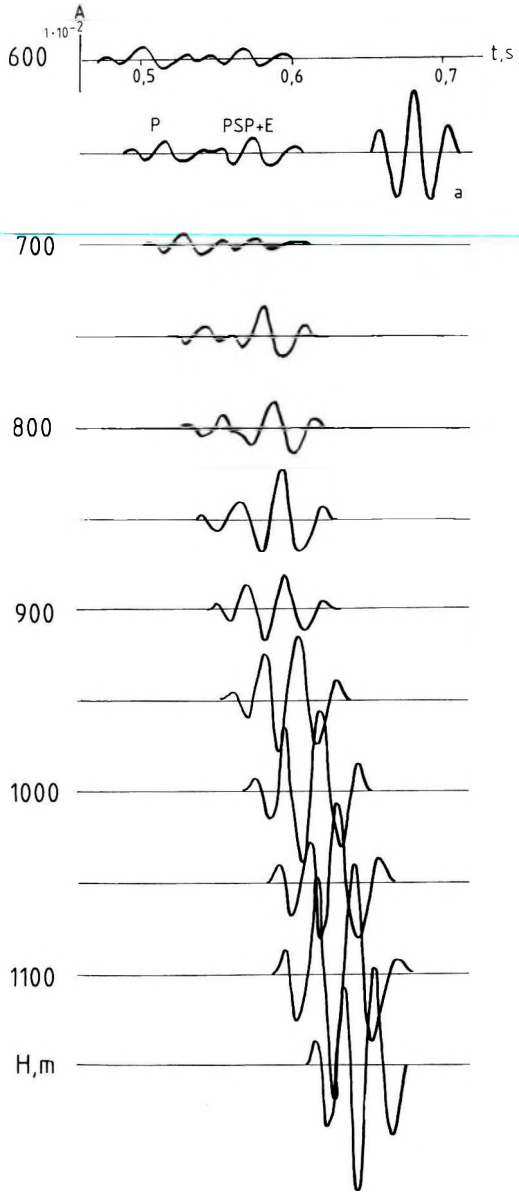

Fig. 10. Theoretical seismogram. a — wavelet used for direct wave

10. ábra. Elméleti szeizmogram. a — a direkt hullámhoz használt elemi jel

Рис. 10. Суммарная теоретическая сейсмограмма. а – форма прямой волны.

These layers may provide additional refraction. The real wave fields are generated by several screens. Moreover, screening and sliding are observable in the fields not only of down-going waves but also of reflected and refracted waves. It is suggested that near the critical angle the field of reflected waves — like that of the direct wave — splits into two parts during penetration through the high-velocity layer, viz. into a ray-type (*PSP*-wave) and a non-ray type part (screened wave). On the surface at a certain offset, one can observe that the reflected wave splits into two waves. The corresponding traveltime curve of the first break of the reflected wave has a higher apparent velocity than that of the second part. Using the model of the study area we calculated traveltime curves of reflected waves taking into account sliding and screening. The results of these calculations allow one to assess the distances at which the splitting into branches of the traveltime curves takes place and the degree of difference between the effective velocities determined from the branches.

Calculations for modelling conventional reflection seismology in a horizontally layered model have also been carried out. As an example, in *Fig. 11* traveltime curves of waves (i) reflected from the boundary of layer 2 in the middle of the sequence (Fig. 1) and (ii) reflected from a deep boundary (layer 5 in Fig. 1) are given. In this case, for one of the reflected waves the limestone layer, 1, is the screen while the corresponding screened wave is generated 1.5 km from the source. The deep reflected wave penetrates anhydrite layers 3 and 4 (Fig. 1) at angles which exceed the critical angle. On the surface, the accompanying screened wave is observable at a distance of 3 km from the source. The traveltime curve of this wave at a distance of 4 km deviates from the first breaks by 40 ms. Thus, in a simple form we can say that the second branch of the traveltime curve appeared. From VSP data, it seems that near the critical angle the intensity of the satellites, the *PSP*-waves and the screened waves brighten up and may generate additional branches of the traveltime curves. The location of this phenomemon may be displaced along the axis depending on the structure.

5. Conclusions

Investigations carried out have shown that if the angle of incidence of the direct wave and its satellites is close to the critical angle, an intense field of secondary waves arises below the high-velocity layer. It has been established that the origin of this field is connected with sliding and screening effects. The principal kinematic and dynamic characteristics of the waves composing the field were investigated. Although the major part of the study is based on VSP data we also used the same velocity model to calculate the moveout of reflected waves in the conventional CDP-technique.

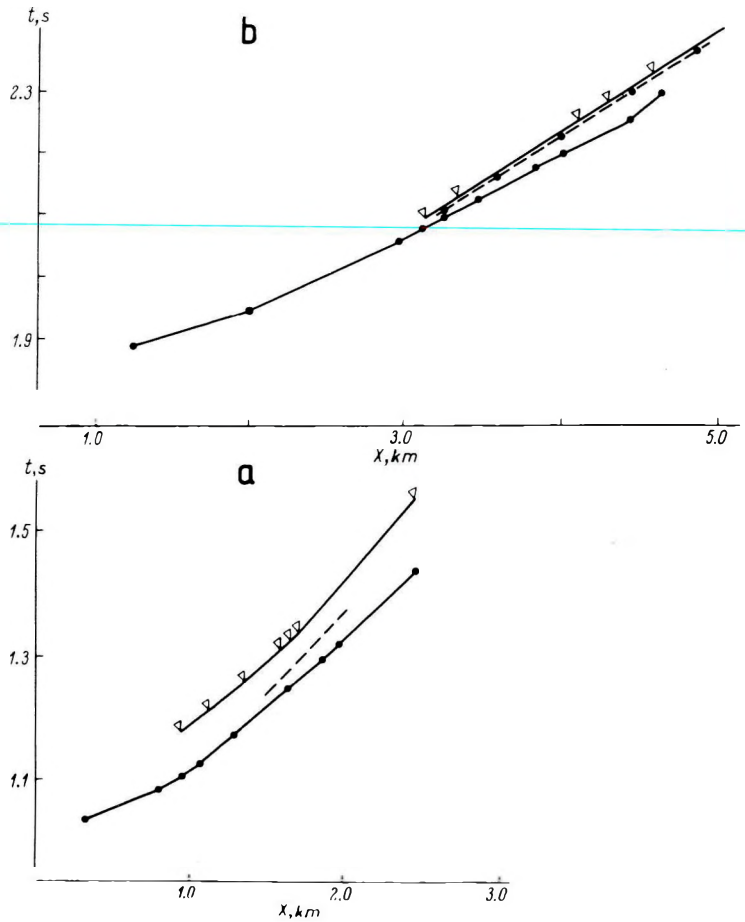

Fig. 11. Modelling of the conventional reflection method: calculated traveltime curves of reflected waves from layer 2 (a) and from layer 5 (b). Line with dots — reflected wave; dashed line — screened wave; line with triangles — *PSP*-wave

11. ábra. A hagyományos reflexiós módszer modellezése: a 2. rétegről reflektált hullámok számított út-idő görbéi (a) és ugyanezek az 5. rétegről (b). Pontokkal jelölt vonal — reflektált hullám; szaggatott vonal — árnyékolt hullám; háromszögekkel jelölt vonal — *PSP*-hullám

Рис. 11. Моделирование традиционного метода отраженных волн.
а) годографы отраженных волн от слоя 2; b) – то же, от слоя 5.
Линия с точками – лучевая отроженная волна;
штриховая – экранированная волна; линия с треугольниками – волна *PSP*.

REFERENCES

BERDENNIKOVA N. I., GOLIKOVA G. V., POGONYAYLO G. G., CHIZHOVA M. V. 1983: The use of polarization- and dynamic characteristics of seismic waves in boreholes (in Russian). Voprosy dinamicheskoy teorii rasprostraneniya seysmicheskikh voln, **XXII**, pp. 168–184

FAYZULLIN I. S. 1971: Modelling of thin high-velocity layers: reflected, refracted and head waves Izv. AN SSSR Fizika Zemli, **8**, pp. 12–22

GAMBURTSEV G. A. 1942: Correlation refraction method (in Russian). Izv. AN. SSSR, ser. geol. i geofiz., **2**, 1–2

GOLIKOVA G. V., BERDENNIKOVA N. I., POGONYAYLO G. G., CHIZHOVA M. V. 1982: The structure of the seismic wave field at different offsets (in Russian). Voprosy dinamicheskoy teorii rasprostraneniya seysmicheskikh voln, **XXII**, pp. 93–97

GOLIKOVA G. V., CHIZHOVA M. V. 1981: The influence of screening phenomena on the kinematics of different types of waves (in Russian). Voprosy dinamicheskoy teorii rasprostraneniya seysmicheskikh voln, **XX**, pp. 119–123

POGONYAYLO G. G. 1968: Study of the wave field in a borehole by offset VSP (in Russian). Voprosy dinamicheskoy teorii rasprostraneniya seysmicheskikh voln, **IX**, pp. 213–235

POGONYAYLO G. G., PETRASHEN G. I., MOLOTKOV L. A. 1974: The influence of thin high-velocity layers in the sedimentary sequence on the reflected wave field at large offsets (in Russian). Voprosy dinamicheskoy teorii rasprostraneniya seysmicheskikh voln, **XXII**, pp. 81–106

VORONIN Yu. A. 1959: Zero offset theoretical seismograms of reflected head- and screened waves (in Russian). Voprosy dinamicheskoy teorii rasprostraneniya seysmicheskikh voln, **III**, pp. 214–251

ÁRNYÉKOLÓ RÉTEG ALATTI HULLÁMTÉR VIZSGÁLATA

G. V. GOLIKOVA, M. V. CSIZSOVA és Ju. A. SZURKOV

1 km robbantási távolságú VSP során, nagy sebességű vékony réteg alatt észlelt hullámtér értelmezését ismertetjük. Bebizonyosodott, hogy ha a direkt hullám beesési szöge a nagy sebességű rétegen a kritikus szöghöz közeli, a direkt hullám két komponensre bomlik: egy sugár típusú direkt hullámra, amely „csúszó" hullámként hatol be a rétegbe, és egy „árnyékolt" hullámra. Ez utóbbit a konvertált *PSP* hullámmal együtt észleljük az első beérkezés után. Az értelmezésben felhasználtuk a hullámok polarizációs és dinamikus tulajdonságait, valamint elméleti számításokat végeztünk a hullámtér sugár-típusú, és nem-sugár-típusú összetevőire.

ОСОБЕННОСТИ ВОЛНОГО ПОЛЯ, ВОЗНИКАЮЩИЕ ПРИ ПРОХОЖДЕНИИ ВЫСОКОСКОРОСТНЫХ СЛОЕВ В ОБЛАСТИ ПРЕДЕЛЬНОГО УГЛА.

Г. В. ГОЛИКОВА, М. В. ЧИЖОВА, Ю. А. СУРКОВ

Приводятся результаты интерпретации волнового поля, зарегистрированного в скважине под слоем высокой скорости при возбуждении из источника, удаленного от устья скважины на один километр. Доказано, что в условиях эксперимента прямая волна падает на слой под углом близким к предельному. При этом она расщепляется на две части: лучевую прямую волну, скользящим образом прошедшую через слой и экранированную. Экранированная волна регистрируется совместно с обменном волной, волной *PSP* на некотором удалении от первых вступлений. Для интерпретации были использованы поляризационно-динамические характеристики волн, а также теоретические расчеты, проводившиеся как для лучевой части поля, так и нелучевой.

GEOPHYSICAL TRANSACTIONS 1990
Vol. 35. No. 4. pp. 243–252

THE USE OF SYMMETRY IN *f–k* MIGRATION

Einar MAELAND*

In order to speed up the classical *f–k* migration of zero-offset marine reflection data, a symmetrical data-set is artificially constructed, both in space and time. An efficient algorithm utilizes the discrete cosine transform, so only real variables are required. Since this yields a twofold decrease in computation time and storage requirements, no extra computer storage or working space other than the original data space is required. Moreover, since the discrete cosine transform effectively double the record length, computational artifacts caused by the discrete Fourier transform will be reduced.

Keywords: seismic data processing, *f–k* migration, discrete cosine transform, algorithm, real variables, computational artifacts

1. Introduction

The construction of an efficient algorithm for migration of zero-offset data is an important objective in seismic data processing. Migration by the classical *f–k* algorithm as given by STOLT [1978], is much faster than any other method, e. g., the phase-shift method [GAZDAG 1978], or the Kirchhoff summation [SCHNEIDER 1978]. In *f–k* migration, the spectrum is transformed from the frequency axis to the (vertical) wavenumber axis. To perform this (non-linear) mapping, some method of interpolation is required. Without any other information, both the real and the imaginary part of the *f–k* spectrum have to be interpolated. With respect to the amplitude and phase spectra, the interpolation errors of the phase spectrum (phase-errors) can be more troublesome than amplitude errors. An objective of the present study is to reduce the amount of this interpolation work.

Migration of zero-offset data is based upon the exploding reflector concept [LOEWENTHAL et al. 1976]. Based on this assumption, the data is equal to zero for time $t < 0$. If a function $f(t)$ is causal, i. e., $f(t) = 0$ for $t < 0$, the real and imaginary parts of the Fourier transform form a Hilbert transform pair [PAPOULIS 1977]. If, in addition, $f(t)$ is real, the real and imaginary parts of the Fourier transform are related to the cosine and sine transform of $f(t)$. If the real part of the Fourier transform is given, the imaginary part can in principle be found, and this latter part is redundant. Although zero-offset data are not "causal" in the horizontal space coordinates, it is possible (artificially) to construct symmetrical data without losing any information from the original data. As a consequence of this construction, the Fourier transform in wavenumber space will be real and even. Hence, it is possible to work entirely with a real spectrum, and many

*Seismological Observatory, University of Bergen, Allegt. 41, N–5007 Bergen, Norway
Manuscript received (revised version): 27 March, 1990

problems of computer storage and artifacts caused by interpolation of a complex spectrum can be avoided.

CARTER and FRAZER [1982] proposed a rapid method for f–k migration of zero-offset data. They used the fact that the Fourier transform of any real function is hermitian (conjugate even), which means that the real part of the Fourier transform is symmetric, while the imaginary part is anti-symmetric. The consequences are that certain parts of the f–k spectrum (negative frequencies) need not be stored in the memory of the host computer. Moreover, they also used a familiar trick such that in order to compute the Fourier transform of two real functions, $f(t)$ and $g(t)$, say, it is possible to compute the Fourier transform of the complex function $h(t) = f(t) + ig(t)$. The Fourier transform of $f(t)$ and $g(t)$ are then the hermitian (conjugate even) and the anti-hermitian (conjugate odd) part, respectively, of the Fourier transform of $h(t)$. However, if the input data are real and either even or odd, COOLEY et al. [1970] have shown that an even faster method exists to compute the discrete Fourier transform. Thus, the construction of symmetric zero-offset data in order to speed up the classical f–k migration warrants a closer study.

2. The f–k algorithm

In order not to overburden the present analysis with detail, only the 2-dimensional case will be studied. If the data (pressure) as a function of space (x) and time (t) are given by $P(x, t)$, imagine that a symmetric function $P(x, t)$ is constructed according to

$$P(-x, t) = P(x, -t) = P(-x, -t) = P(x, t). \tag{1}$$

Although this may at first sight seem to necessitate a much larger (four times) memory space than the original space, this is not the case. Let $x_n = n\Delta x$ and $t_m = m\Delta t$, where Δx and Δt are the (constant) sampling intervals along the x-axis and t-axis, respectively. A simple way to obtain the f–k spectrum is to perform a fast Fourier transform (FFT) column-by-column, and put the transformed data back into the memory $P(x_n, \omega_m)$, where ω_m is the frequency, then a FFT row-by-row, and put the transformed data back into the memory $P(k_n, \omega_m)$ where k_n is the wavenumber. This procedure presupposes a discrete Fourier transform of a working array $f_m = P(x_n, t_m)$, say. The procedure is then repeated in order to compute the discrete Fourier transform in the x-direction. Without any (symmetry) conditions of the input data, the spectrum will be complex, so extra memory space is required. However, if a symmetric working array (f_m) is constructed, then the Fourier transform becomes real and symmetric, and no extra memory in the host computer, beyond the original space $P(x_n, t_m)$, is required.

The Fourier series representation of any (periodic) real and symmetric function contains only real coefficients, which correspond to the cosine terms of the series. This result can be extended to the discrete Fourier transform. Consider a sequence $f_0(m)$ of length $2M-1$ (the odd-length symmetrical cosine transform), where $f_0(m) = f_m$ when $m \geq 0$, and $f_0(m) = f_{-m}$ when $m < 0$. The discrete Fourier transform of this sequence is

$$F_0(k) = \frac{1}{L} \sum_{1-M}^{M-1} f_0(m)\, exp[-2\pi ikm / (2M-1)], \tag{2}$$

for $|k| \leq M-1$, where $L = 2M-1$ is the total length of the sequence. Since $f_0(m)$ is real and symmetric, this relation reduces to

$$F_0(k) = \frac{1}{L} \sum_{m=0}^{M-1} \tilde{f}_m \cos[2\pi km/(2M-1)], \tag{3}$$

where $\tilde{f}_m$ is defined by $\tilde{f}_0 = f_0$ and $\tilde{f}_m = 2f_m$ for $1 \leq m \leq M-1$.

It is possible to compute the odd cosine transform with the discrete Fourier transform algorithm of odd length since

$$F_0(k) = \frac{1}{L} \mathbf{Real} \left\{ \sum_{m=0}^{M-1} \tilde{f}_m \exp[-2\pi imk/(2M-1)] \right\}. \tag{4}$$

The same result can be obtained if the sequence $\tilde{f}_m$ is extended by M zeros, viz., $\tilde{f}_m = 0$ for $m = M, M+1, \ldots, 2M-1$, and computing the DFT of length $2M-1$. This construction yields a causal sequence f_m (by definition).

In any application of the discrete Fourier transform, it is necessary to make a distinction between M even or M odd. The frequency interval is $\Delta\omega = 2\pi/L\Delta t$, and if M is odd, the Nyquist frequency $(\pi/\Delta t)$ is not attained by any $\omega_m = m\Delta\omega$, $|m| \leq M-1$. On the other hand, if M is even, a sample f_M at t_M must be included, so that $L = 2M$. In this case, however, the Nyquist frequency is attained when $m = \pm M$. In order to treat this case correctly, a "one-half" weight at the very last sample is utilized, i. e., $\frac{1}{2} f_M$ at $m = \pm M$.

The most common way to compute the $2M$-length (real) discrete Fourier transform is either to use a $2M$-length complex FFT, or by using a M-length complex FFT plus some additional operations. COOLEY et al. [1970] have shown that if the sequence (of length $2M$) is either even or odd, a simple procedure can be used to reduce the actual computation of the discrete Fourier transform to that of an $M/2$-length (complex) FFT with some preprocessing and postprocessing. An implementation of this procedure is given by RABINER [1979]. This yields a twofold decrease in storage since only half the real input data need be supplied. More details on the efficient computation of the discrete cosine transform are given by VETTERLI and NUSSBAUMER [1984]. Finally, an even more direct

method is to construct a DFT that works directly on 2-dimensional sampled data, but this technique will not be discussed.

Computing the real spectrum with the decrease of storage requirements may be summarized as follows:

```
Do while n ≥ 0 until  n=N–1
    f(0) = P[x(n), t(0)]
    do while m≥1 until m=M–1
        f(m) = P[(x(n), t(m)]
        f(2M–1–m) = f(m)
    end do
    f(m) = DFT[f(m)]
    do while m≥0  until m=M–1
        P[(x(n), ω(m)] = f(m)
    end do
End do
```

The procedure is repeated in order to compute the discrete Fourier transform in the x-direction.

3. Interpolation

Given the f–k spectrum, for each fixed value of the horizontal wavenumber (k_x), f–k migration is essentially a coordinate transformation from the frequency axis (ω) to the vertical wavenumber axis (k_z). In a two-dimensional study, this can be written $\omega / c \rightarrow k_z = \omega / c \cdot \cos(\alpha)$, where c is the velocity and α is the angle between the vertical axis and the direction of the plane waves. To perform this coordinate transformation, a suitable interpolation algorithm has to be used. The algorithm should not only be fast and simple, but also of high resolution. CARTER and FRAZER [1982] used a linear interpolation scheme, but since the f–k spectrum inevitably becomes periodic in any application of the discrete Fourier transform, it is more natural to use a periodic interpolation kernel. In this connection it is appropriate to note that for the construction of the odd symmetrical cosine transform, the addition of trailing zeros effects an interpolation of the spectrum. If Δt is the constant sampling interval, samples are taken at $t_m = m\Delta t$ where m = 0, 1, 2,..., M–1. The Nyquist frequency is then given by $\omega_{Ny} = \pi / \Delta t$. The discrete Fourier transform of a sequence of length M, say, yields a sampling interval in the frequency domain equal to $\Delta\omega = 2\pi / M\Delta t$. By application of the (odd symmetrical) cosine transform, the sampling interval is not changed, so the Nyquist frequency remains the same. However, since the record-length now (artificially) becomes $(2M–1)\Delta t$ the new sampling interval is $\Delta\tilde{\omega} = (2\pi / 2M–1)\Delta t$, or approximately half the original value. This very construction may make any further interpolation superfluous (nearest neighbour interpolation may in some cases be sufficient), but it may be more appropriate to interpolate in terms of cubic splines.

Interpolation by cubic splines is essentially by a low-pass action which incorporates some characteristics of sinc interpolation (Cardinal splines). For a fixed value of horizontal wavenumber, assume that f_m is the data at time $t_m = m\Delta t$, and let the discrete Fourier transform of this sequence be denoted by F_m. Interpolation by cubic spline can be written

$$H(\omega) = \sum A_m B(\omega - m\Delta\omega), \tag{5}$$

where $B(\omega)$ is the cubic B-spline and A_m are coefficients to be determined from the condition that $H(\omega_m) = F_m$. Among a variety of algorithms available in the literature, the algorithm given by FORD [1975] can be recommended, both for its simplicity and for its efficiency, but strictly speaking, the results are only approximately correct. In the present case it is possible to take advantage of the fact that the interpolation is carried out in the frequency domain. Thus, the results can be obtained with even less efforts, but the actual details are given in the Appendix.

The processing part of f–k migration is a mapping from the $(k_x\,\omega)$-domain to the (k_x, k_z)-domain. Let Ω be defined by $\Omega / c = k_z$, where c is the migration velocity. Assume that the f–k spectrum is given at $k_n = n\Delta k$ and $\omega_m = m\Delta\omega$, where Δk and $\Delta\omega$ are, respectively, the sampling interval in the wavenumber and frequency domain. Then for each k_n and ω_m the values of the frequency $\Omega(k_n, \omega_m)$ are required. The mapping is governed by the equation

$$(\Omega / c)^2 = (m\Delta\omega / c)^2 - (n\Delta k)^2. \tag{6}$$

This transformation represents, for a fixed k_n, a shift of data from frequency ω_m to a lower frequency Ω [STOLT 1978]. It is important to achieve $\Omega = j\Delta\omega$, $j = 0, 1, \ldots, M$, hence, interpolation is necessary. However, for any value of k_n, some values of the original frequency (ω_m) may give an imaginary Ω-value. But the Ω is supposed to be real, i. e., the evanescent part of the wave field is excluded. If an imaginary Ω-value is obtained, the corresponding value of the spectrum is put equal to zero.

4. Illustrative examples

A comparison of the proposed algorithm with the conventional FFT-method [STOLT 1978] will be made. The input signal is a zero phase Ricker walvelet, i. e., the second derivative of the function $f(t) = \exp[-2(t/t_0)^2]$, with $t_0 = 0.05$ sec. Moreover, the velocity is $c = 1$ km/sec, while the record lengths are $X = 3$ km and $T = 2$ sec. Three "spikes" are present in the input data set, located at $x_A = 1.5$ km, but at different times $t_A = 0.75$, 1.0 and 1.25 sec, respectively. The migrated

output with the conventional FFT-method is displayed in *Fig. 1.* The impulse response is ideally a semi-circle (the exploding reflector) centred at $z = 0$, with a radius equal to $ct_A = 0.75$, 1.0 and 1.25 km, respectively. The most conspicuous artifacts in the conventional FFT-method are the (inverted) semi-circles. Due to the periodicity of the discrete Fourier transform, the computational artifacts are (inverted) semi-circles of radii $r = c(T - t_A)$, centred at the bottom ($z = cT$). Other artifacts are also present (circles centred at $x_A \pm cT$), but they are hardly visible due to geometrical spreading. The corresponding results with the proposed algorithm are displayed in *Fig. 2.* This method effectively doubles the record length hence, due to geometrical spreading, the amplitude of the computational artifacts is reduced.

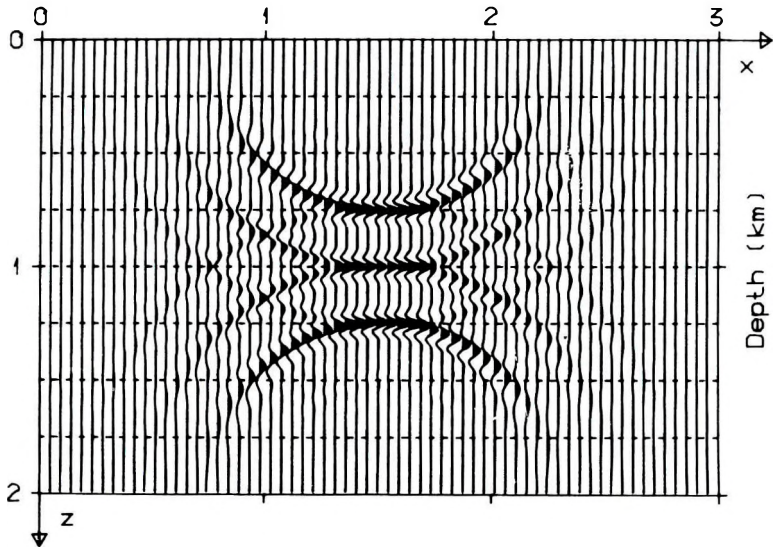

Fig. 1. Migrated output (impulse response) with the conventional FFT-method. The (inverted) semi-circles are the computational artifacts, which are strongly in evidence

1. ábra. A hagyományos FFT-t alkalmazó migráció impulzus válaszfüggvénye. Az (invertált) félkörök a számítás melléktermékei

Рис. 1. Резонансная импульсная функция миграции с традиционным ускоренным преобразованием Фурье.
(Обращенные) полукруги – побочный результат расчетных операций

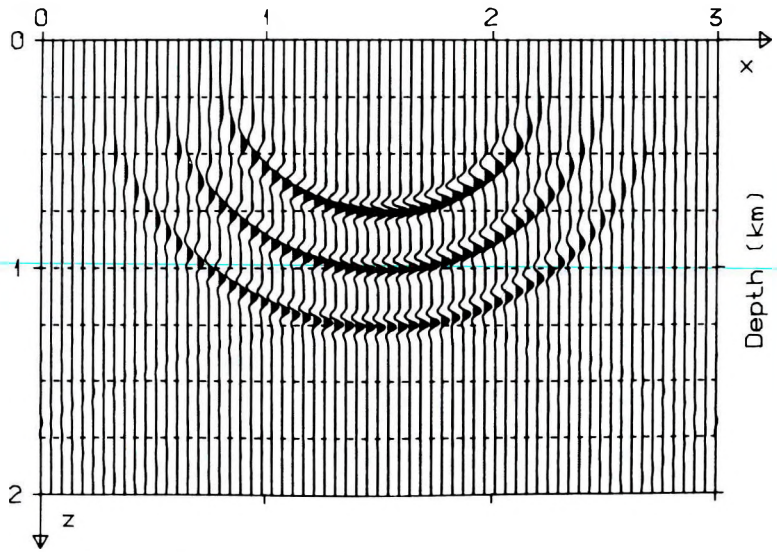

Fig. 2. Migrated output (impulse response) with the proposed method. Computational artifacts are still present, but the amplitudes are reduced due to geometrical spreading

2. ábra. A javasolt migrációval nyert impulzus válaszfüggvény. A számítási melléktermékek amplitúdói lényegesen csökkentek a szférikus divergencia következtében

Рис. 2. Резонансная импульсная функция, полученная при предлагаемом варианте миграции. Амплитуды побочных результатов расчетных операций существенно снизились вследствие сферической дивергенции

5. Conclusion

When migrating zero-offset reflection data for the first time, it is not so important to use a migration technique that is the best possible. Rather, a quick *f–k* migration can be used without running the risk of spending too much time looking for an exact velocity fit. The process of (artificially) constructing symmetric zero-offset data is used as an alternative to the classical *f–k* migration. The advantages are that it is possible to work entirely with real variables, hence, there is no need for extra working space to store the *f–k* spectrum in the host computer. The actual computation of the (real) *f–k* spectrum can be done by utilizing an efficient algorithm such as that of COOLEY et al. [1970].

By application of the discrete Fourier transform, the migrated output will be periodic. Hence, computational artifacts will inevitably make their appearance. Since the impulse response is a semi-circle, the artifact will be (inverted) semi-circles. A method to reduce these artifacts is to use a longer record length in time (trailing the data set with zeros). The proposed method utilizes a symmetrical data set, which essentially incorporates some of this technique.

Consequently, it is possible to take advantage of even more symmetry properties than originally proposed by CARTER and FRAZER [1982].

Appendix

Periodic cubic B-spline

The cubic B-spline is a polynomial approximation to a function $f(t)$, say, where the samples $f_m = f(m\Delta t)$ are given for $|m| \leq M-1$, where Δt is the constant sampling interval. It will be assumed that the input sequence is periodic, i. e., $f_{m+L} = f_m$, where $L = 2M-1$.

Let a function $h(t)$ be constructed according to

$$h(t) = \sum_{1-M}^{M-1} a_m \, B(t-t_m), \tag{A-1}$$

where $B(t)$ is the B-spline or Parzen window, while a_m are coefficients to be determined from the imposed condition that $h(t_m) = f_m$. Moreover, in order that $h(t)$ should be periodic, $h(t + L\Delta t) = h(t)$, the coefficients a_m are forced to be periodic too, $a_{m+L} = a_m$, but it is not necessary to put any restriction on function $B(t)$. Returning to the B-spline form $B(t)$, this function is non-zero over 3 sample points, with $B(0) = 1$, $B(\pm\Delta t) = 1/4$, while $B(\pm m\Delta t) = 0$ when $m > 1$. The claim that $h(t_m) = f_m$ yields the key equations

$$a_{m-1} + 4\,a_m + a_{m+1} = 4\,f_m. \tag{A-2}$$

According to these equations the coefficients a_m used to weight the spline functions are related to f_m by a banded (tridiagonal) circulant matrix. The inversion of this matrix can be accomplished by using Fourier matrix techniques, i. e., the diagonalization property of circulant matrices. The inverse matrix is also circulant, but not banded. However, when M is large, the asymptotic values of the coefficients in this (inverse) matrix are effectively independent of M. According to FORD [1975], the periodic nature of the problem allows it to be expanded (with no loss of accuracy) as if $M \to \infty$.

The construction of the coefficients a_m warrants a closer study. It may be appropriate to study the discrete Fourier transform of equation (A-2), and the result is

$$A_k = 2F_k / [2 + \cos(2\pi k / L)], \tag{A-3}$$

where A_k and F_k are the discrete Fourier transforms of a_m and f_m, respectively. The coefficients a_m are then given by the inverse discrete Fourier transform

$$a_m = \sum_{1-M}^{M-1} A_k \cdot \exp(2\pi i k m / L). \qquad \text{(A–4)}$$

If f_m is an impulse at $m = 0$, then $F_k = 1$ for all values of the index k (the impulse response). Let the corresponding discrete Fourier coefficients be denoted by D_k

$$D_k = 2 / [2 + \cos(2\pi k / L)], \qquad \text{(A–5)}$$

which are real and even, i. e., $D_{-k} = D_{+k}$. In this way interpolation can be accomplished by the discrete Fourier transform and its inverse, respectively. The coefficients a_m can be obtained by first taking the discrete Fourier transform $F_k = \mathrm{DFT}\{f_m\}$ multiplying by D_k, and finally taking an inverse DFT to obtain $a_m = \mathrm{IDFT}\{F_k \cdot D_k\}$

The processing part of *f–k* migration is essentially an interpolation on the frequency axis. The "simplest" way is to take a DFT in space to obtain $P(k_n, t_k)$, then a DFT in time to obtain $P(k_n, \omega_m)$. At this very step an interpolation as indicated by equation (A–1) must be performed. However, to obtain the coefficients a_m, imagine that $P(k_n, t_k)$ is multiplied by the filter coefficients D_k, followed by a DFT. Then the next step is to perform the convolution, which is nothing but an evaluation of a polynomial at the desired frequency values. The final step is to transform back to time and space coordinates to achieve the migrated output. This procedure may be considered as an alternative method to the algorithm given by FORD [1975].

REFERENCES

CARTER J. A. and FRAZER L. N. 1982: Rapid *f–k* migration of zero-offset marine reflection data. Journal of Geophysical Research **87**, (B11), pp. 9365 – 9373

COOLEY J. W., LEWIS P. A. and WELCH P. D. 1970: The fast Fourier transform algorithm: Programming considerations in the calculating of sine, cosine and Laplace transforms. Journal of Sound and Vibrations **12**, pp. 315 – 337

FORD W. S. 1975: Periodic cubic spline interpolation with equidistant nodes. The Computer Journal **18**, pp. 183 – 184

GAZDAG J. 1978: Wave equation migration with the phase-shift method. Geophysics **43**, 7, pp. 1342 – 1351

LOEWENTHAL D., LU L., ROBERSON R. and SHERWOOD J. 1976: The wave equation applied to migration. Geophysical Prospecting **24**, 2, pp. 380 – 399

PAPOULIS A. 1977: Signal Analysis, McGraw-Hill Book Co.

RABINER L. R. 1979: On the Use of Symmetry in FFT Computations. IEEE Trans. Acoust., Speech, Signal Proc. **27**, pp. 233 – 239

SCHNEIDER W. A. 1978: Integral formulation for migration in two and three dimensions. Geophysics **43**, 1, pp. 49 – 76

STOLT R. H. 1978: Migration by Fourier Transform. Geophysics **43**, 1, pp. 23 – 48

VETTERLI M. and NUSSBAUMER H. J. 1984: Simple FFT and DCT algorithms with reduced number of operations. Signal Processing **6**, pp. 267 – 278

AZ *f–k* MIGRÁCIÓ SZIMMETRIÁJÁNAK HASZNOSÍTÁSA

Einar MAELAND

Dinamikusan korrigált, tengeri reflexiós szeizmikus anyag hagyományos *f–k* migrációjának felgyorsítására térben és időben szimmetrikus adatrendszert hoznak létre. Egy hatékony algoritmust közölnek, amely a cosinus transzformációt használja, ezért csak valós változókra van szükség. Ez csökkentést jelent mind gépidőben, mind tárolási kapacitásban, így nincs szükség csak az eredeti adatok által foglalt tárolókapacitásra. Sőt, mivel a cosinus transzformáció megkétszerezi a rekordhosszt, a diszkrét Fourier-transzformáció okozta művi jelek amplitúdója nagymértékben csökken.

УТИЛИЗАЦИЯ СИММЕТРИИ *f–k* МИГРАЦИИ

Эйнар МЕЙЛАНД

Для убыстрения традицинной *f–k* миграции материалов морской сейморазведки МОВ с динамической поправкой создается система данных, симметричная в пространстве и во времени. Приводится эффективный алгоритм, в котором используется косинусное преобразование, поэтому он нуждается лишь в реальных переменных. Это приводит к сокращению как машинного времени, так и емкости памяти, так что отпадает необходимость в памяти для первичных данных. Более того, посколъку при косинусном преобразовании удваивается длина записей, значительно уменьшается амплитуда искусственных сигналов, появляющихся при дискретом преобразовании Фурье.

GEOPHYSICAL TRANSACTIONS 1990
Vol. 35. No. 4. pp. 253–272

GENERALIZED COMPLEX ATTRIBUTES AND THEIR USE FOR NMO STRETCHING COMPENSATION

A. VESNAVER* and F. POLETTO*

Normal Move Out (NMO) correction in the space–time domain is carried out as a time-varying stretching of the seismic trace. The basic limit of this procedure is that early reflections at large offsets are greatly deformed and must be muted before stacking. Although the stack itself can be performed satisfactorily in other domains (such as the f–k), other processing steps such as residual statics require NMO corrected traces. This paper introduces an algorithm able to compensate for NMO stretching. Generalized complex attributes are defined which cast light on various spectral properties of NMO correction. Finally applications to synthetic and real data are discussed.

Keywords: seismic data processing, NMO-correction, seismic attributes, Hilbert transform, envelope, instantaneous phase

1. Introduction

Correction for Normal Move Out (NMO) is the basic preliminary to the stacking of Common Mid Point (CMP) gathers. However, if this operation is performed in the space–time domain, the well-known undesired effect of stretching arises for early reflections at large offsets *(Fig. 1)*. The usual remedy is a surgical mute, which removes the overstretched wavelets and thus reduces the distortion of the stacked signals, but precious information is lost in this way.

Better solutions have been investigated over the last decade, mainly by defining stack procedures in new domains, such as the frequency–wavenumber [GAZDAG and SGUAZZERO 1984]. These new techniques, however, have two major limitations: firstly, they require expensive two-dimensional transforms; secondly, they solve the problem of stacking but not that of NMO correction: in fact, although the summing of coherent signals is the ultimate goal of this procedure, there are numerous processing steps which are executed after NMO correction and before stacking in the space–time domain, such as residual statics, residual NMO, surface consistent deconvolution, mute scans, etc.

In this paper an algorithm is introduced which is able to compensate for NMO stretching based on the concepts of a complex trace [TANER et al. 1979] and phase gain [SGUAZZERO and VESNAVER 1987]. The algorithm requires the definition of new complex attributes generalizing the classical ones, such as instantaneous phase, envelope and instantaneous frequency.

*Osservatorio Geofisico Sperimentale (OGS), POB 2011, 34016 Trieste, Italy
Manuscript received (revised version): 29 November, 1989

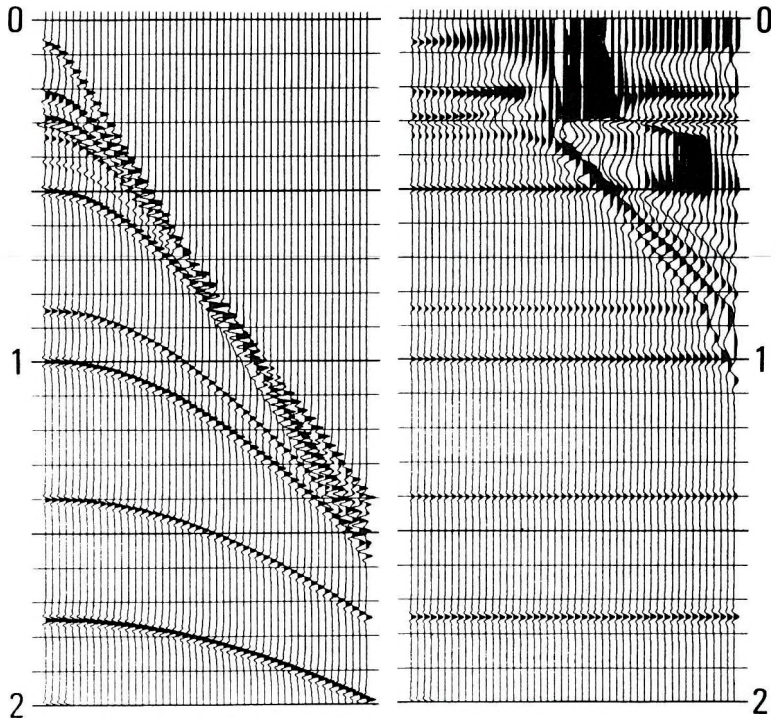

Fig. 1. Synthetic CMP gather before (left) and after (right) NMO correction

1. ábra. Szintetikus közös középpontos gyűjtés dinamikus korrekció előtt (bal) és után (jobb)

Рис. 1. Синтетический сбор по общей точке до (слева) и после (справа) динамической поправки

2. Generalized complex attributes

Before introducing the proposed algorithm to compensate for NMO stretching, we need to define some old and new attributes of the complex trace.

Definition of attributes

Given a real trace $r(t)$, its corresponding complex trace $c^{(1)}(t)$ is defined as:

$$c^{(1)}(t) \equiv r(t) + \mathrm{i}\, \mathbf{H}\{r(t)\} \tag{1}$$

where $\mathbf{H}\{\cdot\}$ indicates the Hilbert transform. We can express in exponential form:

$$c^{(1)}(t) = e^{(1)}(t) \exp[\mathrm{i}\Phi^{(1)}(t)] \tag{2}$$

where

$$e^{(1)}(t) \equiv |c^{(1)}(t)| \tag{3}$$

and

$$\Phi^{(1)}(t) \equiv \mathrm{Arg}\{c^{(1)}(t)\}$$

Expressions (3) are the definitions of the well-known envelope and instantaneous phase, respectively. They are what we call *first order attributes* in this paper, as emphasized by the superscripts. We can define *second order attributes* as follows.

Envelope $e^{(1)}(t)$ may be regarded as a real-valued trace. So a complex trace $c^{(2)}(t)$ may be defined in a similar way as in (1):

$$c^{(2)}(t) = e^{(1)}(t) + i\mathbf{H}\{e^{(1)}(t)\} = e^{(2)}(t)\exp[i\Phi^{(2)}(t)] \tag{4}$$

where $e^{(2)}(t)$ and $\Phi^{(2)}(t)$ are the second order envelope and instantaneous phase, respectively:

$$e^{(2)}(t) \equiv |c^{(2)}(t)|$$

$$\Phi^{(2)}(t) \equiv \mathrm{Arg}\{c^{(2)}(t)\} \tag{5}$$

i. e. $e^{(2)}(t)$ is the envelope of envelope $e^{(1)}(t)$. Generalizing Eqs. (4) and (5) we obtain:

$$c^{(j+1)}(t) = e^{(j)}(t) + i\mathbf{H}\{e^{(j)}(t)\} = e^{(j+1)}(t)\exp[i\Phi^{(j+1)}(t)]$$

$$e^{(j)}(t) \equiv |c^{(j)}(t)|$$

$$\Phi^{(j)}(t) \equiv \mathrm{Arg}\{c^{(j)}(t)\} \tag{6}$$

These recursions, together with Eq. (1), define the *generalized complex attributes* of the real trace $r(t)$.

Figure 2 displays a simple synthetic trace composed of two zero-phase waveforms of opposite polarity. The first order envelope and instantaneous phase are superimposed. We notice that where there is the main lobe of the positive wavelet, the instantaneous phase is close to zero, while in correspondence to the main lobe of the negative wavelet the phase is discontinuous. This fact will be considered again later.

Figure 3 shows higher order envelopes of the same data. When the envelope order increases, the curves are smoother, particularly near the envelope maxima, i. e. where the signal energy is significant. *Figure 4* shows higher order instantaneous phases of these data. We notice two relevant features: firstly, all

curves intersect each other approximately where there are the two maxima of the envelopes in Figure 2; secondly, in proximity to these intersection points the curves display a linear trend.

Higher order complex attributes have been introduced principally for their mathematical usefulness (as shown in the following paragraph), but they do not seem to have immediate physical significance. Nevertheless, we can emphasize that they share the basic properties of first order complex attributes, due to the nature itself of the Hilbert transform; in particular, any value of the computed complex trace depends on all values of the real trace, and not only on the single value at the corresponding arrival time. This characteristic allows the physical continuity of the whole wave propagation phenomenon to be comprised in the algorithms based on complex traces, exploiting the information redundancy in the data, which redundancy is due to the physical constraints obeyed by the data.

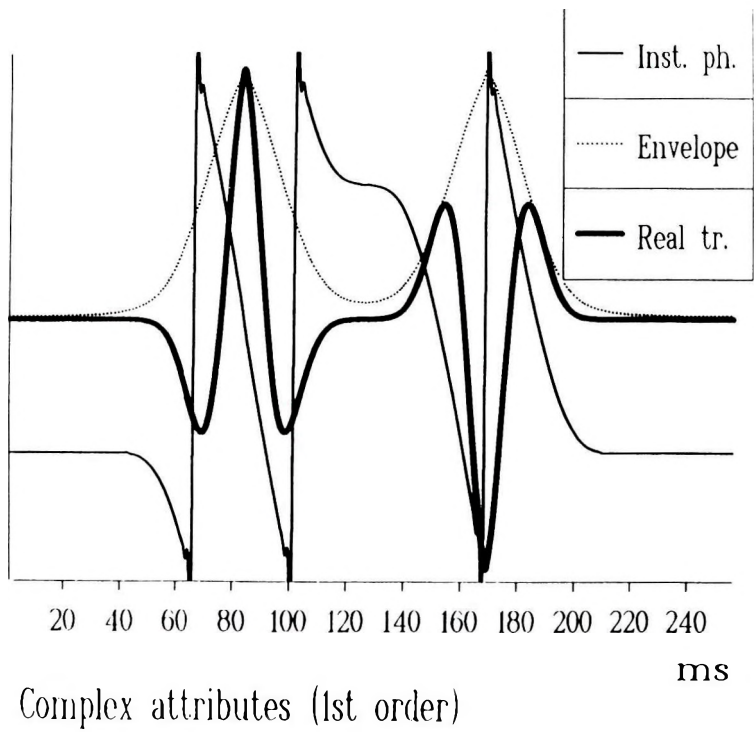

Fig. 2. First order complex attributes of a simple synthetic trace (heavy solid line): envelope (dotted line) and instantaneous phase (solid line)

2. ábra. Szintetikus szeizmogram (vastag vonal) elsőfokú komplex attributumai: burkoló (pontozott) és pillanatnyi fázis (folyamatos vonal)

Рис. 2. Комплексные характеристики первого порядка синтетической сейсмограммы (жирная линия): объемлющая (точки) и мгновенная фаза (сплошная)

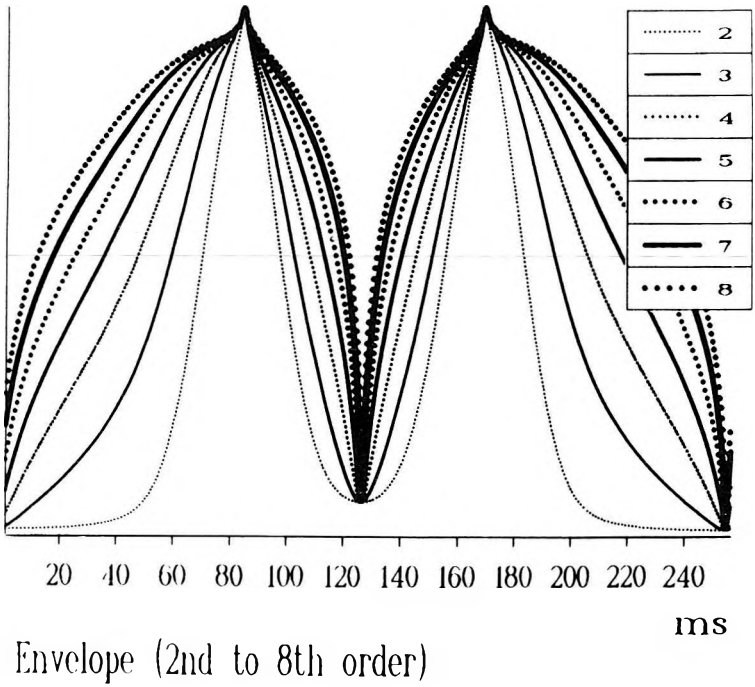

Fig. 3. Second to eighth order envelopes of the trace in Fig. 2

3. ábra. Szintetikus szeizmogram (2. ábra) burkolója (másodfokútól nyolcadfokú közelítésig)

Рис. 3. Обьемлющая (приближения от второго до восьмого порядка) синтетической сеймограммы (рис. 2)

Complex trace expansion

We are going now to use these generalized complex attributes to express the real trace $r(t)$ in a suitable form to compensate for NMO stretching. From definitions (1) and (2) it follows that:

$$r(t) = \mathrm{Re}\{c^{(1)}(t)\} = e^{(1)}(t)\cos[\Phi^{(1)}(t)] \tag{7}$$

Similarly:

$$e^{(1)}(t) = \mathrm{Re}\{c^{(2)}(t)\} = e^{(2)}(t)\cos[\Phi^{(2)}(t)] \tag{8}$$

Substituting $e^{(1)}(t)$ in (7) using (8) we get:

$$r(t) = e^{(2)}(t)\cos[\Phi^{(2)}(t)]\cos[\Phi^{(1)}(t)] \tag{9}$$

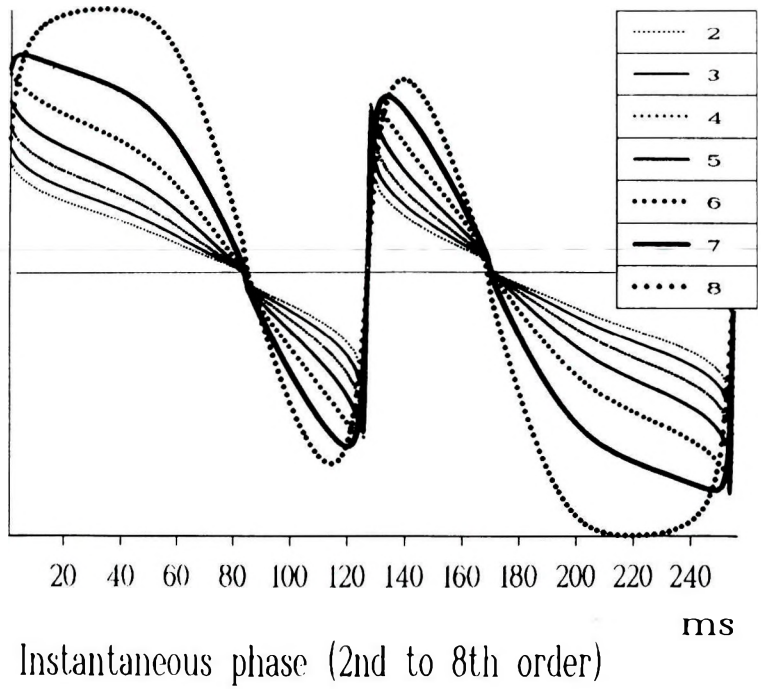

Fig. 4. Second to eighth order instantaneous phases of the trace in Fig. 2

4. ábra. Szintetikus szeizmogram (2. ábra) pillanatnyi fázisa (másodfokútól nyolcadfokú közelítésig)

Рис. 4. Мгновенная фаза (приближения от второго до восьмого порядка) синтетической сейсмограммы (рис. 2)

Substituting iteratively envelopes $e^{(j)}(t)$ in Eq. (9) using recursions Eq. (6) we finally obtain:

$$r(t) = e^{(N)}(t)\cos[\Phi^{(N)}(t)]\cos[\Phi^{(N-1)}(t)]\ldots\cos[\Phi^{(1)}(t)] \tag{10}$$

where N is an arbitrary integer number. If N is relatively large, the N-th order envelope $e^{(N)}(t)$ is relatively smooth where the energy of $r(t)$ is significant. So the main value of Eq. (10) is that most information is contained in the generalized instantaneous phases $\Phi^{(j)}(t)$.

We can now expand the $\Phi^{(j)}(t)$ functions by a first order Taylor series:

$$\Phi^{(j)}(t) \approx \Phi^{(j)}(\tilde{t}) + (t-\tilde{t})\frac{\mathrm{d}}{\mathrm{d}t}[\Phi^{(j)}(t)]_{t=\tilde{t}} = \Phi^{(j)}(\tilde{t}) + \tau\Gamma^{(j)}(\tilde{t}) \tag{11}$$

where $\tilde{t}$ is an arbitrary arrival time, and $\Gamma^{(j)}(t)$ is the j-th order *instantaneous frequency:*

$$\Gamma^{(j)}(t) \equiv \frac{\mathrm{d}}{\mathrm{d}t}[\Phi^{(j)}(t)] \tag{12}$$

If $\tilde{t}$ is chosen as the time of the maximum of the positive zero-phase wavelet, then $\Phi^{(j)}(\tilde{t})$ is close to zero and equation (11) is simplified:

$$\Phi^{(j)}(t) \approx \tau\, \Gamma^{(j)}(\tilde{t}) \tag{13}$$

At minima of negative zero-phase wavelets, for the first order function the following relation holds:

$$\Phi^{(1)}(t) \approx \pi + \tau\, \Gamma^{(1)}(\tilde{t}) \tag{14}$$

but by removing the *apparent polarity* (see Appendix A) we obtain that all instantaneous phases $\Phi^{(j)}(t)$ of all wavelets in the seismogram $r(t)$ may be expanded as in Eq. (13). However, we will have to restore the initial apparent polarity as the last step in the procedure we are defining.

Substituting Eq. (13) into Eq. (10) we can finally express the seismic trace $r(t)$ as follows:

$$r(t) = e^{(N)}(t)\prod_{j=1}^{N}\cos[\Phi^{(j)}(t)] \approx e^{(N)}(t)\prod_{j=1}^{N}\cos[\tau\Gamma^{(j)}(\tilde{t})] \tag{15}$$

Equation (15) is in a very convenient form to apply NMO-stretching compensation.

3. NMO stretching description

The NMO stretching effect was described by DUNKIN and LEVIN [1973]. Since their equations provide the basis for this paper, we recall briefly their results in this section.

Time domain

The arrival time t_x of a signal from a given reflector is a function of the offset x between source and receiver. If we assume that the earth is horizontally layered, this function is the well known Move Out hyperbola:

$$t_x = [t_0 + x^2/v^2(t_0)]^{1/2} \tag{16}$$

where $v(t_0)$ is the stacking velocity at zero-offset time, t_0. In particular, equation (16) relates the arrival time t_x of the signal recorded at offset x with t_0, which is the arrival time of the same signal after NMO correction, when all reflections from the same reflecting point are moved to zero offset.

Expanding $t_0 = t_0(t_x)$ by a Taylor series of the first order, we may express t_0 as a linear function of t_x:

$$t_0 \approx \tilde{t}_0 + [t_x - \tilde{t}_x]\,[\mathrm{d}t_0/\mathrm{d}t_x] \tag{17}$$

where:

$$\frac{\mathrm{d}t_0}{\mathrm{d}t_x} = \frac{\tilde{t}_x}{\tilde{t}_0}\,\frac{1}{\{1 - [x^2/(\tilde{t}_0\, v^3)]\,\mathrm{d}v(\tilde{t}_0)/\mathrm{d}t_0\}} = \sigma \tag{18}$$

$$\tilde{t}_x = [\tilde{t}_0^2 + x^2/v^2(\tilde{t}_0)]^{1/2} \tag{19}$$

We denote by $\tilde{t}_x$ the origin of the Taylor series expansion at the wavelet centre in a trace with offset x *(Fig. 5)*, and σ is a stretching factor greater than 1, which depends on offset, time, stacking velocity and its time derivative: $\sigma = \sigma(x, t_0, v(t_0), \mathrm{d}v(t_0)/\mathrm{d}t_0$. Manipulating Eq. (17) and substituting Eq. (18) we have:

$$\tau_0 = t_0 - \tilde{t}_0 \approx \sigma[t_x - \tilde{t}_x] = \sigma\,\tau_x \tag{20}$$

The variable τ_x is the *local time* in the reference frame of the series expansion at offset x. Equation (20) means that, within a first order approximation, *NMO correction is a local time expansion.* In fact, if Dt_0 and Dt_x are the sampling intervals at offset 0 and x, then from (20) we get:

$$Dt_0 = \sigma Dt_x \tag{21}$$

Equation (21) emphasizes that NMO correction requires a time-varying sampling of traces at offset x. The values sampled at offsets x from an irregular hyperbolic grid are then translated into a different regular grid at offset 0 *(Fig. 6)*.

Frequency domain

Some simple relations between wavelet spectra before and after NMO stretching may be demonstrated in the frequency domain. If f_0 and f_x are the local frequencies associated with local times τ_0 and τ_x, we get from Eq. (20):

$$f_0 = 1 / \tau_0 = 1 / (\sigma \tau_x) = f_x / \sigma \tag{22}$$

Furthermore, since NMO correction changes the shape but not the amplitudes of the waveform w_x, then:

$$w_0(\tau_0) = w_x(\tau_x) \tag{23}$$

Substituting (20) in (23), we obtain:

$$w_0(\tau_0) = w_x(\tau_0 / \sigma) \tag{24}$$

Exploiting the shift-theorem and using Eqs. (20) to (24), we get finally:

$$W_0(f_0) = \sigma W_x(\sigma f_0) = \sigma W_x(f_x) \tag{25}$$

Equations (22) and (25) mean that NMO stretching produces a scaling of the waveform spectrum and a remapping of frequencies into lower bands, since $\sigma \geq 1$.

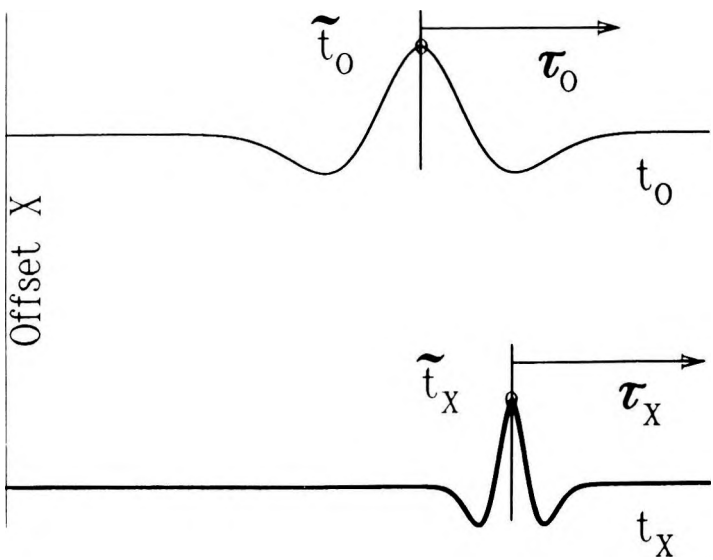

Fig. 5. Zero-phase wavelet at offset x (lower part) is converted to offset 0 by NMO correction (upper part). The stretching effect is evident

5. ábra. x észlelési távolságú elemi jel (alul) és ennek dinamikus korrekció utáni alakja (felül). A nyújtó hatás egyértelműen látszik

Рис. 5. Элементарный сигнал (внизу) и ее вид после динамической поправки (вверху) при расстоянии x между источником и приемником. Однозначно отмечается эффект удлинения

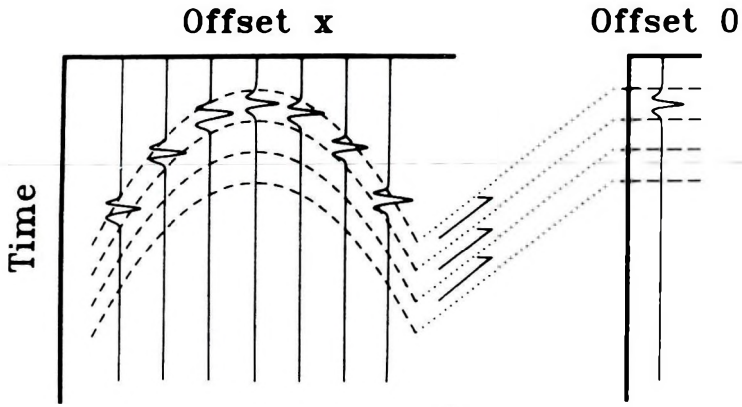

Fig. 6. Time varying sampling of a trace at offset x mapped to offset 0

6. ábra. x észlelési távolságú csatorna időben változó mintavételezésének transzformálása 0 észlelési távolságra

Рис. 6. Приведение дискретности, переменной во времени, трассы с расстоянием x между источником и приемником к расстоянию 0 между источником и приемником

4. NMO stretching compensation

Mathematical formulation

NMO stretching compensation may be performed as a correction for wavelet spectrum compression in the frequency domain — (as described above in Eq. (25)). To this end, we recall the definition of instantaneous spectrum $S_x(t_x, f_x)$ [e. g. ACKROYD 1970]:

$$S_x(t_x, f_x) = r_x(t_x)\, R_x^*(f_x) \exp(-2\pi i f_x t_x) \tag{26}$$

where the asterisk indicates a conjugation. A useful expression relating the first moment of the instantaneous spectrum $S_x(t_x, f_x)$ (i. e., its centroid abscissa) and instantaneous frequency $\Gamma_x(t_x)$ can be demonstrated:

$$\Gamma_x(t_x) = \mathrm{Re}\left|\frac{\int_{-\infty}^{\infty} f_x S_x(t_x, f_x)\,\mathrm{d}f_x}{\int_{-\infty}^{\infty} S_x(t_x, f_x)\,\mathrm{d}f_x}\right| \tag{27}$$

Using (20), (22), (23) and (25), we get:

$$\Gamma_x(t_x) = \mathrm{Re}\left|\frac{\int_{-\infty}^{\infty} \sigma f_0 S_0(t_0, f_0)\,\mathrm{d}f_0}{\int_{-\infty}^{\infty} S_0(t_0, f_0)\,\mathrm{d}f_0}\right| = \sigma\,\Gamma_0(t_0) \tag{28}$$

which also expresses the shift of the instantaneous spectrum centroid towards a lower frequency due to NMO correction. To move the centroid back towards its original frequency, we have to multiply $\Gamma_0(t_0)$ by σ:

$$\bar{\Gamma}_0(t_0) = \sigma\,\Gamma_0(t_0) \tag{29}$$

obtaining in this way the NMO-stretching compensated instantaneous frequency $\bar{\Gamma}_0(t_0)$.

In equations (26) to (29) we dropped the superscript indicating the order of the complex attributes to simplify the notation, but the result expressed by (29) holds for any order of instantaneous frequency $\Gamma_0^{(j)}(t_0)$. Therefore, the seismic trace $\bar{r}_0(t)$ after NMO correction and stretching compensation is given by:

$$\bar{r}_0(t) \approx e_0^{(N)}(t) \prod_{j=1}^{N} \cos[\sigma\,\tau\,\Gamma_0^{(j)}(\tilde{t})] \approx e_0^{(N)}(t) \prod_{j=1}^{N} \cos[\sigma\,\Phi_0^{(j)}(t)] \tag{30}$$

which is obtained from (15) simply by scaling the generalized instantaneous phases $\Phi^{(j)}(t)$ or frequencies $\Gamma^{(j)}(t)$ by the σ factor, according to Eqs. (13) and (29). We may call this scaling N-th order phase gain, since it generalizes a similar procedure introduced by SGUAZZERO and VESNAVER [1987] to enhance the sharpness of velocity spectra.

Spectral interpretation

We saw previously that NMO stretching produces a remapping of the trace spectrum towards lower frequencies. This effect is sketched in *Fig. 7*, together with that of its compensation by phase gain. We see that a boxcar spectrum of a

wavelet at offset x (part A) is scaled, shifted and compressed by NMO correction to offset 0 (part B). A first order phase gain compensation for NMO stretching (part C) shifts the spectrum back to its initial position, but does not restore the initial bandwidth (see Appendix B).

Better results are obtained if a higher order phase gain is used. In fact, we may separate the factors of $\bar{r}_0(t)$ in Eq. (30) into two classes. In the first one, there are the N cosinusoidal waves $\cos[\sigma\Phi_0^{(j)}(t)]$. Since their spectra are spikes instead of bands, they are accurately compensated for NMO stretching by phase gain. On the other hand, envelope $e_0^{(N)}(t)$ may be regarded as an uncompensated component. Nevertheless, if order N is not too small, $e_0^{(N)}(t)$ is a smooth curve which is not very sensitive to stretching residuals.

Figure 8 displays the effect of phase gain of increasing order on the wavelets of Fig. 2, using a constant gain factor $\sigma = 1.4$. The increasing accuracy obtained in waveform preservation is evident especially in the first three orders. If N is greater than 3 only marginal improvements are obtained.

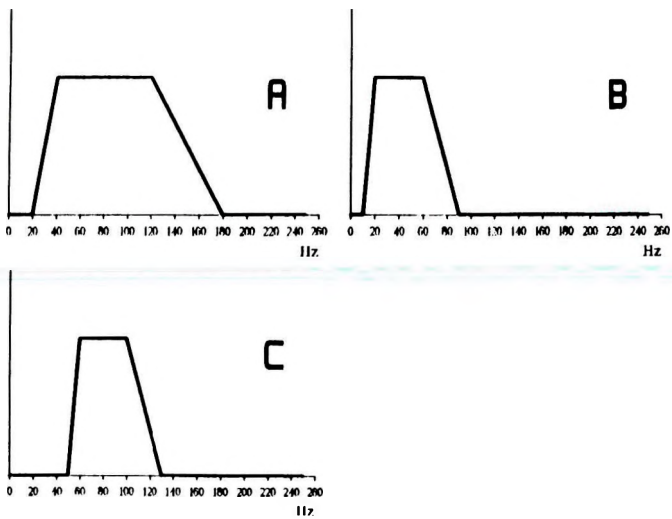

Fig. 7. Band-limited flat spectrum of a wavelet at offset x (part A) undergoes NMO correction to offset 0 (part B). A first order phase gain compensation for NMO stretching (part C) restores the initial position of the spectrum, but not its original bandwidth

7. ábra. x észlelési távolságú elemi jel sávkorlátozott spektruma (A), a dinamikus korrekció okozta spektrumváltozás (B) és ez elsőfokú fáziserősítés-kompenzáció után (C). A nyújtóhatás kompenzálása helyreállítja a spektrum eredeti helyzetét, de sávszélességét nem

Рис. 7. Ограниченный по частоте спектр элементарного сигнала при расстоянии x между источником и приемником (A), изменение спектра, вызванное динамиеской поправкой (B), и то же после компенсирования усиления фаз первой ступени (C). Компенсированнем эффекта удлинения восстанавливается исходное положение спектра, но не восстанавливается ширина полос

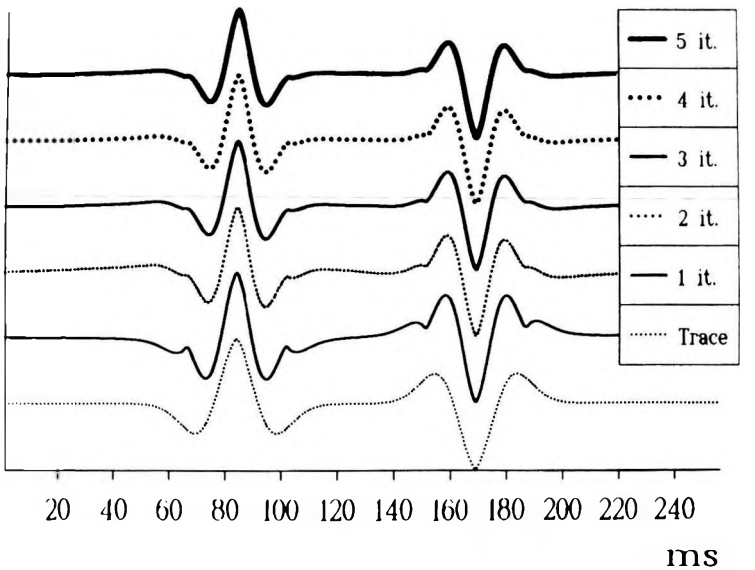

Fig. 8. Effect of phase gain of increasing order to compress the wavelets in Fig. 2. The σ value is 1.4

8. ábra. A 2. ábra szintetikus szeizmogramja elemi jeleinek összenyomása növekvő fokú fáziserősítéssel (σ=1,4)

Рис. 8. Сжатие элементарных сигналов синтетической сейсмограммы рис. 2 при нарастающем усилении фаз (σ = 1,4)

5. Application to synthetic and real data

The synthetic CMP gather in Fig. 1 was generated by convolving a zero-phase wavelet with a reflectivity series simulating primary reflections from horizontal layers, and therefore obeying the hyperbolic Move Out law (Eq. (16)). The sampling rate is 2 ms, the offset range from 0 to 2350 m, the spacing of traces is 50 m.

Figure 9 displays the effect of NMO stretching compensation on the data in Fig. 1 using two different orders for the phase gain, i. e. 1 (part B) and 3 (part C). Obviously, the overstretched wavelets were recompressed only within certain limits, so that the need for a mute is not eliminated, but simply reduced. Later some incoherent band-limited noise is added and mute scans are carried out on a group of CMP gathers of the same model.

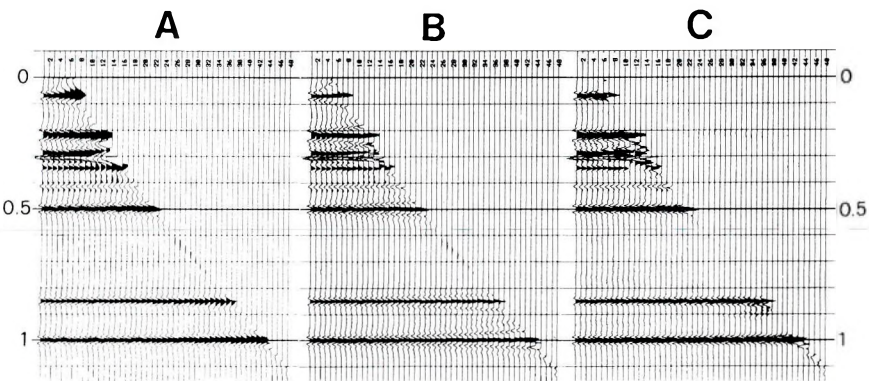

Fig. 9. NMO stretching compensation of the muted data in Fig. 1 using A) input data; B) using phase gain, N=1; C) using phase gain, N=3

9. ábra. A dinamikus korrekció nyújtó hatásának kompenzálása az 1. ábra vágás utáni adatain
A) bemenő adatok; B) fáziserősítés, N=1;
C) fáziserősítés, N=3

Рис. 9. Компенсирование эффекта удлинения от динамической поправки на данных рис. 1 после срезания
A) Входные данные; B) Усиление фаз, $N = 1$; C) Усиление фаз, $N = 3$

In *Figures 10* and *11* we can compare the results obtained by standard NMO correction with those obtained using phase gain compensation. An increasing abscissa corresponds to an increasing number of near offset traces added to the stack. We notice that NMO stretching compensation not only allows the choice of a much wider mute at any given arrival time, but also improves the high frequency content of the stacked signals. A by-product of these effects is that incoherent noise is damped much more since a wider mute is used, so that an additional improvement of the signal to noise ratio is achieved.

Figures 12 and *13* display mute scans of marine data, acquired by OGS in the Mediterranean Sea. The sampling rate is 4 ms, the maximum fold is 12 and the offset range is between 220 and 2620 m. We notice that by compensating for NMO stretching (Fig. 13) a sharp water bottom reflection is obtained for any fold, whilst without this compensation other high frequency signals appear distorted in Fig. 12.

Figures 14 and *15* show the effectiveness of stretching compensation on a stacked seismic section from the same dataset as Figs 12 and 13. Once more, we see that the compensated stack (Fig. 15) improves the resolution of the uppermost reflections, whilst in the lower part, where the stretching effects are negligible, the two sections are almost identical.

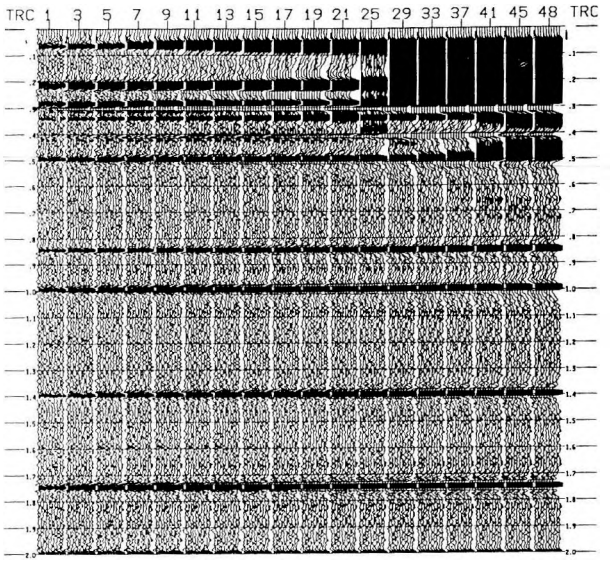

Fig. 10. Mute scan on synthetic data using standard processing

10. ábra. Vágás vizsgálat szintetikus adatokon, hagyományos feldolgozás mellett

Рис. 10. Исследование срезания на синтетических данных при традиционной обработка

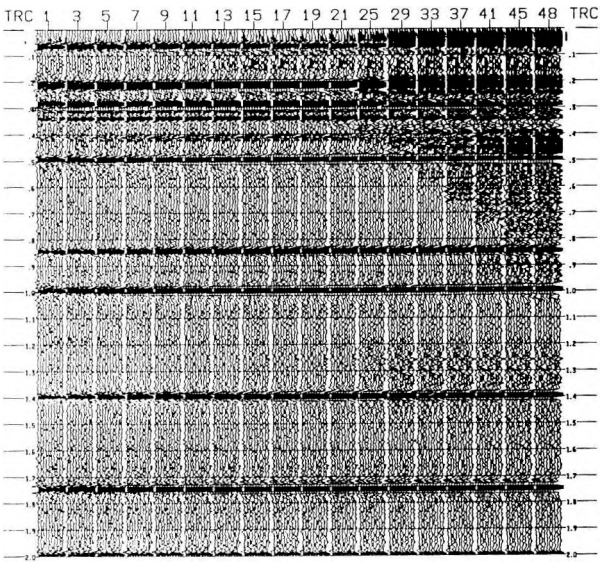

Fig. 11. Mute scan on the same data as in Fig. 10 using NMO stretching compensation

11. ábra. Vágás vizsgálat a 10. ábra adatain, a dinamikus korrekció nyújtó hatásának kompenzálásával

Рис. 11. Исследование срезания на данных рис. 10 при компенсировании эффекта удлинения от динамической поправки

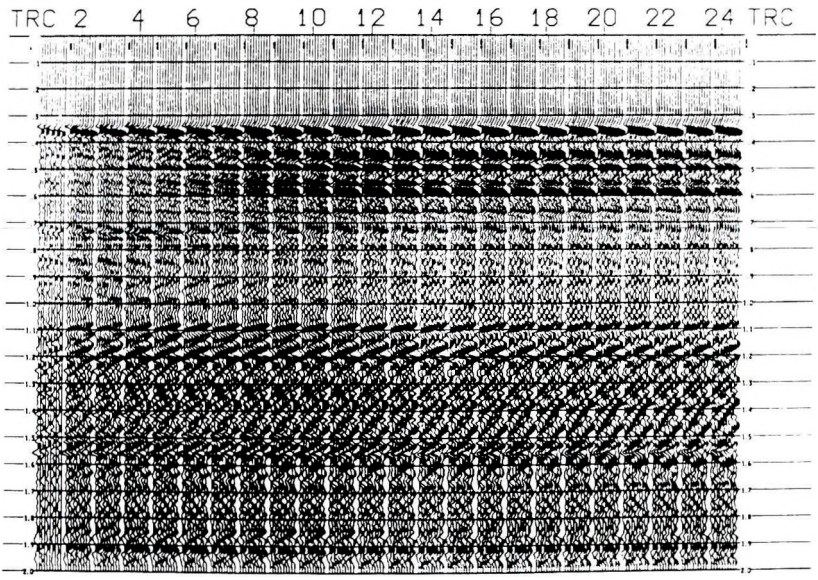

Fig. 12. Mute scan on real marine data using standard processing
12. ábra. Vágás vizsgálat tengeri adatokon, hagyományos feldolgozás mellett
Рис. 12. Исследование срезания на морских при традиционной обработке

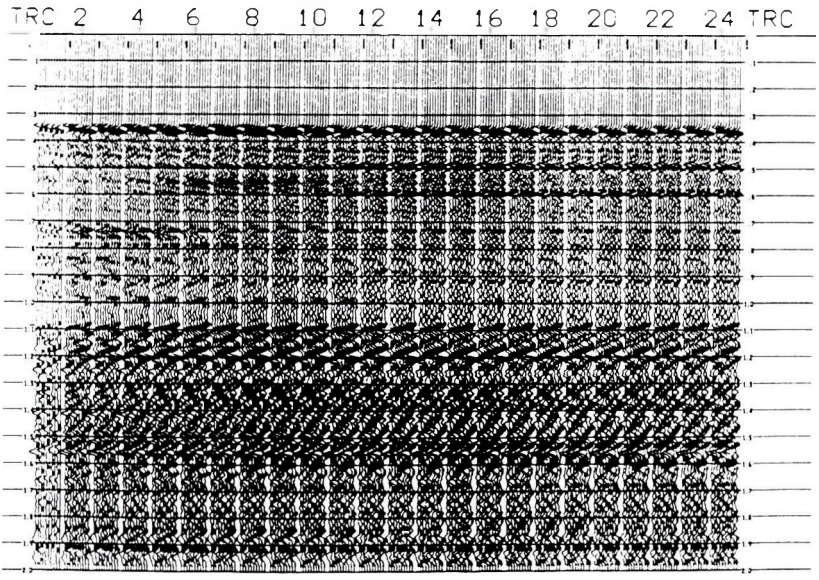

Fig. 13. Mute scan on the same data as in Fig. 12 using NMO stretching compensation
13. ábra. Vágás vizsgálat a 12. ábra adatain, a dinamikus korrekció nyújtó hatásának kompenzálásával
Рис. 13. Исследование срезания на данных рис. 12 при компенсировании эффекта удлинения от динамической поправки

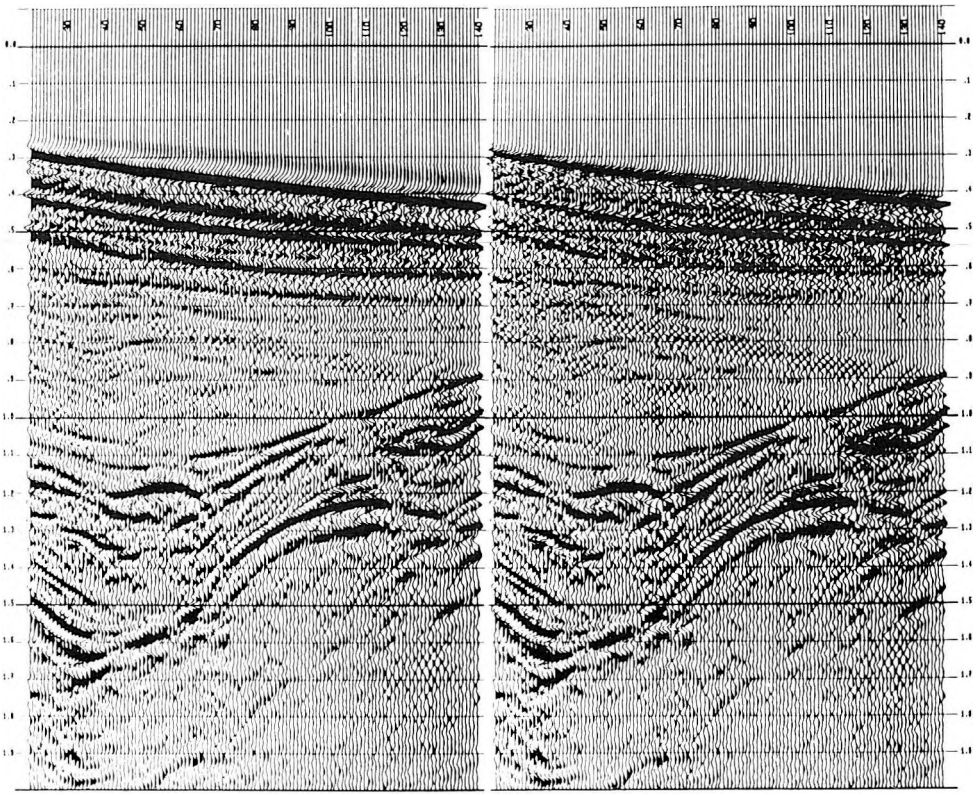

Fig. 14. Stacked seismic section obtained by standard processing

14. ábra. Hagyományos feldolgozással készült összegszelvény

Рис. 14. Суммированный разрез, полученный при традиционной обработке

Fig. 15. The same stacked section as in Fig. 14 using NMO stretching compensation

15. ábra. A 14. ábra szelvénye a dinamikus korrekció nyújtó hatásának kompenzálásával

Рис. 15. Разрез рис. 14 при компенсировании эффекта удлинения от динамической поправки

6. Conclusions

An algorithm able to reduce NMO stretching artifacts has been introduced, it is based on trace factorization using generalized complex attributes. Improvements are obtained for near-surface reflections, in particular for offsets which are large with respect to reflector depths. For this reason, the procedure is useful if the exploration target is the uppermost layers, i. e. for high resolution surveys.

From the computational point of view, NMO stretching compensation is neither cheap nor expensive. The operation number required for each order of phase gain is slightly higher than for linear filtering; since second or third order algorithms are satisfactory, it follows that the global cost is about three times that of pre-stack linear filtering. However, it should be emphasized that vector or parallel computer architecture may significantly reduce the computational impact. In fact, all operations required are typically of vector type and, since the traces are considered independently, they may be shared amongst different processors.

Acknowledgements

The authors wish to thank F. Rocca for hints and fruitful discussions, and P. Guidotti for manuscript revision.

This paper is publication No. 304 of OGS.

Appendix A

In their classic paper, TANER et al. [1979] define apparent polarity as the sign of the seismic trace $r(t)$ when its envelope $e^{(1)}(t)$ has local maxima. Since we need to associate apparent polarity with a whole wavelet instead of with a few points, we extend the definition by the following algorithm:

— compute envelope $e^{(1)}(t)$;

— delimit the lobes of envelope $e^{(1)}(t)$ as the parts comprised between two consecutive relative minima;

— assign to all samples within a lobe the sign of trace $r(t)$ at the maximum of the envelope in that lobe.

To remove the apparent polarity we have to multiply $r(t)$ by the step-wise sequence so obtained. To restore the initial polarity, the data are multiplied once more by the apparent polarity function of $r(t)$.

Appendix B

Let us consider a zero-phase wavelet $w(t)$ whose spectrum $W(f)$ is the following boxcar function:

$$W(f) = 1, \text{ for: } |f_c - Df| \le |f| \le |f_c + Df|$$
$$= 0, \text{ elsewhere} \qquad (B-1)$$

where f_c is the central frequency and Df is the half-width of the frequency band (Fig. 7). Wavelet $w(t)$ is given by:

$$w(t) = [\sin(f_c + Df)t - \sin(f_c - Df)t] / [\pi t] \qquad \text{(B-2)}$$

whilst its complex counterpart $c^{(1)}(t)$ is:

$$c^{(1)}(t) = \exp(i f_c t) \sin(Df\, t) / [\pi t] \qquad \text{(B-3)}$$

In this case, the central frequency f_c coincides with the instantaneous frequency. Applying a first order phase gain implies a multiplication of f_c by the stretching factor σ, but this is nothing other than a translation of the frequency band because its half-width Df remains unchanged (Fig. 7).

REFERENCES

ACKROYD M. H. 1970: Instantaneous spectra and instantaneous frequency. Proceedings IEEE **58**, 141 p.

DUNKIN J. W. and LEVIN F. K. 1973: Effect of Normal Move Out on a seismic pulse. Geophysics **38**, 4, pp. 635–642

GAZDAG J. and SGUAZZERO P. 1984: Interval velocity analysis by wave extrapolation. Geophysical Prospecting **32**, 3, pp. 454–479

SGUAZZERO P. and VESNAVER A. 1987: A comparative analysis of algorithms for stacking velocity estimation. In: Deconvolution and Inversion, Bernabini et al. (eds), Blackwell, pp. 267–286

TANER M. T., KOEHLER F. and SHERIFF R. E. 1979: Complex seismic trace analysis. Geophysics **44**, 6, pp. 1041–1063

ÁLTALÁNOSÍTOTT KOMPLEX ATTRIBUTUMOK ÉS ALKALMAZÁSUK A DINAMIKUS KORREKCIÓ NYÚJTÓ HATÁSÁNAK KOMPENZÁLÁSÁRA

A. VESNAVER és F. POLETTO

Az NMO-korrekció a tér–idő tartományban lényegében a szeizmikus csatornák időben változó nyújtása. A művelet alapvető korlátja a korai, nagy észlelési távolságú reflexiók erős deformálódása. Ezért ezeket stacking előtt kivágják. Noha maga a stack egyéb tartományokban (pl. f–k tartományban) torzítás nélkül elvégezhető, egyéb feldolgozási lépésekhez, mint pl. a maradék statikus korrekcióhoz NMO-korrigált csatornák szükségesek. A dolgozatban egy olyan algoritmust mutatnak be, amely képes kompenzálni az NMO-korrekció nyújtó hatását. Általánosított komplex attributumokat vezetnek be, amelyek rávilágítanak az NMO-korrekció spektrális tulajdonságaira. Végül szintetikus és valódi adatokon szemléltetik az eljárás alkalmazhatóságát.

ОБОБЩЕННЫЕ КОМПЛЕКСНЫЕ ХАРАКТЕРИСТИКИ И ИХ ПРИМЕНЕНИЕ В КОМПЕНСИРОВАНИИ ЭФФЕКТА УДЛИНЕНИЯ ОТ ДИНАМИЧЕСКОЙ ПОПРАВКИ

А. ВЕСНАВЕР и Ф. ПОЛЕТТО

Динамическая поправка в пространственно-временной области по существу означает переменное во времени удлинение сейсмических трасс. Фундаментальным ограничением метода является сильная деформация ранних отражений при больших растояниях между источником и приемником. Поэтому эти отражения удаляются перед суммированием. Хотя само суммирование в других областях, например, в области f–k, может быть выполнено без искажений, для других ступеней обработки, как например, для остаточной статической поправки, необходимы трассы с динамической поправкой. В работе представляется алгоритм, благодаря которому становится возможным компенсирование удлиняющего эффекта от динамической поправки. Вводятся обобщающие комплексные характеристики, относящиеся к спектральным особенностям динамической поправки. Наконец, на синтетических и реальных данных иллюстрируется применение способа.

GEOPHYSICAL TRANSACTIONS 1990
Vol. 35. No. 4. pp. 273–285

RAY-TRACING MODELLING IN SEISMIC EXPLORATION

Zoltán WÉBER*

Seismic modelling provides an inexpensive means of evaluating the potential effectiveness of a proposed data acquisition procedure. Using an approximate geological model based on information from previous work in the area, proposed source, receiver and recording parameters can be included in a seismic simulation to assess the preliminary design of a seismic survey. Seismic modelling can also be used to generate appropriate synthetic data sets for testing processing algorithms. The purpose of this paper is to present a general ray-tracing modelling package which has been written to compute finite-offset and walkaway VSP data as well as conventional seismic time sections; CRP gathers, seismograms, etc. in laterally varying two-dimensional (2-D) media. It requires sufficient speed and a means of providing a proper balance between speed and accuracy. To speed up computations, third-order parabolas are fitted to consecutive straight line segments of each interface in the vicinity of all breakpoints. Thus, in the calculation of intersections of raypaths and interfaces, linear equations have to be solved in most cases, whereas third-order equations are solved only when rays arrive in the neighbourhood of breakpoints. As a net result ray tracing becomes fast and accurate even with a personal computer. The examples that are given prove that even a relatively simple modelling method can provide valuable information for exploration geophysicists.

Keywords: ray tracing, seismic modelling, VSP, time sections, synthetic seismograms, CRP gather

1. Introduction

The typical geometry for a vertical seismic profile (VSP) consists of a single source on the earth's surface and a number of recorder positions in a vertical drill hole (offset VSP) or a single geophone in the well and several sources on the surface (walkaway VSP). Vertical seismic profiles have been the subject of many recent publications. Examples of numerical modelling of VSP data were presented in WYATT [1981] and THYBO [1985] who synthesized acoustic responses from sonic and density logs, and in URSIN and ARNTSEN [1985] who computed the acoustic response accounting for geometrical spreading and absorption. Synthetic VSPs have been used in iterative forward modelling [LEE and BALCH 1983], in iterative inversion for velocity and attenuation [DIETRICH and BOUCHON 1985; GRIVELET 1985] and in interpretation of CRP data [HARDAGE 1983, BALCH and LEE 1984].

One feature common of all the above-mentioned studies is that they deal with zero-offset VSP data in a one-dimensional context. This is the result of three factors: first, there is typically only one source position; second, the offset of the source is usually small; and third, the earth's structure is assumed to be a stack of horizontal layers. None of these restrictions is necessary. If the offset is not zero, the lateral variations of the geological structure should be taken into

*Geophysical Department, Eötvös L. University, H–1083 Budapest, Kun Béla tér 2.
Manuscript received (revised version): 20 November, 1989

account. Similarly, in the computation of synthetic seismograms and conventional seismic time sections two- or three-dimensional modelling should be used. The purpose of this paper is to present a program package which has been written to model finite-offset and walkaway VSP data as well as conventional seismic time sections and seismograms in laterally varying two-dimensional models. In this topic the reader is referred to YOUNG et al. [1984], MCMECHAN [1985], SUPRAJITNO and GREENHALGH [1986] and others. Such modelling can be used directly as an interpretational tool and as a source of data for testing of inverse (imaging) processes.

2. Modelling by geometrical ray tracing

The geometrical ray-tracing method is chosen here to compute synthetic VSPs and surface seismic data. There are numerous modelling techniques commonly employed for the computer simulation of seismic wave propagation. The capabilities of these techniques vary according to the theoretical foundations and subsequent approximations upon which the algorithms are based. Ray-tracing modelling assumes that seismic energy propagates along straight line segments (rays), and that reflection and transmission processes occur at a mathemathical point when one of these rays intersects a boundary between two different rock units. Actually, seismic energy propagates through the earth as spherically spreading wavefronts, and reflection and transmission processes occur not at mathematical points but in large elliptical Fresnel zones. Each reflection point shown in the ray-tracing models in this paper marks only the centre of the Fresnel zone corresponding to a reflected raypath. The physical dimensions of these Fresnel zones must be kept in mind when interpreting ray trace models since a Fresnel zone defines the size of the reflector area which contributes to each reflection raypath. Particular attention should be given to situations where a Fresnel zone may be larger than the lateral dimensions of a structural or stratigraphic feature of a model. In such cases, if a raypath can exist mathematically, it generally yields the proper travel time, but the amplitude of the synthetic reflection will be incorrect since in the real earth the Fresnel zone would extend beyond one or more edges of the feature.

Diffracted energy can be defined as energy which propagates along raypaths other than those given by Snell's law of reflection and refraction. In real earth seismology, diffracted energy can, in some instances, be the dominant type of response recorded by geophones. However, since all energy propagation in ray-tracing modelling obeys Snell's law, the calculated results shown in this paper disregard diffracted energy. Diffraction effects can be ignored in modelling as long as the wavelengths contained in the seismic pulse are much shorter than the radius of curvature of any part of a reflecting surface occurring in the model. Thus, ray-tracing modelling in the vicinity of sharp curvature changes in an impedance boundary should be viewed with caution.

Apart from these disadvantages the ray-tracing technique has several advantages. Relatively simple, efficient ray-tracing algorithms can be developed

for two- or three-dimensional media including structurally complex geological models. Sub-programs can be attached which compute partial amplitude information, geometrical spreading and absorption. User-defined types of multiple reflections can also be calculated easily. This method allows for flexible definition of source–receiver geometry and thereby facilitates modelling of any data acquisition configuration.

These features allowed us to prepare an efficient ray tracing program package on an IBM PC/AT personal computer, i. e. ray tracing could be realized without extremely fast computers. This tool of seismic modelling has proved to be valuable for determining the optimum VSP field geometry that can address a given structural or stratigraphic problem. Constructing ray-tracing models before starting a VSP experiment will result in fewer instances where VSP sources and geophones are positioned so that they record data which are incapable of achieving a given exploration objective. The modelling package also provides a framework for an economic analysis during the planning stage of a field experiment. For example, modelling can prevent the recording of more data than are needed to achieve an exploration objective. It can also indicate the amount of data that needs to be recorded in order to properly image a subsurface anomaly, and thus it allows an explorationist to make a reliable estimate of how much time and money will be required to record the data. And last but not least, it can demonstrate the structural and stratigraphic messages contained in VSP, CRP, or conventional seismic time sections.

3. Utilities of the program package

The geological model can be defined interactively on the computer screen. The layer boundaries consist of straight line segments, but in the subsequent calculations third-order parabolas are fitted to adjacent segments in the vicinity of each breakpoint. Each layer has constant P-wave velocity, bulk density and quality factor Q.

The user is able to get a preview with some possible raypaths for the given VSP geometry. Several ray types can be selected by the user, such as direct waves only, primary reflections, primary reflections from specified interfaces(s), all the second-order surface multiples and user-defined multiple reflections. The purpose of this calculation is to create a picture for a quick-look type interpretation. Because we do not prescribe for the raypaths to terminate at the exact receiver positions, it is not time-consuming to create previews. It is advisable to run a preview before subsequent detailed calculations in order to work out experimentally the suitable source–receiver configurations.

If a synthetic time section is to be calculated, those raypaths should be determined that start from the source(s) and terminate at the geophone(s). This calculation needs an iterative technique. It is time-consuming: if we use a complex geological model and the number of traces is a few hundred, the computation takes more than one hour. However, after such a computation the user is able to make a lot of different plots, such as the determined raypaths, the

reflecting points of the primary refletions and the synthetic time section. In the last of these several options can be chosen. The computed quantity may be pressure, displacement, particle velocity or acceleration. In the last three cases both the vertical as well as the horizontal components can be determined. The impulse response can be convolved by four types of wavelets. Peak frequencies and lengths are defined by the user.

Absorption and/or geometrical spreading can also be included. The magnification of a given window of the time section is possible.

4. The algorithm

In the previous section it was mentioned that if one wishes to calculate synthetic time sections then those raypaths should be calculated that terminate at the exact receiver positions. This calculation needs iterations and, as a consequence, it is necessary to compute several times more raypaths than those appearing in the final results. It means that the efficiency of computation of a single raypath influences the running time of the whole ray-tracing program. Because the ray-tracing algorithm is given and cannot be modified, the computation time depends on how the layer boundaries are handled by the program.

The model-definition program actually accepts and stores the coordinates of some points of each consecutive interface. The simplest method of working with a layer boundary is to connect its points by straight line segments. In order to determine points of intersections of raypaths and the interface only linear equations have to be solved; this is fairly simple and can rapidly be done even with a personal computer. Unfortunately, even a small but abrupt change of an interface always causes an undesirable shadow zone in the reflection event *(Fig. 1a)*. In order to prevent the appearance of fictitious shadow zones the points of the interfaces can be connected by cubic spline functions. In this case, however, third-order equations have to be solved in order to compute the points of intersection of raypaths and the interface, and the determination of the angles of incidence requires the evaluation of second-order polynomials. For realistic geological models this calculation needs so much time on an IBM PC/AT personal computer that its implementation is not economical.

In our program package the following method is used. The defined points of an interface are connected by straight line segments, but in the calculations third-order parabolas are fitted to adjacent segments in the vicinity of each breakpoint. By this method the undesirable shadow zones are eliminated *(Fig. 1b)* and, in the calculation of the points of intersection, third-order equations need to be solved only in a few cases. This allows economical implementation of ray-tracing modelling on a personal computer such as the IBM PC/AT. Furthermore, it is not necessary to fit a parabola at every breakpoint so the geological model may include steep faults without any round-off. Spline interpolation does not possess this advantageous feature.

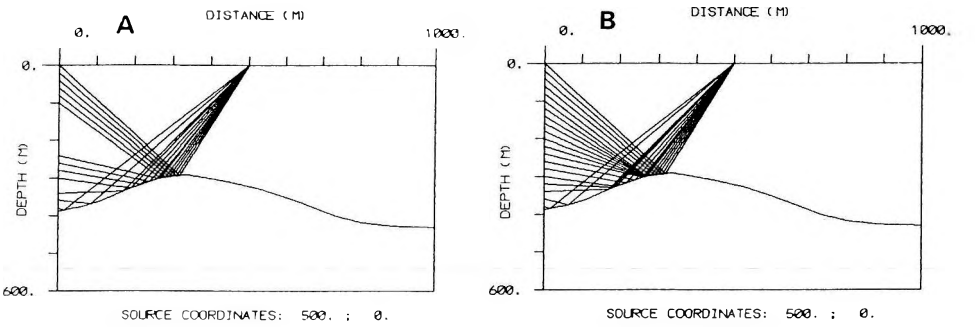

Fig. 1. If the layer boundary consists of straight line segments, two undesirable shadow zones occur (A). If third-order parabolas are fitted to adjacent line segments at the breakpoints, shadow zones disappear (B). The source-receiver geometries are the same in both parts of the figure

1. ábra. Ha a réteghatár egyenes szakaszokból áll, két nemkívánatos árnyékzóna jelenik meg (A). Ha azonban a töréspontokban harmadfokú parabolát illesztünk a szomszédos szakaszokhoz, az árnyékzónák megszűnnek (B). A mérési elrendezés mindkét ábránál azonos

Рис. 1. В случае границы раздела, состоящей из отрезков прямых, появляются две нежелательные теневые зоны (А). Однако если в точках сопряжения к смежным отрезкам подбирается многочлен третьей степени, теневые зоны исчезают (В). Схема измерения одинакова в обоих случаях.

5. Examples

This section presents a series of synthetic VSPs and surface seismic data. All models vary laterally (2-D) and, it is to be hoped, are characteristic in seismic exploration.

A low-velocity wedge is shown in *Fig. 2/a*. The calculated raypaths and the synthetic offset VSP for this model are shown in *Fig. 2/b* and *2/c*, respectively. (Here and in all the following examples, wiggle trace plots will show every geophone response, but raypath plots will show only every fourth raypath.) They contain the direct waves and the primary reflections only. Absorption and geometrical spreading are not included. The Ricker wavelet has a peak frequency of 30 Hz.

The four primary reflections originating from the direct wave branch can clearly be seen (Fig. 2/c). Reflections from the second and third interfaces (from the interfaces of the wedge) create two highly convergent branches. The slope of a reflection depends on the dip of the reflecting boundary. If the dip difference between two interfaces is considerable, the slope difference between the two upgoing reflection events on the VSP section is evident. Thus, the above-mentioned convergence implies a large dip difference.

The low-velocity wedge acts as a collector lens and can thus cause a shadow zone. This shadow zone can be found on the deepest reflection event between the 33rd and the 37th traces.

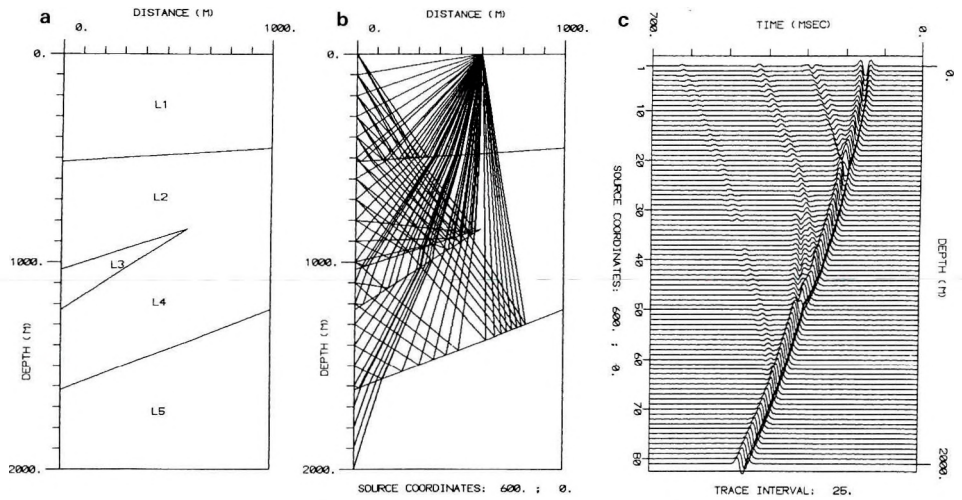

Fig. 2. Modelling for offset VSP geometry
a) Low-velocity wedge model. The layer parameters are shown in Table I
b) Calculated raypaths. The well is at the left-hand-side of the model, the source offset is 600 m. The distance between the equally spaced geophones is 25 m
c) The synthetic VSP section simulating pressure sensitive geophones with Ricker wavelets of 30 Hz peak frequency. Only direct waves and primary reflections are presented

2. ábra. Távoli (offset) VSP modellezése
a) Kissebességű kiékelődés. A rétegparamétereket az I. táblázat tartalmazza.
b) Számított sugárutak. A fúrólyuk a modell bal szélén helyezkedik el, a robbantópont–mélyfúrás távolság 600 m. Az egyenközűen elhelyezett geofonok közötti távolság 25 m.
c) A 2/b ábrán látható mérési elrendezésnek megfelelő szintetikus VSP szelvény, nyomásmérő geofonok és 30 Hz-es Ricker wavelet feltételezésével. Csak a direkt hullámokat és az elsődleges reflexiókat tartalmazza

Рис. 2. Моделирование удаленного (оффсетого) ВСП
а) Выклинивание с малой скоростью. Параметры пластов приведены в таблице I.
b) Расчитанные пути лучей при смещенной геометрии ВСП. Скважина находится на левом краю модели, величина смещения – 600 м. Расстояние между равномерно расположенными сейсмоприемниками равно 25 м.
c) Синтетический разрез ВСП, соответствующий схеме измерения, приведенной на рис. 2b. Содержит только прямые волны и действительные отражения. Предполагались чуствительные к давлению сейсмоприемники. Верхний предел частоты волны Рикера – 30 гц.

It is important to estimate the importance of multiples. It is evident from the plots of *Fig. 3*, where again absorption and geometrical spreading are not included, that a surface multiple may possess larger energy than a primary reflection. This suggests that the suppression or at least the identification of these multiples is very important in the interpretation of offset VSPs. The synthetic VSP sections are rather confused near the surface and at short travel times: the reflections from the upper two interfaces can hardly be separated from other

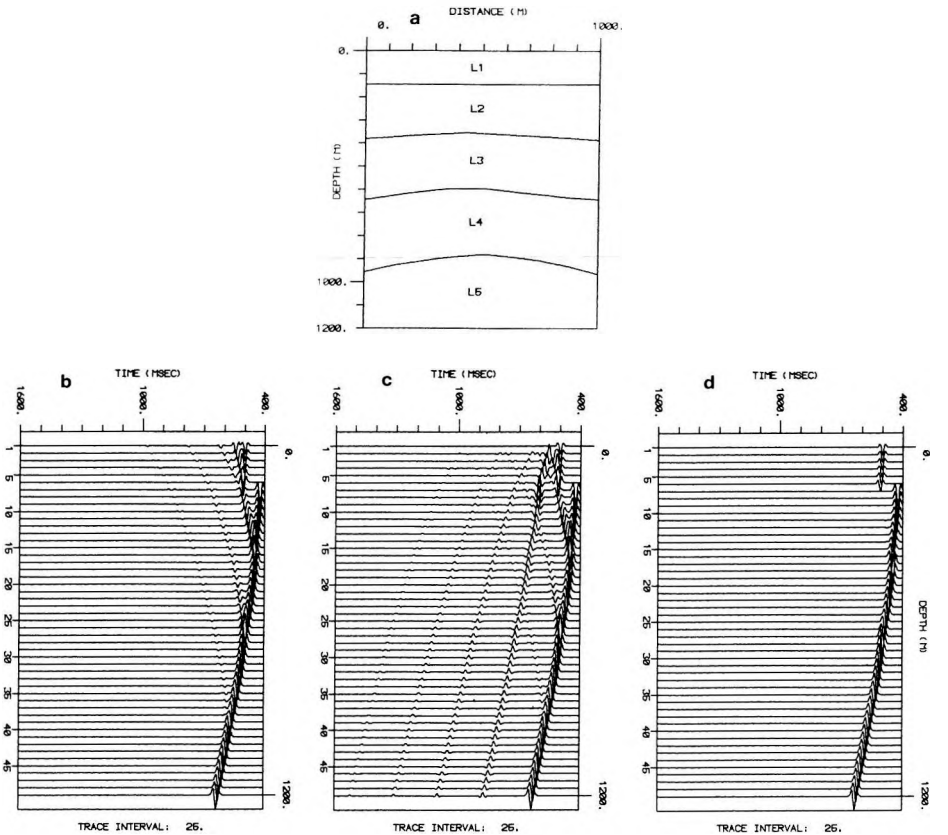

Fig. 3. Modelling with multiples
a) Geological model. The layer parameters are shown in Table II
b) Synthetic VSP section, conditions the same as in Fig. 2/b and 2/c. Only direct waves and primary reflections are shown
c) Synthetic VSP section with all the second-order surface multiples
d) Direct arrivals only

3. ábra. Modellezés többszörösökkel
a) Földtani modell. A rétegparamétereket a II. táblázat tartalmazza.
b) Szintetikus VSP szelvény, a 2/b ábrán bemutatott feltételekkel. Direkthullámok és elsődleges reflexiók
c) Szintetikus VSP szelvény az összes másodrendű felszíni többszörössel
d) Direkthullámok

Рис. 3. Моделирование с кратными волнами
a) Простая геологическая модель с почти горизонтальными слоями. Параметры пластов приведены в табли.. ' II.
b) Синтетический разрез ВСП, соответствующий геологической модели, представленной на рис. 2b. Прямые волны и действительные отражения.
c) Синтетический разрез ВСП со всеми поверхностными кратными второго порядка.
d) Прямые волны.

Layer No.	Velocity (m/s)	Density (g/cm^3)
1	4000	2.80
2	5000	3.00
3	4000	2.80
4	5000	3.00
5	4500	2.90

Table I. Layer parameters of the geological model of Fig. 2/a

I. táblázat A 2/a ábrán bemutatott földtani modell rétegparaméterei

Таблица I. Параметры пластов геологической модели, представленной на рис. 2/a.

Layer No.	Velocity (m/s)	Density (g/cm^3)
1	1200	2.00
2	1800	2.10
3	2200	2.30
4	2600	2.40
5	2800	2.50

Table II. Layer parameters of the geological model of Fig. 3/a

II. táblázat A 3/a ábrán bemutatott földtani modell rétegparaméterei

Таблица II. Параметры пластов геологической модели, представленной на рис. 3/a.

Fig. 4. Modelling for walkaway VSP geometry
a) Unconformity reservoir. The layer parameters are shown in Table III
b) Synthetic walkaway VSP. The well is in the middle of the model, the geophone is at a depth of 700 m, the source spacing is 20 m, other conditions as in 2/c. Only direct waves and primary reflections are presented
c) Synthetic walkaway VSP for the modified model (L6=L7), geometry unchanged
d) Raypaths related to the synthetic section shown in Fig. 4/b

4. ábra. Távolodó (walkaway) VSP modellezése
a) Diszkordancia-csapda. A rétegparamétereket a III. táblázat tartalmazza.
b) Szintetikus távolodó VSP szelvény, nyomásérzékeny geofonok és 30 Hz-es Ricker wavelet feltételezésével. A fúrólyuk a modell közepén, a geofon 700 m mélyen helyezkedik el, a források közötti távolság 20 m. Csak a direkthullámokat és az elsődleges reflexiókat számítottuk.
c) A módosított modellnek megfelelő szintetikus távolodó VSP szelvény a 4/b ábrán leírt mérési geometria mellett.
d) A 4/b ábrán bemutatott szintetikus szelvényhez tartozó sugárutak

Рис. 4. Моделирование удаляющегося (walkaway) ВСП.
a) Ловушка приуроченная к несогласию. Параметры пластов приведены в таблице III.
b) Синтетический разрез ВСП с движущимся источником. Скважина находится в середине модели, глубина сейсмоприемника – 700 м, расстояние между источниками 20 м. Расчитывались только прямые волны и действительные отражения. Предполагались чуствительные к давлению сейсмоприемники. Верхний предел частоты волны Рикера – 30 гц.
c) Синтетический разрез ВСП с движущимся источником, соответствующий модифицированной модели, при геометрии измерения, представленной на рис. 4b.
d) Лучевые пути соответствующие синтетическому разрезу, представленному на рис. 4b.

events. In order to solve this problem we have calculated a synthetic VSP which contains the direct waves only (Fig. 3/d). Comparing these data with the other figures, the identification of the two reflections under consideration becames easier.

Modelling of an unconformity reservoir is shown in *Fig. 4/a*. Layer 6 contains hydrocarbons and, as a consequence, its P-wave velocity is lower and its bulk density less than those of layer 7. Two synthetic walkaway VSPs have been calculated: one for the original model *Fig. 4/b* and one for a slightly modified version of the model, in which the parameters of the 6th and 7th layers are the same (there is no hydrocarbon, *Fig. 4/c*). Figure 4/d shows the related raypaths. Only the direct waves and the primary reflections have been calculated. Absorption and geometrical spreading are not included and the Ricker wavelet again has a peak frequency of 30 Hz.

Detailed comparison of the two VSPs shows a salient difference. The decrease of the acoustic impedance in the reservoir locally enhances the reflectivities of its faces, giving increased amplitudes of the reflections (see the right-hand-side of the sections between 200 and 300 milliseconds). This

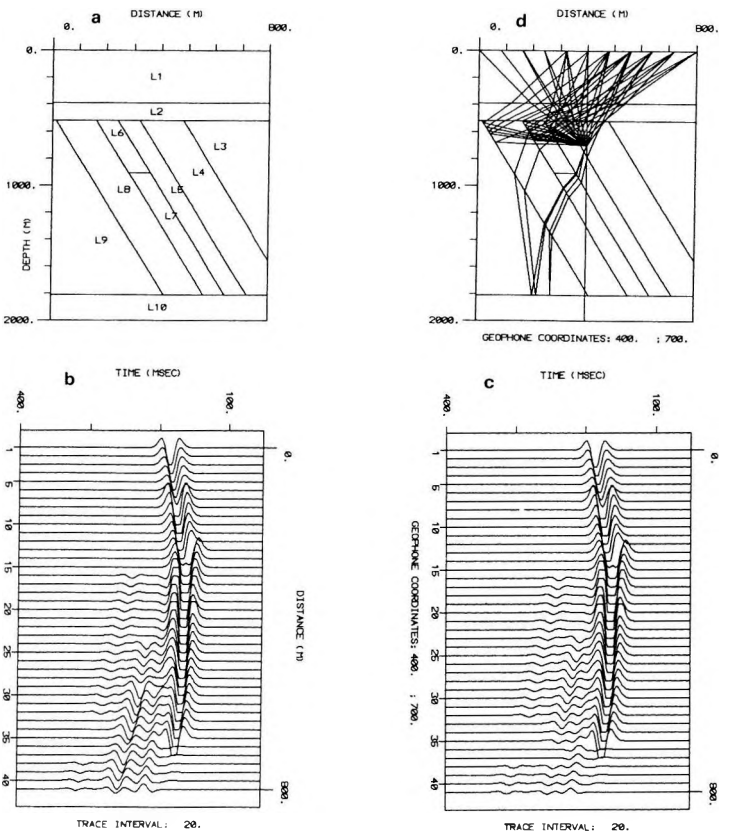

increased energy is similar to the bright spot well known as a potential hydrocarbon indicator.

Layer No.	Velocity (m/s)	Density (g/cm^3)
1	4000	2.80
2	5000	3.00
3	4000	2.80
4	4500	2.90
5	4700	2.95
6	3600	2.70
7	4000	2.80
8	4500	2.90
9	4900	3.00
10	5000	3.00

Table III. Layer parameters of the geological model of Fig. 4/a

III. táblázat A 4/a ábrán bemutatott földtani modell rétegparaméterei

Таблица III. Параметры пластов геологической модели, представленной на рис. 4/a.

A more complicated geological model is shown in *Fig. 5/a*. The related raypaths and the synthetic seismic time section can be seen in Figs. 5/b and 5/c, respectively. Absorption is included and the wavelet (a damped sine wave) has a peak frequency of 30 Hz. It is assumed that the recorded parameter is the *z*-component of the particle velocity. (In the previous examples pressure sensitive geophones were assumed.)

Fig. 5. Modelling a relatively complicated 2-D geological section
a) Geological model. The layer parameters are shown in Table IV.
b) Raypaths
c) Synthetic seismic time section, primaries only

5. ábra. Bonyolult 2-D földtani szelvény modellezése
a) A földtani modell. A rétegparamétereket a IV. táblázat tartalmazza
b) Sugárutak
c) Szintetikus időszelvény. Csak az elsődleges reflexiókat mutatjuk be

Рис. 5. Моделирование сложного двухмерного геологического разреза
a) Геологическая модель. Параметры пластов содержатся в таблице IV.
b) Лучевые пути
c) Синтетический времонной разрез. Представлены только действителные отражения.

Layer No.	Velocity (m/s)	Density (g/cm^3)	Q
1	1600	2.30	300
2	1800	2.50	450
3	2200	2.60	700
4	2900	2.60	800
5	3200	2.80	900
6	4200	3.10	1500
7	4500	3.10	1600
8	4000	2.90	1500
9	4800	3.10	1600
10	5000	3.10	2000
11	5200	3.20	2000

Table IV. Layer parameters of the geological model of Fig. 5/a

IV. táblázat Az 5/a ábrán bemutatott földtani modell rétegparaméterei

Таблица IV. Параметры пластов геологической модели, представленной на рис. 5/a.

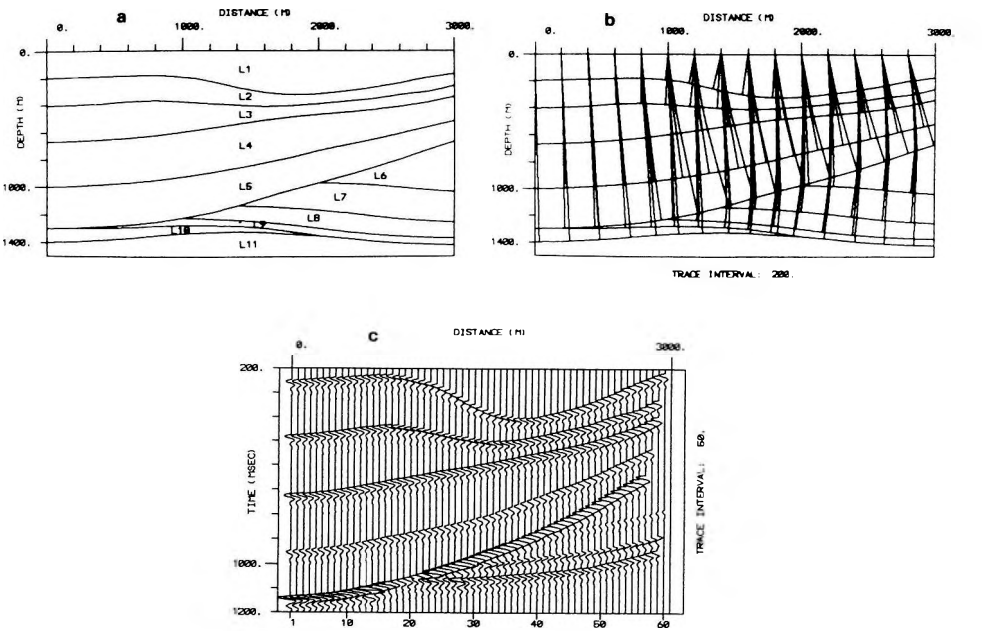

Conclusions

The above discussed examples have proved that the modelling package described here can be used for all those tasks solved by modelling packages for big computers. The package also offers many more possibilities.

In addition to demonstrating the structural and stratigraphic messages contained in the data, ray trace modelling is also invaluable for determining the optimum field geometry. The energy ratio of specified multiples and primary reflections can also be investigated. One can estimate how the recorded data may be influenced by hydrocarbon saturation, if a potential petroleum trap is under consideration. Such modelling can also be used directly as a source of data for testing inverse methods or data processing techniques.

REFERENCES

BALCH A. H. and LEE M. W. 1984: Vertical Seismic Profiling: Technique, Applications, and Case Histories. Reidel Publishing Co.

DIETRICH M. and BOUCHON M. 1985: Measurements of attenuation from vertical seismic profiles by iterative modeling. Geophysics **50**, 6, pp. 931–949

GRIVELET P. A. 1985: Inversion of vertical seismic profiles by iterative modeling. Geophysics **50**, 6, pp. 924–930

HARDAGE B. A. 1983: Vertical Seismic Profiling (Part A). Handbook of Geophysical Exploration Vol 14A, Geophysical Press, London–Amsterdam

LEE M. W. and BALCH A. H. 1983: Computer processing of vertical seismic profile data. Geophysics **48**, 3, pp. 272–287

MCMECHAN G. A. 1985: Synthetic finite-offset vertical seismic profiles for laterally varying media. Geophysics **50**, 4, pp. 627–636

SUPRAJITNO M. and GREENHALGH S. A. 1986: Theoretical vertical seismic profiling seismograms. Geophysics **51**, 6, pp. 1252–1265

THYBO H. 1986: An algorithm for fast time-domain computation of one-dimensional synthetic vertical seismic profiles. Geophysical Prospecting **34**, 6, pp. 833–844

URSIN B. and ARNTSEN B. 1985: Computation of zero-offset vertical seismic profiles including geometrical spreading and absorption. Geophysical Prospecting **33**, 1, pp. 72–96

WYATT K. D. 1981: Synthetic vertical seismic profile. Geophysics **46**, 6, pp. 880–891

YOUNG T. K., MONASH C. B. and TURPENING R. M. 1984: Computer modeling of vertical seismic profiling. Geophysical Prospecting **32**, 5, pp. 851–870

SUGÁRVEZETÉSES SZEIZMIKUS MODELLEZÉS

WÉBER Zoltán

A szeizmikus hullámterjedés számítógépes modellezése a szeizmikus módszer fontos részévé vált sokirányú felhasználhatósága révén. Jelen dolgozat célja egy geometriai sugárkövetésen alapuló modellező programcsomag bemutatása, melynek segítségével mind a VSP különböző változatai, mind pedig stacking szelvények, illetve közös robbantópontokhoz tartozó szeizmogramok számíthatók horizontálisan is változó kétdimenziós modellekre. A megfelelő számítási sebességet úgy érjük el, hogy a számítások során az egyenes szakaszokból álló réteghatárok minden egyes töréspontjánál egy harmadfokú parabolát illesztünk a csatlakozó szakaszokhoz. Ezáltal a sugarak és a réteghatárok metszéspontjának meghatározásakor a legtöbb esetben csak egy lineáris egyenletet kell megoldani, míg harmadfokú egyenletek megoldására csak akkor van szükség, ha a sugarak a töréspont közvetlen közelében érkeznek a réteghatárra. A bemutatott példák bizonyítják, hogy még egy viszonylag egyszerű modellezési eljárás is értékes információkkal szolgálhat a geofizikus számára.

СЕЙМИЧЕСКОЕ МОДЕЛИРОВАНИЕ ПО ГЕОМЕТРИЧЕСКОМУ ПРОСЛЕЖИВАНИЮ ЛУЧА

Золтан ВЕБЕР

Компьютерное моделирование распространения сейсмических волн стало важной частью сейсмического метода благодаря возможности многостороннего использования его результатов.

Целью настоящей работы является представление пакета программ моделирования, основанного на геометрическом прослеживании луча, а помощъю которого можно расчитать ВСП со смещением или движущимся источником, а также суммированные разрезы и сейсмограммы, относящиеся к общей точке взрыва для двумерных моделей с горизонтальными вариациями. Необходимая скорость расчетов достигается так, что в ходе расчетов в каждой отдельной точке сопряжения отрезков прямых, из которых состоят границы пластов, к сопряженному отрезку подбирается трехмерный многочлен. Благодаря этому, при определении точек пересечения границ слоев и лучей в большинстве случаев необходимо решить только одно линейное уравнение, а решать уравнения третьей степени нужно только тогда, если лучи приходят к границе пласта в непосретственной близости от точки сопряжения.

Представленными примерана доказывается, что даже относительно простая процедура моделирования может дать ценную информацию для геофизиков.

GEOPHYSICAL TRANSACTIONS 1990
Vol. 35. No. 4. pp. 287–298

IS THE MAGNETOTELLURIC FIELD IN THE PANNONIAN BASIN DISTORTED BY CARPATHIAN INHOMOGENEITIES?

Antal ÁDÁM*, Tibor STEINER*, Pertti KAIKKONEN**,
Michel MENVIELLE*** and Pascal TARITS***

Deep magnetotelluric soundings indicate conductivity increase in the lower crust and in the asthenosphere of the Pannonian basin at shallower depths than in the surrounding older tectonic units. The question arises how these MT indications are influenced by the resistive rim of the Carpathians and by the Carpathian crustal conductivity anomaly. An attempt is made to answer this by two types of computations: (i) The effect of variation of conductance of the sedimentary complex on the magnetic field were studied using bimodal thin sheet modelling for the Pannonian basin in the cases of resistive and conductive frame (i. e. with different conductances outside the basin), and (ii) the possible effect of the resistive Carpathian blocks and the nearby conductivity anomaly on the deep magnetotelluric sounding curves of the Pannonian basin was studied by 2-D modelling. In both cases the effects were found to be negligible.

Keywords: Pannonian basin, electromagnetic field distortion, Carpathian arc, conductivity anomaly, 2-D modelling, 3-D modelling

1. The problem

The Pannonian (or Carpathian) basin is surrounded by the highly resistive mountain frame of the Carpathians and the Dinarides. Besides these more than 2000 m high crystalline mountain blocks of high resistivity, there is a crustal conductivity anomaly along the whole Carpathian chain, the so-called Carpathian anomaly, between the Inner and Outer Carpathians following mainly the Pieniny Klippen Belt — as has been reported by many joint papers of Czechoslovak and Polish scientists [e. g. JANKOWSKI et al. 1984]. It is questionable whether these geoelectric anomalies do influence the natural electromagnetic field inside the Pannonian basin. If so, the particular resistivity distribution in the crust and the upper mantle, obtained by deep MT soundings, would be an artifact resulting from EM field distortions. Numerical modelling studies were carried out to highlight these effects. The main features of the above-mentioned anomalies are dealt with below.

* Geodetic and Geophysical Research Institute of the Hung. Ac. Sci., Sopron, P.O.B. 5, H–9401 Hungary
** Department of Geophysics, University of Oulu, SF–90570 Oulu 57, Finland
*** Institute de Physique du Globe, 4 Place Jussieu, 75230 Paris Cedex 05, France
Manuscript received (revised version): 16 November, 1989

In *Fig. 1.* the best determined part of the Carpathian anomaly is shown by Wiese arrows in the Western Carpathians [after JANKOWSKI et al. 1984]. The 180° turn of the Wiese arrows, and their zero amplitudes trace the anomaly zone. The 2-D resistivity distribution corresponding to the measured geomagnetic vectors (in the vicinity of Profile P–V) is given in *Fig. 2.* by the same authors. The average depth to the conducting zone along the whole anomaly is 7–12 km based on the 1-D inversion of the magnetotelluric soundings (or 15–25 km based on the line current approximation).

In the Pannonian basin, both conducting zones (that of the lower crust and of the asthenosphere) are much shallower than in the surrounding older platform areas. In these older areas the heat flow is much smaller than at the "hot spot" of the Pannonian basin. In *Fig. 3.* [after ÁDÁM et al. 1989] the average depth to the conducting layer is:

in the lower crust: 18.6 ±5.3 km (n=54 data)

in the asthenosphere: 52.6 ±14 km (n=42 data)

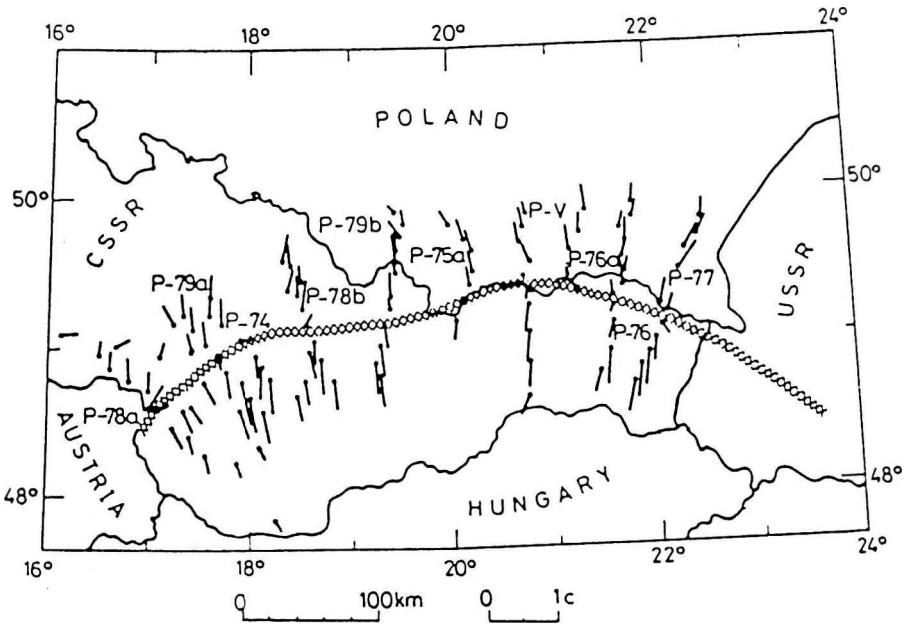

Fig. 1. Induction vectors in the Western Carpathians and the trace of the Carpathian conductance anomaly (hatched line) [after JANKOWSKI et al. 1984]

1. ábra. A Nyugati Kárpátok indukciós vektorai és a Kárpáti vezetőképesség anomália (x–el jelölt sáv) [JANKOWSKI et al. 1984. után]

Рис. 1. Индукционные вектора в Западных Карпатах и аномально высокая проводимость в Карпатах (полоса, обозначенная), по Янковскому у др. 1984 [JANKOWSKI et al. 1984]

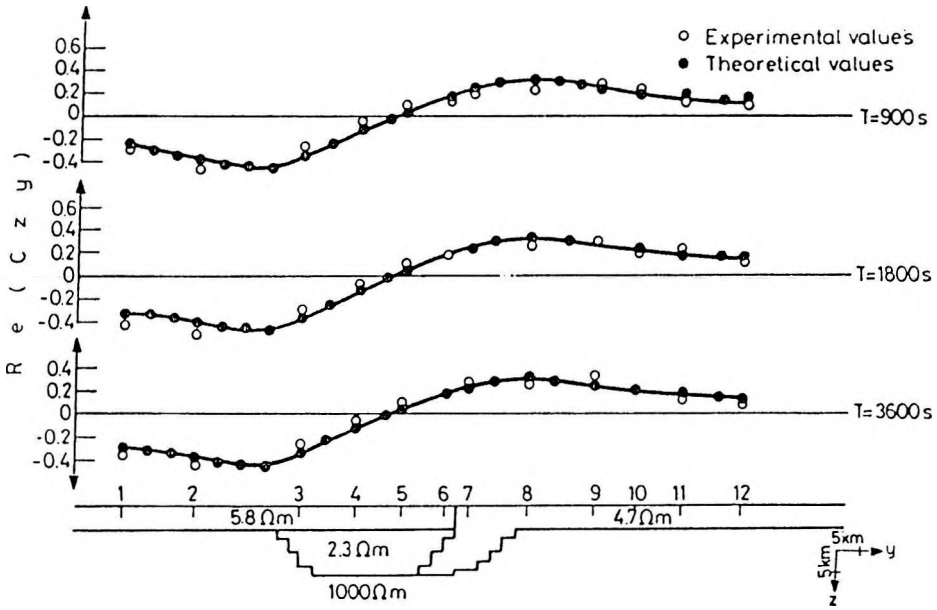

Fig. 2. Schematic 2-D model across the Carpathians in the vicinity of *P–V* profile and the real geomagnetic vectors at three periods [after JANKOWSKI et al. 1984]

2. ábra. A Kárpátokat a *P–V* szelvény közelében harántoló 2-dimenziós vázlatos modell, 3 periódusra számított valós földmágneses vektorokkal [JANKOWSKI et al. 1984. után]

Рис. 2. Схематическая двухмерная модель, пересекающая Карпаты вблизи от профиля *P–V*, с реальными геомагнитными векторами, рассчитанными для трех периодов по Янковскому и др. 1984 [JANKOWSKI et al. 1984]

These data were determined in that part of the basin where the sedimentary cover is horizontaly stratified and so well approximates Tikhonov–Cagniard's 1-D theory. It should be mentioned that the first collection of the scalar MT sounding curves [ÁDÁM 1970] recorded not only in the basin but in the Transdanubian Central Range provide scattered data for the depth to the asthenosphere. That is why ROKITYANSKY and YUDIN [1984] tried to explain — at least partly — the distortion of Ádám's MTS curves [see ÁDÁM 1970] inside the basin by the regional effect of the Carpathian conductivity anomaly.

To find an answer to this distortion problem, two types of computations have been made: (i) Bimodal thin sheet modelling was carried out in the International Laboratory on Numerical Modelling (ILONEM) of Oulu University, Finland for the Pannonian basin using the Vasseur–Weidelt [1977] program both for resistive and conductive frame, and (ii) 2-D modelling to study the effect of the resistive Carpathian blocks and the nearby conductivity anomaly on the deep magnetotelluric sounding curves of the Pannonian basin.

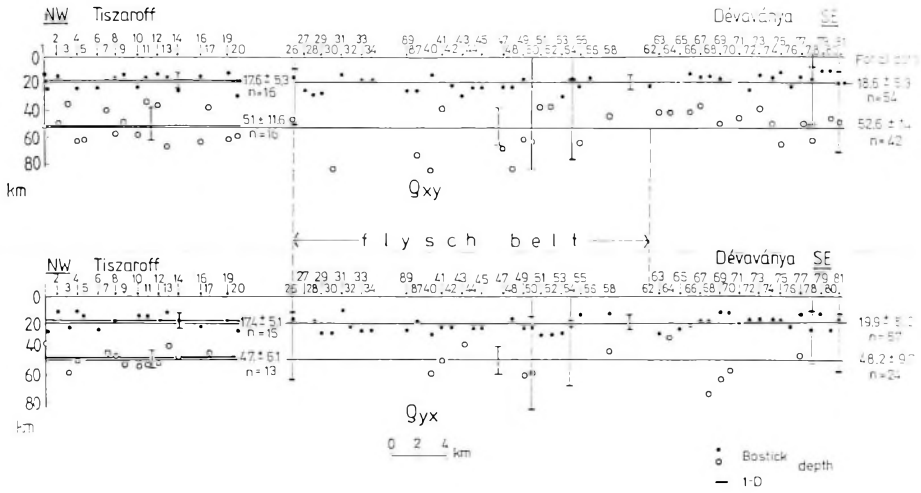

Fig. 3. Depth to the lower crustal conductivity anomaly and to the conducting asthenosphere in the Pannonian basin [after ÁDÁM et al. 1984]

3. ábra. Az alsókéregbeli és az asztenoszférabeli vezetőképesség-anomália mélysége a Pannon-medencében [ÁDÁM et al. 1989. után]

Рис. 3. Глубина до тел аномально высоких проводимостей в нижней коре и в астеносфере по АДАМУ и др. 1989 [ÁDÁM et al. 1989]

2. Thin sheet modelling

The VASSEUR–WEIDELT [1977] thin sheet modelling program adapted by ILONEM was used to study the combined regional effect of a resistive frame (the Carpathians: horizontal conductance $S_1 = h\,[\mathrm{m}] / \rho_{av}\,[\Omega\mathrm{m}] = 2500/200 = 12.5$ Siemens) and a conductive zone (Carpathian anomaly: $S_2 = 2500/10 = 250$ Siemens) and, at the same time, to analyse the more or less local effects due to the variation of the thickness of the sedimentary cover inside the Pannonian basin.

As a first approximation the isopach map of the Neogene–Quarternary sedimentary complex *Fig. 4.* [HORVÁTH and ROYDEN 1981] has been devided by a grid consisting of 30×44 cells each representing 20×20 km^2. The average

Fig. 4. Isopach map of the Neogene–Quaternary sedimentary complex, including volcanic flood tuffs [HORVÁTH and ROYDEN 1981]

4. ábra. A neogén–kvarter üledékösszlet vastagságtérképe a vulkáni tufákat is beleértve [HORVÁTH és ROYDEN 1981. után]

Рис. 4. Карта мощностей неоген–четвертичных отложений, включай и вулканические туфы, по ХОРВАТУ и РОЙДЕН 1981 [HORVÁTH and ROYDEN 1981]

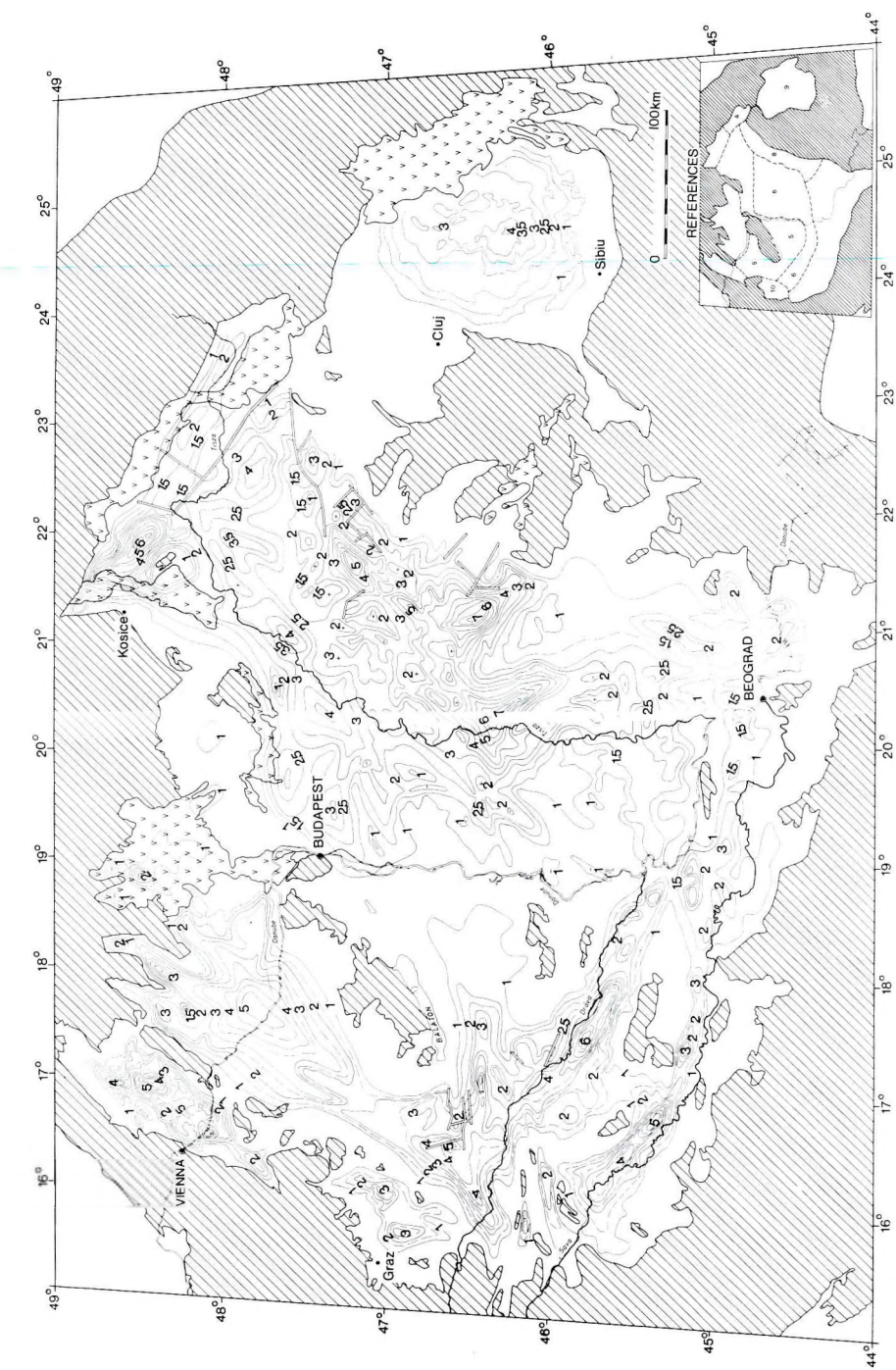
VIENNA
BUDAPEST
BEOGRAD
Graz
Kosice
Cluj
Sibiu
Danube
Drava
Sava
Tisa
BALATON
0
100km
REFERENCES

conductance (S) of these squares was calculated on the basis of the thickness of sediments and an average resistivity [ÁDÁM and VERŐ 1967: 4.4 Ωm] characterizing the sedimentary cover of the Pannonian basin. Of course, a real S map would have led to a better approximation of the problem. *Figure 5* shows the S–value map used in the calculation having the same frame as Fig. 4. The crustal conductor of the Transdanubian Central Range was not taken into account due to the limits of the computer program. This was also the reason for substituting the Carpathian anomaly by a surface conductance increase.

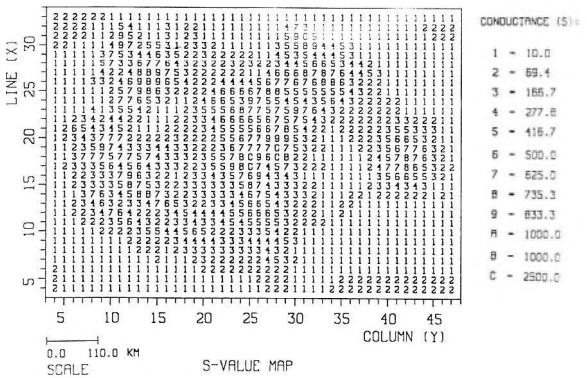

Fig. 5. Conductance map of the Carpathian basin

5. ábra. A Kárpát-medence vezetőképesség térképe

Рис. 5. Карта проводимости Карпатского региона

The induction vectors were calculated for periods (T) between 300 and 3600 s and for conductances of the frame between 12.5 and 250 Siemens. The resistivity of the basement has been taken to be 1000 Ωm. The results are shown in *Figs. 6.* and *7.* In Figure 6 the real induction vectors are shown calculated with S_1 for (a) T=3600 s and (b) T=1000 s. In Fig. 7. the same quantities are given for S_2 and for (a) T=3600 s and (b) T=1000 s. If one compares the isopach map and the induction vectors, the correlation between the deepening of the basin and the anomalous feature of the induction vectors is in both cases obvious. The effect of the anomalous resistivity frame of the Pannonian basin is strongly modified by the local variations of the sediment thickness.

It is very difficult to find any relation between the calculated real induction vectors and the measured Wiese arrows *(Fig. 8.)* which are certainly influenced by the conducting bodies (mainly graphitic schist embedded in the basement) and the deep crustal and mantle structure. In the next step of the calculations these should also be considered.

It should be mentioned that in all cases the modulus of the computed induction vectors remains smaller then 0.05. This means that the contribution of the sedimentary structure to the observed induction vectors is smaller than the uncertainties in their determination. This question should be further studied.

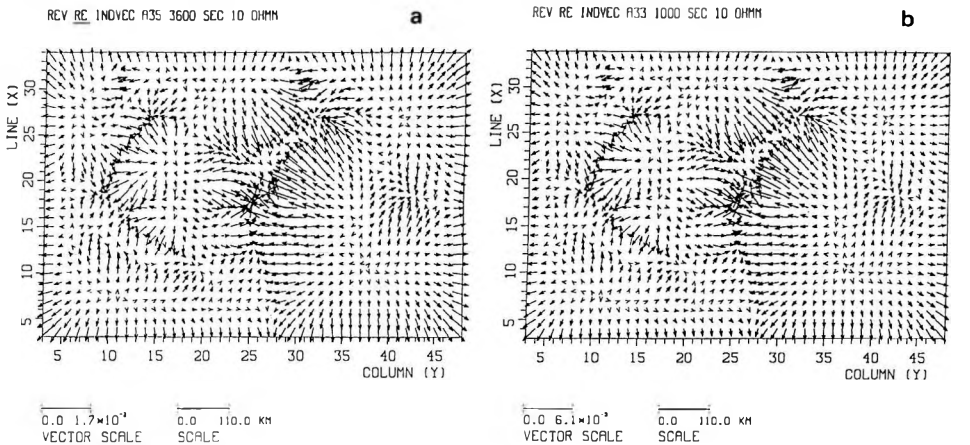

Fig. 6. Real induction vectors calculated with S_1=12.5 Siemens for T=3600 s (a) and T=1000 s (b)

6. ábra.. Valós indukciós vektorok az S_1=12,5 Siemens esetre, T=3600 s (a) és T=1000 s (b) periódusra

Рис. 6. Реальные индукционные вектора для случая S_1= 12.5 сименс и для периодов T = 3600 с (a) и T = 1000 с (b)

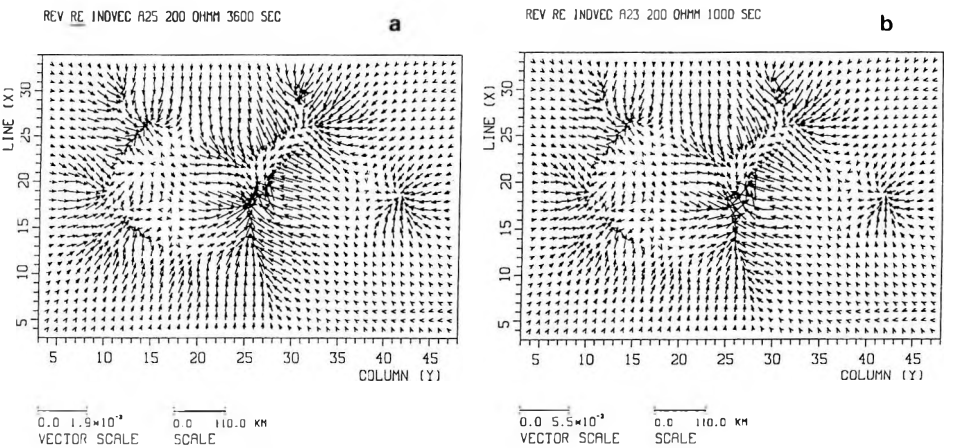

Fig. 7. Real induction vectors calculated with S_2=250 Siemens for T=3600 s (a) T=1000 s (b)

7. ábra. Valós indukciós vektorok az S_2=250 Siemens esetre, T=3600 s (a) és T=1000 s (b) periódusra

Рис. 7. Реальные индукционные вектора для S_2= 250 сименс и для периодов T = 3600 с (a) и T = 1000 с (b)

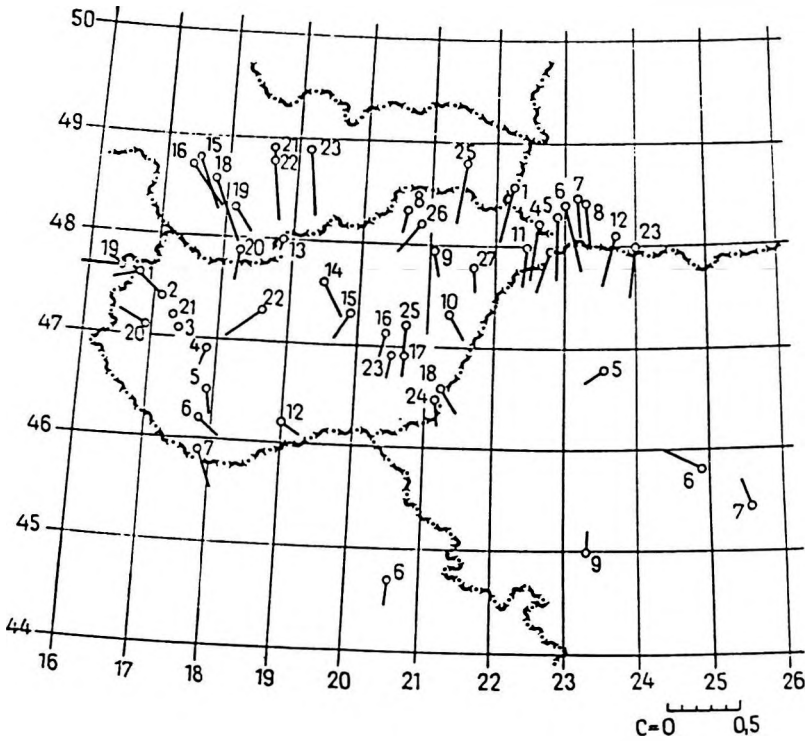

Fig. 8. Wiese arrows determined in the Carpathian basin [ÁDÁM et al. 1972]

8. ábra. A Kárpát-medencére meghatározott Wiese-nyilak [ÁDÁM et al. 1972. után]

Рис. 8. Вектора Визе для Карпатского бассейна по Адаму др. 1972 [ÁDÁM et al. 1972]

3. 2-D modelling

2-D modelling was carried out by a slightly modified version of the program of WANNAMAKER et al. [1986] adopted by ILONEM. The aim of the calculation was to determine the effect of a resistive triangular block 2500 m high, approximating the High Tatra and that of a conducting body corresponding to the Carpathian anomaly in two versions (i) the model of JANKOWSKI et al. [1984] and (ii) that of SWENTISKA-PAWLISZIN and PAWLISZIN [1983]. The effect was calculated for point 0 km above the centre of the triangle and for a point 100 km far from it, in the basin.

Figures 9 and *10* show the effect of the High Tatra on the phase and resistivity curves at points 0 and 100 (km). Judging both from resistivity and phase curves, the resistive block has no effect at a distance of 100 km from its axis.

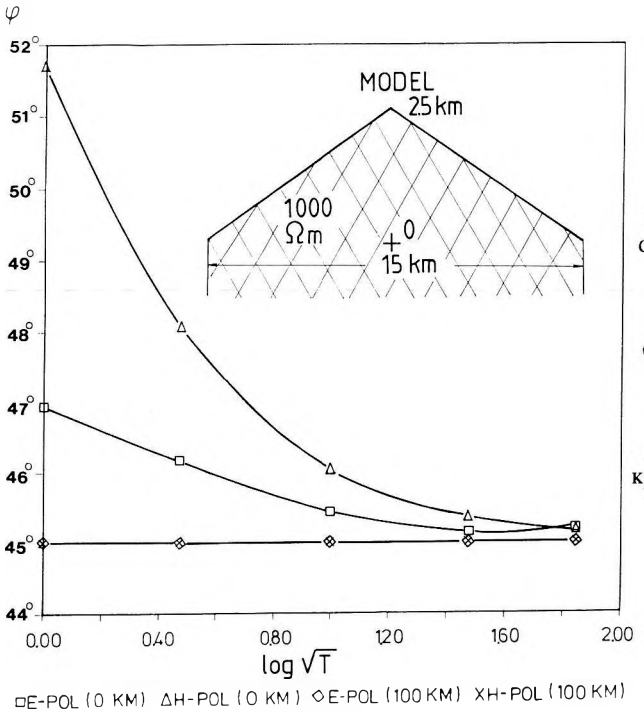

Fig. 9. Electromagnetic effect of the High Tatra on the phase sounding curves

9. ábra. A Magas-Tátra elektromágneses hatása a fázis szondázási görbékre

Рис. 9. Электромагнитный эффект от высоких Татр на кривые зондирования по фазам

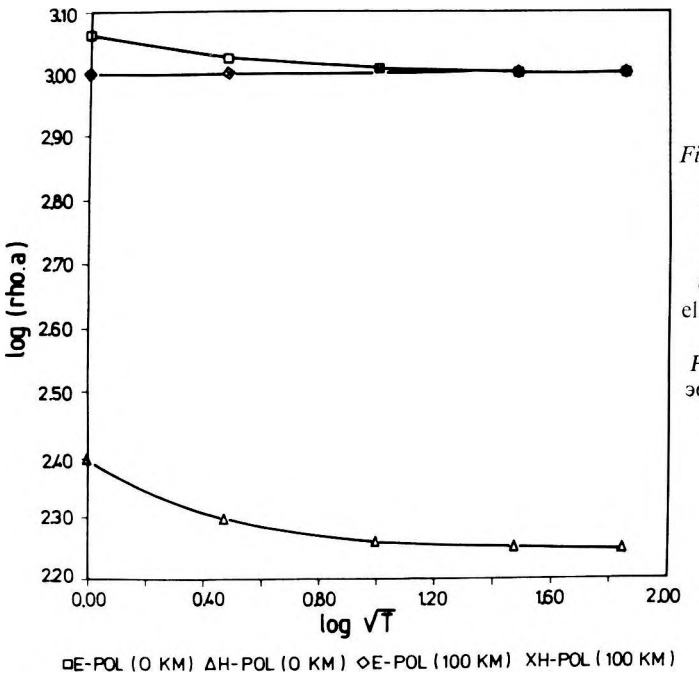

Fig. 10. Electromagnetic effect of the High Tatra on the resistivity sounding curves

10. ábra. A Magas-Tátra elektromágneses hatása az ellenállásszondázási görbékre

Рис. 10. Электромагнитный эффект от высоких Татр на кривые зондирования по сопротивлениям

Figures 11 and *12* represent the EM responses of the conducting bodies approximating those proposed by JANKOWSKI et al. [1984] and SWENTISKA-PAWLISZIN and PAWLISZIN [1983] (Swentiska model in the following), respectively. Again, there is a great difference between the sounding curves corresponding to points 0 and 100 km. Lateral effects of the conducting body do not appear at a distance of 100 km from its centre. The upgoing end of all sounding curves approximate well the resistivity of the host rock, i. e. 1000 Ωm, except the *E*-polarization curve of the Swentiska model which reaches only about 450 Ωm. This is due to the presence of a much higher resistivity first layer in the Swentiska model than in the Jankowski model. As the integrated conductivity (conductance) of the sediments in the Pannonian basin can be greater than 500 S (see Fig. 4), the Jankowski model is a better representation of the real conditions in the whole area investigated in this paper. This 2-D modelling supported our former result that in the Pannonian basin there exists no significant distortion resulting from the Carpathian regional structure.

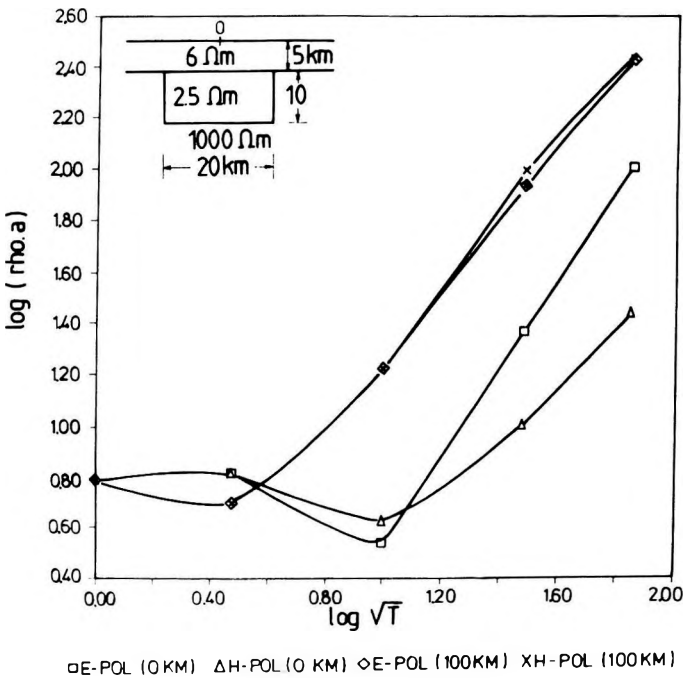

Fig. 11. Effect of the Carpathian anomaly using the model of JANKOWSKI et al. [1984]

11. ábra. A Kárpát-anomália hatása a JANKOWSKI et al. [1984]-féle modell felhasználásával

Рис. 11. Эффект карпатской аномалии с использованием модели Янковского и др. [JANKOWSKI et al. 1984]

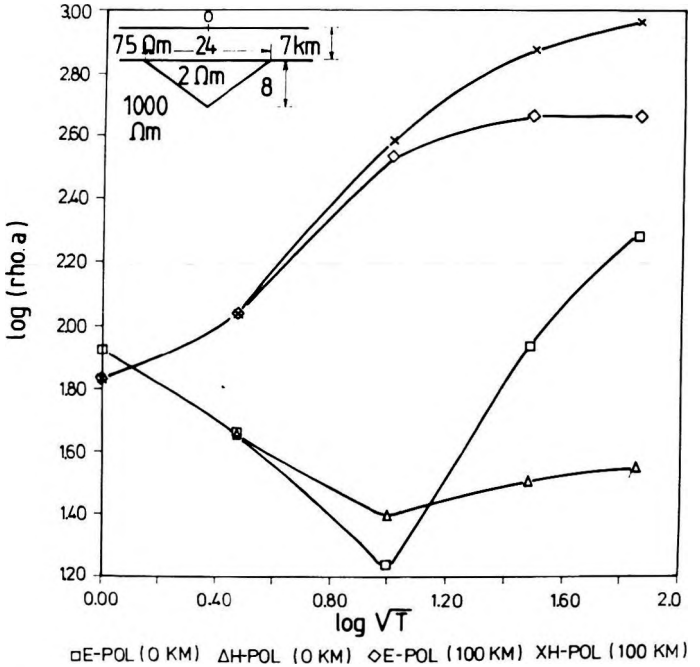

Fig. 12. Effect of the Carpathian anomaly using the model of SWENTISKA-PAWLISZIN and PAWLISZIN [1983]

12. ábra. A Kárpát-anomália hatása a SWENTISKA-PAWLISZIN és PAWLISZIN [1983]-féle modell felhasználásával

Рис. 12. Эффект от карпатской аномалии с использованием модели Свентинской–Павлишина и Павлишина [SWETINSKA–PAWLISZIN and PAWLISZIN 1983]

4. Conclusions

The results of numerical computations presented in this paper show that it is unlikely that there is any significant distortion in the observed electromagnetic field resulting from the regional Carpathian structure (in the period range 400–2000 s). All distortions appearing in the observed MT curves would therefore be due to the local variation of the resistivity distribution. For periods greater than 20 minutes, the induction vectors are thus representative of deep conductivity heterogeneities. There is therefore no bias related to the sedimentary structure in deep conductivity models deduced from geomagnetic sounding.

The relatively shallow depths of the lower crustal and asthenospheric conductivity anomaly in the Pannonian basin are clearly correlated with the high heat flow of the region so they have a real physical meaning and are not the results of any EM field distortions.

REFERENCES

ÁDÁM A. 1970: Problems of electric upper mantle research in the Hungarian basin. In: Somogyi J. and Verő J. (editors): Fifteen Years of Geod. and Geophys. Lab. of Hung. Acad. of Sciences in Sopron, pp. 77–91

ÁDÁM A., LANDY K., NAGY Z. 1989: New evidence for the distribution of the electric conductivity in the Earth's crust and upper mantle in the Pannonian basin as a „hot spot". Tectonophysics **164**, pp. 361–368

ÁDÁM A., VERŐ J. 1967: Latest results of electromagnetic measurements in Hungary (in Hungarian). Geofizikai Közlemények **16**, 1–2, pp. 26–52

ÁDÁM A., VERŐ J., WALLNER Á. 1972: Regional properties of geomagnetic induction arrows in Europe. Acta Geod. Geoph. Mont. Hung. **7**, 3–4, pp. 251–287

HORVÁTH F., ROYDEN L. 1981: Mechanism for the formation of the Intra-Carpathian basins: A review. Earth Evol. Science **1** (3-4), pp. 307–316

JANKOWSKI J., PETR V., PĚČOVÁ J., PRAUS O. 1984: Geoelectric anomaly in the Czechoslovak-Polish section of the Carpathians on the basis of geomagnetic and magnetotelluric soundings. Acta Geod. Geoph. Mont. Hung. **19**, 1–2, pp. 81–91

ROKITYANSKY I. I., YUDIN M. N. 1984: Modelling of the electromagnetic field in the Carpathian region. Acta Geod. Geoph. Mont. Hung. **19**, 1–2, pp. 139–144

SWENTISKA-PAWLISZIN J., PAWLISZIN J. 1983: Magnetotelluric modelling of the Carpathian conductivity anomaly on the territory of Poland. Proceedings of the 28th International Geophys. Symposium, Balatonszemes, 28. 9–1. 10. 1983, Part II, pp. 848–858

VASSEUR G., WEIDELT P. 1977: Bimodal electromagnetic induction in non-uniform thin sheets with an application to the northern Pyrenean induction anomaly. Geophys. J. R. Astron. Soc. **51**, 3, pp. 669–690

WANNAMAKER P. E., STODT J. A., RIJO L. 1986: Two-dimensional topographic responses in magnetotellurics using finite elements. Geophysics **51**, 11, pp. 2131–2144

TORZÍTJÁK-E A MAGNETOTELLURIKUS TERET A KÁRPÁTI ELEKTROMOS INHOMOGENEITÁSOK A PANNON MEDENCÉBEN?

ÁDÁM Antal, STEINER Tibor, Pertti KAIKKONEN, Michel MENVIELLE és Pascal TARITS

A Pannon medencében a földkéreg és asztenoszféra elektromos vezetőképesség növekedését a nagymélységű magnetotellurikus szondázások kisebb mélységben jelzik, mint a körülötte lévő idős nagytektonikai egységeken. Felmerül a kérdés, nem torzítja-e az MT görbéket a Kárpátok nagyellenállású hegységkerete és a kárpáti jólvezető kéreg-anomália. A kérdésre a tanulmány kétféle numerikus modellszámítással igyekszik válaszolni: (1) A felszíni ellenállás-kontrasztnak a mágneses térre gyakorolt hatását bimodális vékonyréteg modellezéssel (VASSEUR–WEIDELT program, ILONEM, Oulu) tanulmányoztuk nagyellenállású és jólvezető medenceperem, azaz a medencén kívül felvett különböző horizontális vezetőképesség (*S*) esetében, és (*2*) a nagyellenállású kárpáti hegységtömeg és közelében lévő jólvezető kéreganomália lehetséges hatását a Pannon medencében mért magnetotellurikus szondázási görbékre kétdimenziós numerikus modellszámítással vizsgáltuk. A hatás mindkét esetben elhanyagolhatónak bizonyult.

ИСКАЖАЮТ ЛИ КАРПАТСКИЕ ГЕОЭЛЕКТРИЧЕСКИЕ НЕОДНОРОДНОСТИ МАГНИТОТЕЛЛУРИЧЕСКОЕ ПОЛЕ ПАННОНСКОЙ ВПАДИНЫ?

Антал АДАМ, Тибор ШТЕЙНЕР, Пертти КАЙККОНЕН,
Мишель МЕНВЬЕЛЬ, Паскаль ТАРИТС

В Паннонской впадине возросшая геоэлектрическая проводимость земной коры и астеносферы отмечается глубинным магнитотеллурическим зондированием на меньших глубинах, нежели в окружающих более древних тектонических структурах. Встает вопрос, не искажаются ли кривые МТЗ горным обрамлением Карпат, характеризующимся высокими сопротивлениями, и аномалней повышенной проводимости в земной коре Карпат. В статье ответ на поставленный вопрос подыскивается путем цифровых модельных расчетов свух типов: (1) эффект, оказываемый контрастными изменениями приповерхностных сопротивлений на магнитное поле, исследовался на бимодальной модели тонкого слоя (программа Вассёра–Вейдельта, ИЛОНЕМ, Оулу) для случаев высоко- и низкоомного обрамления впадины, то-есть при различных горизонтальных проводимостях *(S)*, принимаемых для вневпадинных районов, и (2) возможный эффект, оказываемый карпатскими горными массами высокого сопротивления и расположенными вблизи от них аномального, проводящего тела на кривые МТЗ, получаемые в Паннонской впадине, исследовался путем цифровых расчетов двухмерных моделей. Эффект в обоих случаях оказался незначителъным.

GEOPHYSICAL TRANSACTIONS 1990
Vol. 35. No. 4. pp. 301–313

LITHOSTATISTICAL STUDY OF KHARITA FORMATION, WESTERN DESERT, EGYPT

Ahmed Aly HASSAN* and Azz El-Din Aly SALEH*

In an attempt to detect and/or predict lithologic constituents from well-logging data, a statistical technique is used that is based on the idea that layer-wise or point-wise well-log values are considered as probablistic variables. The probability that these variables belong to individual zones, can be evaluated on the basis of their measured values, scatter, and weight matrix. For comparison matrix analysis has also been carried out using several standard crossplots. Two examples are given in this paper that represent the occurrences of rock components of the Kharita Formation in the Abu Subeiha–IX and Fadda–I wells which are located in the northern part of the Egyptian Western Desert.

Keywords: log analysis, statistical interpretation, probabilistic variables, matrix analysis, crossplots, Western Desert, Egypt

1. Introduction

SOKHRANOV [1973] and SZENDRŐ [1983] introduced a statistical technique for lithologic discrimination based on the idea that different types of rocks manifest themselves in different logs with non-overlapping ranges or zones of values. The basic principle of this technique is explained below:

The logs and the assumed rock types are indicated by the indices n and m respectively,

$$\text{where } n = 1, 2, 3, ..., N$$
$$\text{and } m = 1, 2, 3, ..., M.$$

The probatility that a given type of rock occurs is denoted by P_m. Two symbols, a_{nm} and b_{nm} indicate the lower and upper boundary of the zone characterizing the m-th rock type in the n-th log, respectively. *Table I* gives the compiled parameters in a matrix of $(N+1)\times M$ elements.

2. Statistical approach

Dispersion σ

The dispersion of the measured values of the log with respect to a certain rock type can be computed using the following formula [CHURINOVA et al. 1980]:

*Geology Department, Faculty of Science, Tanta University, Egyipt
Manuscript received (revised version): 19 December, 1989

$$\sigma = \frac{Y_{max} - Y_{min}}{10} \quad (1)$$

where Y_{max} and Y_{min}, respectively, indicate the maximum and minimum measured values of each log for a certain rock type.

A value of Y_{ni} denotes the reading of the n-th log at the i-th sampling point, where

$$n = 1, 2, 3, ..., N$$
$$\text{and } i = 1, 2, 3, ..., I$$

Logs \ Geological formation	1	2	...	M
1	a_{11} b_{11}	a_{12} b_{12}	...	a_{1M} b_{1M}
2	a_{21} b_{21}	a_{22} b_{22}	...	a_{2M} b_{2M}
. . .	. . .	. . .		. . .
N	a_{N1} b_{N1}	a_{N2} b_{N2}	...	a_{NM} b_{NM}
probabilities of occurrence	p_1	p_2	...	P_M

Table I. The $(N+1)\times M$ matrix including the statistical lithologic parameters (a_{nm}, b_{nm} and p_m) [after SZENDRŐ 1983]

I. táblázat. Az (a_{nm}, b_{nm} és p_m) kőzetstatisztikai paramétereket tartalmazó, $(N+1)\times M$ tagú mátrix [SZENDRŐ 1983 után]

Таблица I. Матрица петростатистических параметров (a_{nm}, b_{nm} и p_m), содержащая $(N+1)\times M$ членов по Сендрё [Szendrő 1983]

The dispersion σ_{ni}, which characterizes the accuracy of Y_{ni} is affected by various factors: these are the instrument parameters, measurement conditions and the eventual statistical behaviour of the particular geophysical parameter.

The probability that a measured value Y_{ni} of a dispersion corresponds to an expected value Y_n of a zone (a_{nm}, b_{nm}) for the m-th rock type on the n-th log is given by CHURINOVA et al. [1980] as:

$$P_{nmi} = \frac{1}{2}\frac{2}{\sqrt{2\pi}}\left[\int_0^{t_{nm1}} \exp\frac{-t_n^2}{2}dt_n\right] + \frac{2}{\sqrt{2\pi}}\int_0^{t_{nm2}} \exp\frac{-t_n^2}{2}dt_n \quad (2)$$

where

$$t_n=(Y_n-Y_{ni})/\sigma_{ni}$$
$$t_{nm1}=(Y_{ni}-a_{nm})/\sigma_{ni}$$

and

$$t_{nm2}=(b_{nm}-Y_{ni})/\sigma_{ni}$$

The integrals of the above equation are known as the error integrals. These are functions of the upper limits of the integration, which is the distance of the measured value of the n-th log from the boundaries of the m-th zone expressed in units of dispersion.

Weight Factor, C_{nm}

This factor provides the measure by which the value of the n-th log is considered in the determination of the m-th rock type, it ranges between zero and one, indicating that the values of the n-th log are not utilized in the evaluation of the m-th rock type (C_{nm}=0); or they may be very characteristic (C_{nm} = 1). The different values of weight factors are tabulated as a lithologic weight matrix *(Table II)*.

Probability of occurrences of a given rock type

Considering the concept of the statistical lithologic weight matrix, the weighted probability can be defined by the following equation [SZENDRŐ 1983]:

$$P^w_{nmi} = \frac{1-C_{nm}}{2} + C_{nm}P_{nmi}\,. \quad (3)$$

The probability that the measured values Y_{ni} (n=1, 2, ..., N) of a log combination belong to the corresponding zone $b_{nm}-a_{nm}$ and that they all characterize the m-th rock type, is given by

$$P_{mi} = P_m\prod_{n=1}^{N} P^w_{nmi}\,, \quad (4)$$

where P_m is the probability of occurrence of the m-th rock type.

Logs \ Geological formation	1	2	...	M
1	c_{11}	c_{12}	...	c_{1M}
2	c_{21}	c_{22}	...	c_{2M}
. . .	. . .	. . .		. . .
N	c_{N1}	c_{N2}	...	c_{NM}

Table II. The lithologic weight matrix. C_{nm} (n=1, 2, ...N; m=1, 2, ..M) are the weight factors [after SZENDRŐ 1983]

II. táblázat. A kőzettani súlymátrix. C_{nm} (n=1, 2, ..N; m=1, 2, ...M) a súly faktorok [SZENDRŐ 1983 után]

Таблица II. Петрографическая весовая матрица. C_{nm} (n=1, 2, ... N; $м$=1, 2, ... M) – весовые факторы по Сендрё [SZENDRŐ 1983]

Supposing that there are only M kinds of possible rock types, the probability can be normalized to 1:

$$P_{mi}^{norm} = \frac{P_{mi}}{\sum_{m=1}^{M} P_{mi}} \tag{5}$$

The resultant computed probabilities indicate the occurrence of a given rock type on the basis of the available logs.

3. Application

Various methods have been applied to evaluate the lithological fractions at each sampling point in the Abu Subeiha–IX and Fadda–I wells in the Western Desert of Egypt *(Fig. 1)*. Considering the analysed Kharita formation the statistical method was applied to detect the most probable lithology encountered in the wells. By using computer facilities, first the statistical parameters presented in *Tables III* to *VI* were determined for all the available logs, then for the estimation of the probability of occurrence of rock types *(Figs. 2* and *3)* at each depth point.

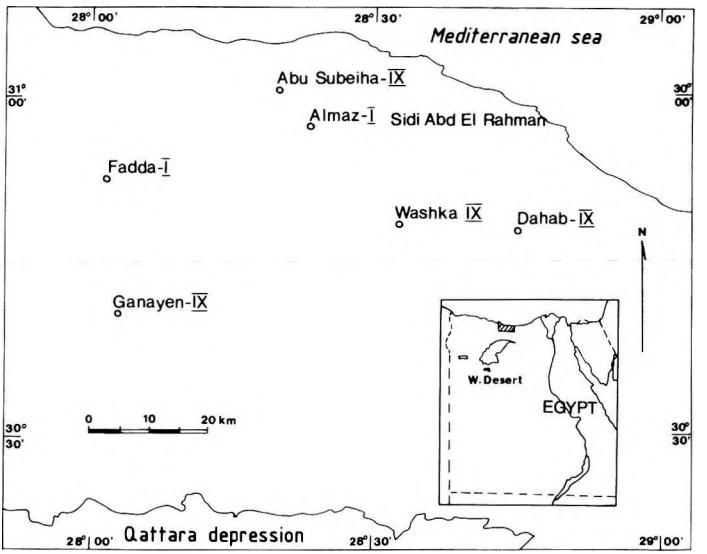

Fig. 1. Location map of the study area showing the distribution of the studied wells

1. ábra. Helyszínvázlat a tanulmányban felhasznált fúrásokkal

Рис. 1. Схема расположения скважин, использованных в работе

The values of a_{nm} and b_{nm} that represent the upper and lower boundaries of a log characterizing each rock type have been determined as the limits of the 97% of occurrence range of a group of log variables characterizing a certain rock type. It should be noted that in the case of identical minimum and maximum values (a_{nm} and b_{nm}), t_{nm1} and t_{nm2} will have the same absolute value but they will differ in sign. When a measured value Y_{ni} equals a_{nm} and b_{nm} then $t_n=0$ and $t_{nm1}=t_{nm2}=0$ and the exponent $-t_n^2/2=0$ too, accordingly $P_{nm1}=1$.*

As far as the values of the lithologic weight matrix are concerned, they depend completely on the degree of overlap between zones of values in such a way that when the degree of overlap increases, the weights decrease: at non-overlapping zones $C_{nm}=1$, and in completely overlapping zones $C_{nm}=0$. A flow chart is given in *Figure 4* that summarizes the steps used in the statistical lithological interpretation.

*Editor's note: Although the author's explanation for using identical minimum and maximum values provides a formal solution, the probability of recording the same value for a given rock type — if the number of sampling points satisfies the statistical criteria — is very low. In the wells detailed here these criteria are not met, no wonder the greatest mismatch between matrix analysis and probabilistic interpretation occurs in the zone of limestone.

Logs \ Lithology	Sandstone	Limestone	Dolomite	Shale
Gamma	12.00 24.00	27.00 27.00	10.00 21.00	43.00 73.00
SP	–28.00 –15.00	–18.00 –15.00	–8.00 0.00	–9.00 0.00
R_t	0.40 0.70	2.60 2.60	4.50 40.00	1.30 2.50
R_{xo}	0.30 0.80	1.80 1.80	2.60 9.30	1.40 2.80
dT	78.00 85.00	65.00 65.00	49.00 65.00	83.00 112.00
FDC	2.21 2.35	2.63 2.63	2.67 2.86	2.00 2.40
SNP	18.50 25.00	12.00 12.00	4.00 14.00	27.00 49.00
Caliper	12.25 12.50	12.30 12.50	12.25 12.80	12.70 16.00
Probability of Occurrence	0.55	0.02	0.24	0.20

Table III. The statistical lithologic matrix of Abu Subeiha–IX well
Gamma: gamma-ray log (cpm); SP: spontaneous potential log (mV); R_t: resistivity of the uncontaminated zone (Ωm); R_{xo}: resistivity of the flushed zone (Ωm); dT: acoustic log (Δt) (μs/feet); FDC: formation density log (g/cm^3); SNP: Sidewall neutron porosity log (%); CNL: Compensated neutron log (%); Caliper: caliper log (inch)

III. táblázat. Az Abu Subeiha–IX fúrás kőzetstatisztikai mátrixa.
A szelvények jelölése: Gamma: természetes gamma (cpm); SP: természetes potenciál (mV); R_t: az érintetlen zóna ellenállása (Ωm); R_{xo} — az elárasztott zóna ellenállása (Ωm); dT: akusztikus Δt (μs/láb); FDC: formáció sűrűség (g/cm^3); SNP: oldalfal neutron porozitás (%); CNL: kompenzált neutron (%); Caliper: lyukátmérő (inch)

Таблица III. Петростатистическая матрица скважины Абу Субейха–IX. Обозначения кривых: gamma – естетственной гамма-активности (cpm);
SP – естественных потенциалов (мв); R_t – сопротивление нетронутой зоны (омм); R_{xo} – сопротивление обводненной зоны (омм); dT – акустическаяа Δt (микросек/фут); FDC – формационная плотность (г/см^3); SNP – нейтронная пористость боковых стенок (%); CNL – компенсированная нейтронная пористость (%); Caliper – диаметр скважины (дюймы)

Logs \ Lithology	Sandstone	Limestone	Dolomite	Shale
Gamma	0.4	0.3	0.4	1.0
SP	0.7	0.3	0.4	1.0
R_t	1.0	0.5	1.0	0.8
R_{xo}	1.0	0.5	0.9	0.7
dT	0.8	0.6	1.0	0.8
FDC	0.7	0.6	1.0	0.6
SNP	0.8	0.7	1.0	0.9
Caliper	0.6	0.4	0.4	0.9

Table IV. The lithologic weight matrix of Abu Subeiha–IX well. For symbols see Table III

IV. táblázat. Az Abu Subeiha–IX fúrás kőzettani súlymátrixa. Jelöléseket lásd a III. táblázatban

Таблица IV. Весовая петрографическая матрица скважины Абу Субейха–IX. Условные обозначения см. в табл. III.

Logs \ Lithology	Sandstone	Limestone	Dolomite	Shale
Gamma	19.00 30.00	22.00 28.00	17.00 24.00	44.00 72.00
SP	−50.00 −37.00	−9.00 −1.00	−49.00 −8.00	−10.00 0.00
R_t	0.30 0.90	5.00 17.00	10.00 65.00	1.40 2.50
R_{xo}	0.35 1.00	5.00 10.00	13.00 65.00	1.50 3.00
dT	77.00 88.00	56.00 63.00	47.00 58.00	85.00 130.00
FDC	2.21 2.37	2.67 2.70	2.68 2.82	1.95 2.37
CNL	17.00 23.50	0.00 9.00	0.00 10.50	29.00 45.00
Caliper	11.70 12.70	18.00 18.00	14.00 16.00	13.20 18.00
Probability of Occurrence	0.57	0.02	0.14	0.27

Table V. The statistical lithologic matrix of Fadda–I well. For symbols see Table III

V. táblázat A Fadda–I fúrás kőzetstatisztikai mátrixa. Jelöléseket lásd a III. táblázatban

Таблица V. Весовая петростатистическая матрица скважины Фадда–I. Условные обозначения см. в табл. III.

Logs \ Lithology	Sandstone	Limestone	Dolomite	Shale
Gamma	0.5	0.3	0.3	1.0
SP	0.8	0.3	0.3	1.0
R_t	1.0	0.9	0.9	0.7
R_{xo}	1.0	0.9	1.0	0.8
dT	0.8	0.9	0.9	0.9
FDC	0.7	0.9	1.0	0.7
CNL	0.9	0.7	0.9	0.9
Caliper	0.9	0.0	0.3	0.9

Table VI. The lithologic weight matrix of Fadda–I well. For symbols see Table III

VI. táblázat. A Fadda–I fúrás kőzettani súlymátrixa. Jelöléseket lásd a III. táblázatban

Таблица VI. Весовая петрографическая матрица скважины Фадда–I. Условные обозначения см. в табл. III.

It is also possible to determine the matrix elements using the triporosity *M–N*, *K–A* and *MID* crossplots [SCHLUMBERGER 1972 and 1974]. Such litho-porosity crossplots of the Kharita formation for the two wells are given in *Figs. 5* and *6*. It can be seen that the sand facies prevails as indicated by the clustering of points around the quartz in all three crossplots of both Abu Subeiha–IX and Fadda–I wells. It must be noted that in the Abu Subeiha–IX well there is a slight tendency to gas or light CH-occurrence and in the Fadda–I well a secondary porosity trend is obvious, shown by the shifting of many points from quartz towards calcite in *MID* crossplots.

The volume percentage of the rock constituents is determined by an equation system set up for the values of *M*, *N*, *K*, *A*, ρ_b and Δt. In these equations the physical parameters characteristic of the individual rock-constituents were defined by the cross-plots of Fig. 5.

The results computed for each sampling point are shown in the right coloumns of Figs. 2 and 3. They are in good agreement with the results from the application of the statistical method.

Acknowledgements

The author wishes to thank the Management of the Egyptian General Petroleum Corporation (EGPC) for providing the well-log data.

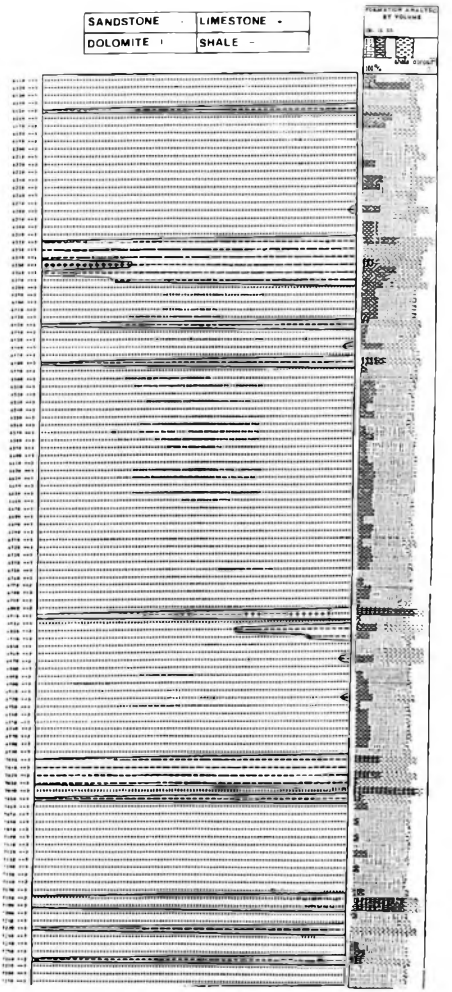

Fig. 2. Comparison of statistical lithologic interpretation and formation analysis by volume in Abu Subeiha–IX well

2. ábra. A kőzetstatisztikai és a kőzetösszetétel analízis módszer összehasonlítása az Abu Subeiha–IX fúrásban

Рис. 2. Сопоставление результатов петростатистического и петрографического способов по скважине Абу Субейха–IX.

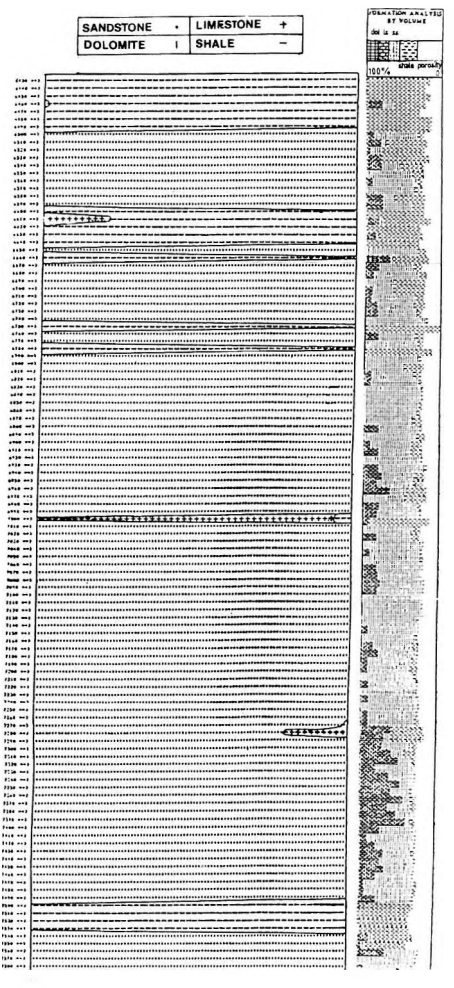

Fig. 3. Comparison of statistical lithologic interpretation and formation analysis by volume in Fadda–I well

3. ábra. A kőzetstatisztikai és a kőzetösszetétel analízis módszer összehasonlítása a Fadda–I fúrásban

Рис. 3. Сопоставление результатов петростатистического и петрографического способов по скважине Фадда–I.

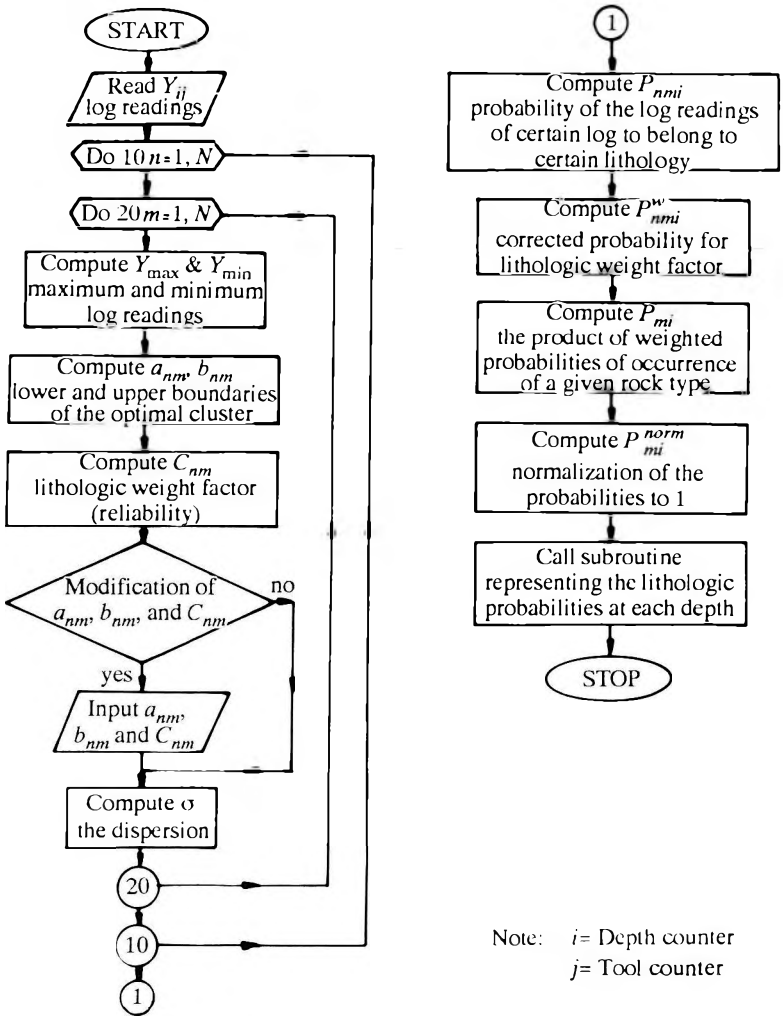

Fig. 4. Flow chart of the statistical lithologic interpretation program

4. ábra. A kőzetstatisztikai értelmezési program folyamatábrája

Рис. 4. Схема программы по петростатистическому анализу

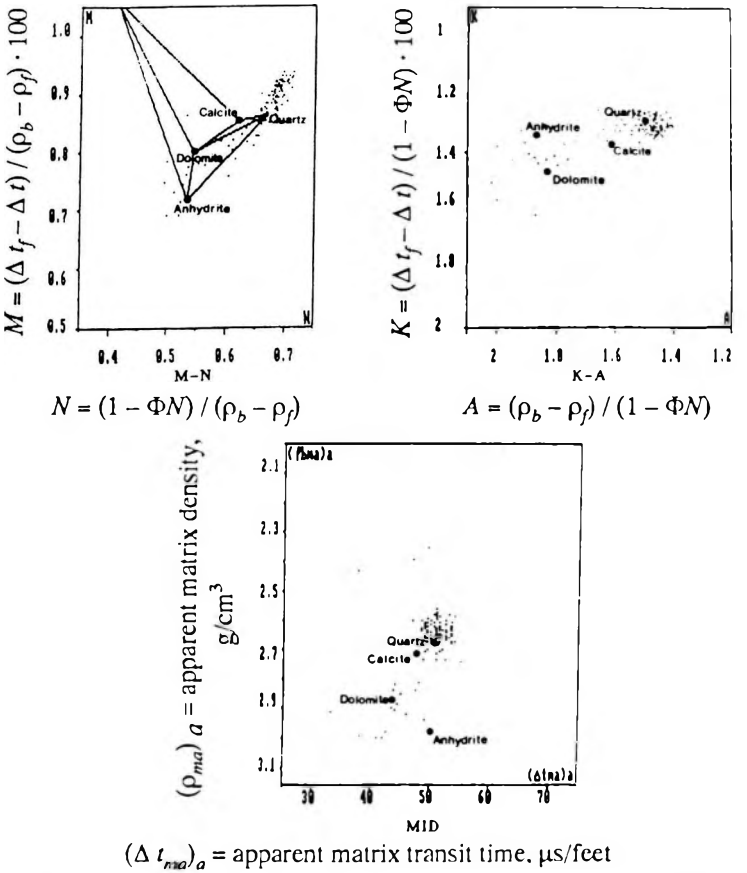

Fig. 5. Litho-porosity crossplots of the Kharita Formation (Abu Subeiha–IX well). Note that the points are clustered towards the quartz point indicating a sandstone lithology with slight tendency to gas or light hydrocarbon occurrence as shown in *M–N* and *MID* crossplots.
Δt_f: fluid (water) transit time = 189μs/feet; Δt: interval transit time (μs/feet); ρ_b: bulk density (g/cm^3); ρ_f: fluid density (g/cm^3); ΦN: neutron porosity

5. ábra. A Kharita Formációra szerkesztett kőzetporozitás diagramok (Abu Subeiha–IX fúrás). Megfigyelhető, hogy a pontok a kvarc körül sűrűsödnek, homok dominálását jelezve, gyenge gáz, vagy könnyű CH előfordulási tendenciával az *M–N* és *MID* crossplot-ban
Δt_f: folyadék terjedési idő (vízre 189 μs/láb); Δt: intervallum terjedési idő (μs/láb); ρ_b: térfogatsúly (g/cm^3); ρ_f: folyadéksűrűség (g/cm^3); ΦN: neutron porozitás

Рис. 5. Диаграммы пористости пород свиты Харита (скважина Абу Субейха–IX). Можно заметить, что точки сгущаются вокруг кварца, указывая на преобладание песка, на диаграммах *M–N* и *MID* с тенденцией проявления газов или легких нефтей.
Δt_f – время распространения в жидкости (для воды – 189 микросек/фут); Δt – интервальное время распространения (микросек/фут); ϱ_b – обьемный вес (г/см^3); ϱ_f – плотность жидкости (г/см^3); ΦN – нейтронная пористость

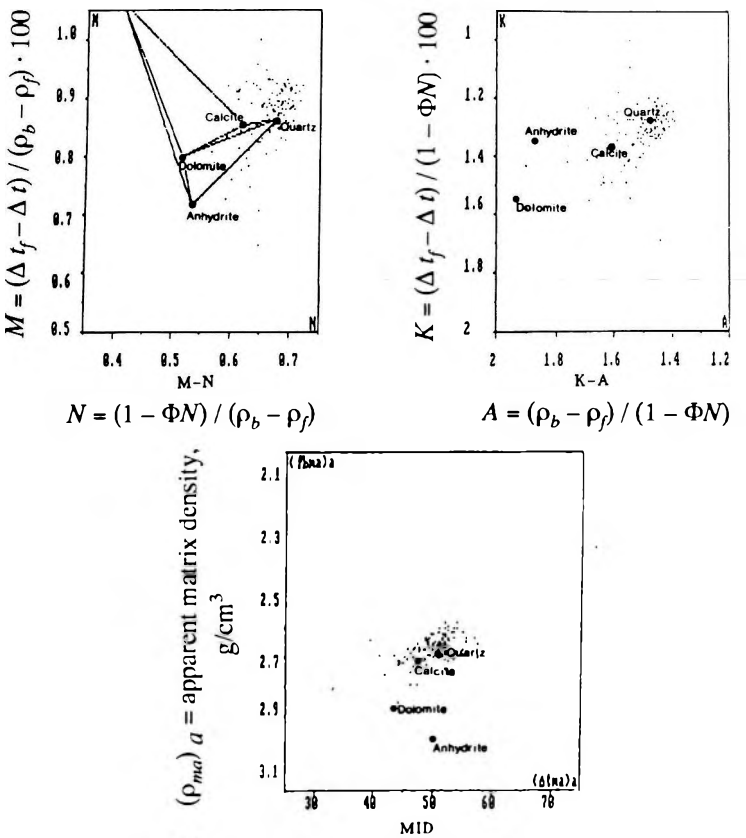

Fig. 6. Litho-porosity crossplots of Kharita Formation (Fadda–I well). Sandy facies prevails. Secondary porosity trend is obvious; this may be the cause of shifting of many points from the quartz towards the calcite in *MID* crossplot. For symbols see Fig. 5.

6. ábra. A Kharita Formációra szerkesztett kőzetporozitás diagramok (Fadda–I fúrás). A homok fácies uralkodik. A másodlagos porozitás a pontoknak a kvarctól a kalcit felé való eltolódásában nyilvánul meg (*MID* crossplot)

Рис. 6. Диаграммы пористости пород свиты Харита (скважина Фадда–I). Преобладает песчаная фация. Вторичная пористость проявлена в смещении точек от кварца к кальциту (диаграмма *MID)*

REFERENCES

CHURINOVA I. M., ZHIGALINA N. P. and SZENDRŐ D. 1980: Reference manual for the „LITLOG" program of lithologic interpretation. Central Geophysical Expedition of the Soviet Oil Ministry Report, 31 p.

Log Interpretation chart book. Vol. I. — Principles. Schlumberger Ltd., New York, 1972, 112 p.

Log Interpretation chart book. Vol. II. — Applications. Schlumberger Ltd., New York, 1974, 116 p.

SOKHRANOV N. N. 1973: Computer interpretation and processing of borehole geophysical data. Nyedra, Moscow

SZENDRŐ D. 1983: A statistical method for lithologic interpretation from well logs. The Log Analyst 24, 3, pp. 16–23

A KHARITA FORMÁCIÓ (EGYIPTOM, NY-I SIVATAG) KŐZETSTATISZTIKAI VIZSGÁLATA

Ahmed Aly HASSAN és Azz El-Din Aly SALEH

A kőzetösszetétel karotázs adatokból történő meghatározására statisztikai módszert alkalmaztam. A módszer lényege, hogy a karotázs görbék értékeit pontonként, vagy rétegenként valószínűségi változóknak tekinti. Annak valószínűsége, hogy ezek a változók adott tartományhoz tartoznak, értéküket, szórásuk és súlymátrixuk alapján dönthető el. Összehasonlításként mátrix analízist is végeztem számos ismert crossplot felhasználásával. Két példán ismertetem a Kharita Formációra vonatkozó eredményeket: az Abu Subeiha–IX és a Fadda–I fúrás adatait felhasználva (mindkettő az egyiptomi Nyugati Sivatag északi részén található).

ПЕТРОСТАТИСТИЧЕСКОЕ ИССЛЕДОВАНИЕ СВИТЫ ХАРИТА (ЗАПАДНАЯ ПУСТЫНЯ, ЕГИПЕТ)

Ахмед Али ГАССАН и Азз Эл-Дин Али САЛЕХ

В определеннии состава пород по каротажным данным был использован статистический метод, сущность которого заключается в том, что значения на каротажных кривых рассматриваются в качестве переменных по точкам или же слоям. Вероятность принадлежности этих переменных к заданному интервалу решается на основании их значеней, дисперсий и весовых матриц. Для сопоставления был проведен матричный анализ с использованием ряда известных диаграмм. Результаты по свите Харита иллюстрируюзся на двух примерах: скважин Абу Субейха–IX и Фадда–I — в северной части Западной пустыни в Египте.

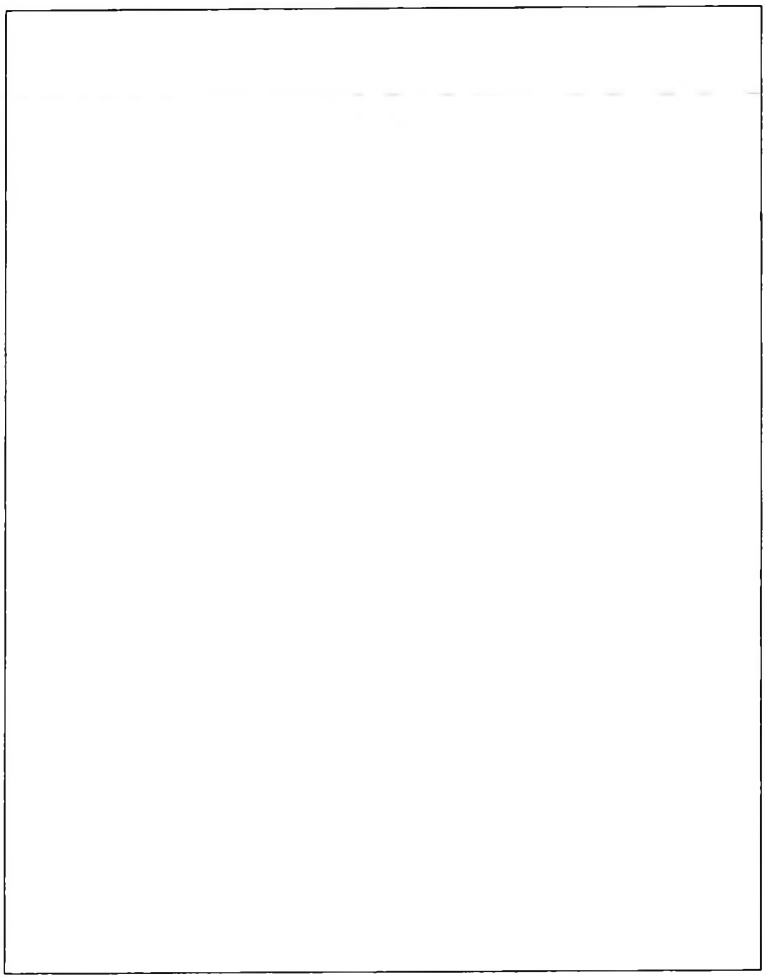

This page is waiting for you!